The BOLD fMRI Signal under Anaesthesia and Hyperoxia

Vom Fachbereich Biologie der Technischen Universität Darmstadt
zur
Erlangung des akademischen Grades eines
Doctor rerum naturalium
genehmigte Dissertation von

Dipl.-Phys. Michael Wibral
geboren in Essen

Referent der Arbeit: Prof. Dr. R. A. W. Galuske
Koreferent der Arbeit: PD Dr. habil. M. J. H. Munk

Eingereicht am: 31. Januar 2007
Tag der mündlichen Prüfung: 11. Mai 2007
Darmstadt 2007 - D17

Contents

Introduction

Functional Magnetic Resonance Imaging (fMRI) using the blood oxygenation level dependent (BOLD) effect [95] has become an indispensable tool in human brain mapping due to its non-invasive nature. BOLD fMRI indirectly measures neuronal activity by exploiting the fact that intra voxel field homogeneity in the brain is reduced by the presence of paramagnetic deoxyhemoglobin (dHb) molecules in an imaging voxel. Neuronal activation leads to disproportionate focal increases in regional cerebral blood flow (rCBF). This local hyperperfusion then reduces the total deoxyhemoglobin content of an imaging voxel of brain tissue. The reduction in turn leads to increased signal strength in MRI sequences sensitive to intravoxel field inhomogeneities. The level of the BOLD signal and its relative changes under stimulation, thus, sensitively depend on physiological baseline conditions [102] and the gain of neurovascular coupling.

The influence of an augmented oxygen fraction in the breathing gas on *baseline* rCBF has been extensively studied since the first experiments were conducted more than 50 years ago [68]. Multiple studies found the effect of hyperoxia to be a reduction of basal rCBF [96, 114] that was shown to be independent of the typically accompanying hypocapnia [38]. This reduction of rCBF has been consistently demonstrated over a wide range of species and physiological states from anaesthetised rats [3, 25] to conscious human subjects [96, 114, 38]. The influence of this hyperoxia induced reduction of regional cerebral blood flow on the relative amplitude of *stimulus induced* hemodynamic changes has been studied far less extensively, however, and with contradictory results (increase: [66]; decrease: [76]). Furthermore the effects of hyperoxia seem to depend on time as experiments using very short lasting hyperoxia of 7 minutes found no effects [119].

Experiments using fMRI under hyperoxic conditions can also yield valuable information on neurovascular coupling mechanisms as at least three substances that have been implied to play a role in the signalling cascade (for a recent review see: [60]) are also known to be directly influenced by hyper-

oxia: S-Nitroso-Hemoglobin (SNOHb) [88, 104], Prostaglandin E2 (PGE2) [89] and NO [3]. Last but not least detailed knowledge on the effects of prolonged hyperoxia is desirable as several recent experiments on the foundations of BOLD fMRI used added oxygen in the breathing gas over longer periods of time [69, 71, 46, 74, 65, 27].

The deoxyhemoglobin dilution model (DDM) developed by Hoge and colleagues [50] provides a basis to theoretically predict the effects of changed basal rCBF on the amplitude of stimulus induced BOLD fMRI signal changes. It has been successfully applied in the case of rCBF changes induced by CO_2 gas challenges. Here the DDM correctly predicted both the increase of relative stimulus induced signal changes for reduced basal rCBF under hypocapnia and the reduction of relative stimulus induced signal changes for increased basal rCBF under hypercapnia [21].

For the case of severe hyperoxia the classical DDM must fail, however, as it assumes a strict proportionality of deoxyhemoglobin (dHb) production and the cerebral metabolic rate of oxygen consumption ($CMRO_2$). This assumption is violated under hyperoxia which is due to the fact that non negligible amounts of oxygen are transported physically dissolved in the blood plasma (approximately 1.8 vol% at an ispiratory Oxgen fraction (FiO_2) of 100% [98]). This physically dissolved oxygen is metabolized fully before deoxyhemoglobin production starts as it is closer to the mitochondria on the oxygen pathway. This amount of physically dissolved oxygen has to be directly subtracted from the amount of oxygen taken from oxyhemoglobin under normal physiological conditions (approximately 8 vol% at normal flow conditions). The dependency between deoxyhemoglobin concentration and $CMRO_2$ is thus changed from a proportional to a merely linear one. In the appendix (A) we derive a modified version of the DDM for non-negligible concentrations of plasma oxygen. This model takes into account both plasma oxygenation and flow effects of hyperoxia and predicts an additional increase of relative BOLD fMRI response amplitudes for FiO_2 of 100% when compared to the predictions made by the classical DDM for this case. Deviations from this predicted increase would either indicate a direct influence of hyperoxia on neuronal activity or its direct interaction with mechanisms of neurovascular coupling.

To resolve the issue of conflicting results of previous hyperoxia studies, to provide the missing information on the temporal evolution of the effects of hyperoxia and to test the applicability of the modified DDM for the case of hyperoxia we used a visual stimulation paradigm to elicit BOLD fMRI responses in the visual pathway (lateral geniculate nucleus (LGN) and visual

cortex) of macaque monkeys and investigated changes in response strength under prolonged hyperoxia of up to 6 hours in a time resolved manner.

For fMRI signal changes in response to controlled stimuli, where strong *a priori* assumptions on the expected outcome can be made, analysis is best performed using the general linear model (GLM; see [73] and references therein). Results of this kind of analysis are presented in chapter 1.

However, signal components that are only loosely or not at all related to the stimulation escape this kind of model driven analysis. Important examples of such signal changes comprise the effects of changes in arousal and state under anaesthesia or signal changes related to mere physical factors like temperature changes. For the experimenter it is also of value to know about machine related artefacts in his data (that are e.g. due to shim drifts and signal drop outs). To uncover further signal components and, for those components of known physiological origin, their dependencies on changing anaesthesia conditions we therefore used the model free approach of independent component analysis in chapter 2. While successful in many fields of signal processing, ICA results in functional magnetic resonance imaging studies have sometimes been difficult to interpret due to missing additional information. Here we present an approach where ICA components were first clustered to extract components that were reliably extracted over multiple experimental runs. These component clusters were then tested for the existence of an influence of independent physiological and anaesthesia related variables. For components that reflected BOLD fMRI responses we compared ICA results to those of the GLM analysis with respect to anatomical location and sensitivity to changes in independent physiological and anaesthesia related variables.

Chapter 1

Changes in Stimulus Driven Hemodynamic Responses

Results presented in this chapter were accepted for publication in Neuroimage [118].

1.1 Introduction

BOLD fMRI signal changes (ΔBOLD%) in response to a certain stimulus are typically very weak, hardly ever exceeding a few percent of the total signal amplitude at magnetic field strengths used in research on humans. Therefore, techniques for noise reduction such as statistical tests for the presence of an a priori formulated (e.g. stimulus driven) signal part in the overall signal are used. The most common method used in fMRI in this respect is the general linear model (GLM) analysis (see [73] and references therein). It describes the statistical probability, that a signal partition similar to the binary (also termed 'boxcar') time course of an experimental condition (predictor) is present in the data. In contrast to simple correlation analysis multiple experimental conditions can be analysed simultaneously. Due to the fact that the BOLD fMRI response can be described using a stereotypical hemodynamic impulse response function [11] a more refined way of using the GLM is assuming a predictor that results from the convolution of the boxcar function of the experimental condition(s) with this hemodynamic impulse response function.

In this chapter we describe our experiment on the influence of hyperoxia and anaesthesia on the BOLD fMRI signal. The analyses in this chapter focus on the results of a GLM analysis for responses to visual stimulation.

We then analyse these results with respect to a manipulation of anaesthesia conditions, hyperoxic ventilation and the influence of recorded physiological covariates.

We would like to emphasise at this point that due to the use of the GLM analysis we can only analyse *stimulus driven* BOLD fMRI signal changes and their modulation by anaesthesia. Anaesthesia and hyperoxia will, nevertheless, also influence non stimulus related processing and the corresponding BOLD signal level in the brain. However, no clear hypotheses exist on this influence and therefore the GLM analysis is not applicable to these phenomena. In the second part of this study we will use a data driven approach (independent component analysis, ICA) to overcome these limitations and derive new hypotheses.

1.2 Materials and Methods

1.2.1 General

This study was conducted in five parts. In the first part (pilot experiment) we aimed to find potential linear and time independent influences of FiO_2 on stimulus induced ΔBOLD% and to assess the influence of potential confounding factors. In the second part (time course experiment) we tried to keep all anaesthesia related and all physiological parameters as constant as possible while recording the time course of changes in stimulus induced ΔBOLD% brought about by a single step in FiO_2 from 21% (room air) to 90%. To assess whether changes in vasoreactivity were responsible for the observed effects we then repeated the time course experiment using monocrystalline iron oxide nanoparticles (MION) [117] as a contrast agent to measure changes in rCBV independent of blood oxygenation (MION experiment). The fourth part of the study simply consisted in a repetition of the time course experiment in an additional animal (Monkey J) with an experimental schedule that was strongly shifted in time to establish independence of any effects of the circadian rhythm. The fifth part (termed paO_2 Experiment hereafter) was aimed at establishing that arterial hyperoxia is present even at late stages of the experiment. This was necessary as long exposure to an increased inspiratory fraction of oxygen can lead to reduced gas exchange capability of lung tissue and adult respiratory distress syndrome (ARDS) as shown in primates by Huang and colleagues [52]. Although arterial oxygen tension was still high above normoxic levels after 24 hours ($\sim$400mmHg) in their study, we nevertheless tried to establish that

any time dependent effects were independent of fluctuations in the level of arterial hyperoxia.

1.2.2 Animal Preparation and Monitoring

The animal experiments were performed according to the German Law for the Protection of Experimental Animals. The procedures also conformed to the regulations issued by the NIH and the Society for Neuroscience. Initial BOLD fMRI experiments (pilot experiment and time course experiment) were performed on 3 macaque monkeys (Monkeys: K, B, Se; 1 female (K), weight 5.7-9.7 kg). In the retest BOLD fMRI experiment we measured one additional monkey (J, male, 4.2 kg). The MION experiment comprised four monkeys (Monkeys: K, S, M; P, 3 females). In the paO_2 Experiment we measured two monkeys (J and P, 2 male). Anaesthesia was prepared by administering atropine sulphate (0.5 mg)IM. Dissociation was induced by an injection of the barbiturate Methohexital IM (30-45 mg/kg). This type of anaesthesia induction provides intact breathing reflexes and minimises the risk of hypoxic accidents before intubation of the animal. Methohexital is one of the most short lived barbiturates available [45]. Animals were immediately placed between water heating pads and positioned on their back on a custom made MR compatible animal bed. After treatment of the trachea with lidocain the animals were intubated and mechanically ventilated by an MRI compatible ventilator (Datex Ohmeda Aestiva MRI, Datex-Ohmeda Division Instrumentarium Corp., Finland) with a mixture of 0.30% Isofluorane in air. A forearm vein was cannulated and mivacurium chloride (5.3-6.9 mg/(kg·h)), Fentanyl (2.3-4.1 μg/(kg·h)), and Saline (0.9%vol. at rates between 0 (only in the pilot experiment) and 18 ml/(kg·h)) were infused. This combination of Isofluorane and Fentanyl is typically used in human surgery and was first introduced by Logothetis and colleagues [77] for monkey fMRI. It is known to provide excellent signal quality. To record vital parameters we used an MRI compatible anaesthesia monitor (Datex Ohmeda S5 MRI, Datex-Ohmeda Division Instrumentarium Corp., Finland) that provided monitoring of the electrocardiogram (ECG), non invasive monitoring of oxygen saturation (SpO_2) via infrared pulse oxymetry, breathing gas analysis (CO_2, O_2, Isofluorane) and non invasive blood pressure (NIBP) measurement. In addition, body temperature was measured via a small Pt100 rectal probe. Body temperature, end tidal CO_2 and Isofluorane levels were kept as constant as possible (refer to Table 1) using permanent regulation of heating, Isofluorane settings and stroke rate of the ventilator by an

operator. We used single shot EPI imaging that fully samples the breathing cycle and does not suffer from a within image phase error due to breathing as it is the case for segmented EPI. Thus, we were able to choose a larger stroke volume and low breathing rates (approx. 12 strokes/min) to allow for proper alveolar equilibration of the exhaled breathing gas to ensure correct measurement of end tidal CO_2. To protect the lungs we always used a constant peak end expiratory pressure (PEEP) of 4cm H_2O. We chose to use a slightly elevated body temperature (38.5°C) as our target temperature to compensate decreases in brain metabolism due to Isofluorane [47]. In addition, we used a slightly hypocapnic (target $ETCO_2$= 4.0%) preparation to partially counterbalance the vasodilatation brought about by Isofluorane [81]. Note that both elevated body temperature and slight hypocapnia are of course rather crude global attempts to correct for the influences of Isofluorane on cerebral circulation and metabolism. They were based on results from preliminary experiments and may fail to yield the desired compensation. To protect the animal from scanner noise we placed silicone ear plugs. The pupils were dilated and the ciliary muscles relaxed by administering cyclopentolate to each eye. The non stimulated left eye was closed and covered using a saline soaked pad. A contact lens (Wöhlk-Contact-Linsen GmbH, Germany) was placed in the stimulated eye to protect the cornea and to ensure that the focal plane was at the location of visual stimulus presentation. Irrigation of the eyes with either cyclopentolate or saline was repeated after each functional MRI scan to prevent drying of the cornea. To avoid stress induced by the need to urinate the bladder was emptied when necessary by massaging the lower abdomen. When using FiO_2 of 90% for more than two hours we used a period of 10 strokes at elevated peak end expiratory pressure (8 cm H_2O) after the end of each run to avoid any risk of atelectasis.

1.2.3 Stimulation

Figure 1.1 presents the stimulus paradigm and the stimulation setup. We used a black and white concentric checker board with spatial frequency approximately scaling according to cortical magnification and reversing contrast at 8 Hz. Stimulation for one experimental run consisted of one block of 28 seconds of a blank screen baseline (these data were discarded in later analysis) followed by 23 blocks of 24 seconds of presentation of the checker board and 24 seconds of blank screen. The position of the foveal field of view on the stimulus screen was estimated by back projecting the blind

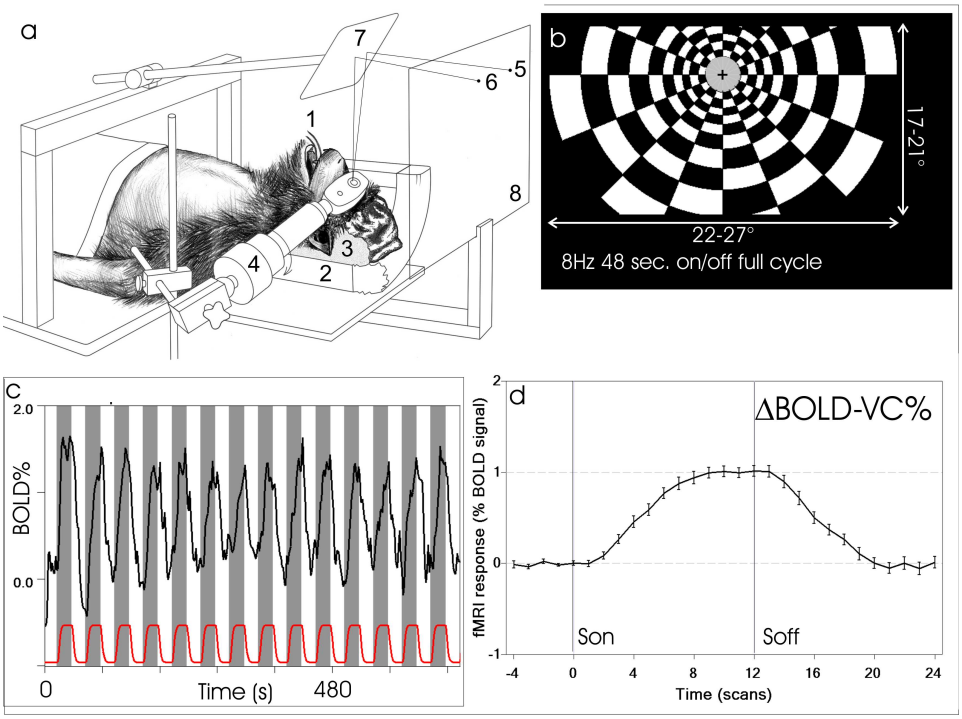

Figure 1.1: *Stimulation setup and single trial responses (a) Setup: (1) breathing gas supply, (2) RF coil (cut, 1/4 shown), (3) vacuum pad, (4) 180° reversible ophthalmoscope, (5) measured position of blind spot, (6) estimated position of fovea at 14° visual angle from blind spot - the stimulus centre is positioned at this location, (7) mirror, (8) back projection screen (b) Schematic drawing of the visual stimulus. The visual angle covered by the stimulus display varied from 22° (horizontal) x 17° (vertical) to 27° x 21° depending on the distance between monkey, mirror and stimulation screen. The cross in the stimulus centre indicates the estimated position of the foveal field of view. We predominantly stimulated the lower visual field to obtain reliable activation in areas without susceptibility artefacts. (c) Single trial BOLD responses: ΔBOLD% in % of baseline BOLD signal (black) and normalized model hemodynamic response function (red, arbitrary units) versus EPI-volume. Baseline epochs are marked in white, stimulation is marked in grey. (d) Single run average over 23 stimulation epochs. ΔBOLD% in % of baseline BOLD signal versus time counted in EPI volumes (1 TR = 2 sec.). Son and Soff denote onset and offset of the stimulus. Error bars denote one standard error. Part (a) of this figure courtesy of K. Melnikovic.*

spot of the eye via a custom made reversible ophthalmoscope and subsequent calculation of the foveal position using a visual angle of 14°. The stimulus was centred on this position. Due to limitations of setup geometry and fMRI imaging (susceptibility artefacts induced by the petrous bone) we concentrated on presenting the stimulus optimally in the lower visual field, thus activating the dorsal parts of visual cortex more than the ventral parts. Lateral extension of the stimulus was 22°-27° of visual angle, symmetrically around the fovea; vertical extension was 17°-21° of visual angle predominantly in the lower visual field. As the stimulus was seen through the opening of the standard 18 cm birdcage coil small parts of the visual field were occluded by the rungs of the coil in some of the sessions. The retinotopically corresponding regions in visual cortex were excluded from further analysis.

1.2.4 MR Imaging and fMRI Data Analysis

All experiments were performed in a 3 Tesla magnet (Magnetom Trio, Siemens Medical Solutions, Erlangen, Germany) equipped with a standard 18 cm birdcage coil. A second order shim localised on occipital cortex including the upper portion of the superior temporal sulcus was performed. T1 weighted images were acquired with a 3D magnetisation prepared rapid gradient echo (MPRAGE) sequence (TE 3.9 ms, TR 2250 ms, voxel size 0.5 x 0.5 x 0.5 mm^3). For fMRI experiments volumes of 20-23 slices (simply referred to as volume in the following) were acquired using single shot EPI (TR 2000 ms, TE 30 ms, matrix size 128 x 88, FOV 103 x 150 mm^2 to 115 x 168 mm^2 - depending on the size of the monkeys head, resulting pixel size (1.17 mm)^2 to (1.31 mm)^2, slice thickness 1.9 mm). To achieve the desired echo time we used partial Fourier acquisition (75% of k-space covered). To avoid arterial inflow artefacts we chose a flip angle of 70° which is well below the calculated Ernst Angle of 77° for a TR of 2000 ms at 3 Tesla. To account for shortened T2* when using microcrystalline ion oxide nanoparticles as an exogenous contrast agent (MION, [117]) we shortened the echo time to 25 ms and had to decrease inplane resolution to 1.5 x 1.5 mm^2 in the MION experiment. An experimental run consisted of 540 volumes (540 x 2000 ms = 1080 s). In a typical experimental session (1 day) monkeys stayed in the scanner for 10 hours and 10-14 runs were acquired.

Functional imaging data analysis was performed in BrainVoyagerQX (www.brainvoyager.com), using standard pre-processing including slice scan time correction, sub millimetre motion correction with between run coreg-

istration using sinc interpolation, spatial smoothing with a 2 mm gaussian kernel, linear trend removal, temporal high pass filtering at 0.01 Hz and temporal smoothing with 4 seconds FWHM (= 2 x TR). fMRI datasets were coregistered to the anatomical image. From the coregistered fMRI slice datasets volume datasets for 3D analysis were created. For each experimental session (1 monkey, no removal from scanner) we pooled all functional data[1] and performed a group general linear model (GLM) analysis by using the box car on-off cycles of visual stimulation convolved with a standard hemodynamic response function [11] as a predictor. We then defined regions of interest (ROI) for each experimental session by accepting all voxels that were significant at $p < 0.001$ (Bonferroni corrected for multiple comparison and corrected for serial correlation) if they additionally were part of a cluster of at least 20 voxels. For each individual run of a session we then extracted time courses averaged separately over all voxels in each of the different ROIs defined by the session GLM with the thresholds given above. Average BOLD signal amplitude for the corresponding two volumes before onset of each single stimulus was defined as the respective baseline for this stimulus repetition. BOLD response amplitudes where calculated relative to this local baseline and subsequently averaged over the 23 stimulus repetitions of a single run to get the amplitude and standard deviation of ΔBOLD% (regionally specific ΔBOLD% is from hereon denoted ΔBOLD-VC% and ΔBOLD-LGN% for visual cortex and the LGN, respectively).

1.2.5 Pilot Experiment: Influence of Anaesthesia Parameters and FiO_2

This experiment was designed to investigate the influence of the recorded anaesthesia related covariates and to detect a potential time independent linear effect of FiO_2 levels on ΔBOLD%. To this end we recorded for each run the initial dose of Methohexital, time elapsed since injection of Methohexital, dose of Fentanyl, dose of Mivacurium chloride, dose of saline infusion, systolic NIBP, heart rate measured by pulse oxymetry, body temperature at start and end of run, $EtCO_2$ and end tidal fraction of the anaesthetic agent Isofluorane (further on abbreviated as FeAA). In addition, we systematically varied FiO_2 of the breathing gas. We then used the per run averages of these variables for further analysis. After a change in FiO_2 we waited for 40 min for the organism to equilibrate before starting the next

[1] Pooling of the datasets was done by concatenating the data in the time dimension before performing the GLM analysis.

fMRI acquisition. To further account for longer term hysteresis effects not covered by the 40 min equilibration time we used both possible transitions (i.e. from low to high FiO_2, and from high to low FiO_2) in our design in a balanced manner (table 1.1).

FiO_2 schedule			
FiO_2-level	Sequence: rising	Sequence: identical	Sequence: falling
20	n.a.*	7	8
30	6	n.a.**	8
50	6	n.a.**	4
80	4	n.a.**	0
90	10	n.a.**	n.a.***

Table 1.1: *FiO_2 schedule. For each level of FiO_2 in the pilot experiment this table lists the number of times it was reached while increasing FiO_2 or else decreasing it. (n.a.) denotes categories not applicable for one of the following reasons: * As no hypoxia was used in our experiments the level of 21% FiO_2 could only be reached from an higher or equal FiO_2. ** Because time constants of FiO_2 effects were not measured in the pilot experiment (but compare results of the time course experiment) we chose not to count repetitions of levels of FiO_2 as identical in this table but rather to attribute them to rising or falling FiO_2 depending on whether the last differing level of FiO_2 was below or above the current level respectively. *** Due to limits of our gas supply it was impossible to reach FiO_2 of 100%, thus the level of 90% FiO_2 only appeared on the rising slope.*

1.2.6 Time Course Experiment

This experiment was designed to investigate the time course of variations in ΔBOLD% in reaction to changes in FiO_2. Before acquiring data for this experiment, we monitored BOLD fMRI responses of the monkey in the scanner using the checkerboard stimulus described above and real time data analysis provided by the TurboBrainvoyager software package (www.brainvoyager.com) in combination with real time data export from the scanner [116, 115]. After waiting for 300 minutes (two half lives of the barbiturate Methohexital that was used for anaesthesia induction) we acquired 2-4 fMRI runs at FiO_2 of 21% (room air) followed by a switch to an FiO_2 of 90% and subsequent acquisition of fMRI runs up to a total length of anaesthesia of 720 minutes (26 runs). Alternatively, to investigate the far end of the time course in

response to hyperoxia, we switched to an FiO_2 of 90% either immediately after anaesthesia induction or after 300 min had elapsed since induction of anaesthesia (29 runs). In the latter case the switch took place immediately before starting fMRI data acquisition for this experiment. Thus, we were able to record data up to durations of 480 minutes after switching to hyperoxia, covering the complete time course relevant for fMRI under long term anaesthesia. No single session alone covered the entire duration of hyperoxia presented here, due to the necessary waiting period of 300 minutes that had to be interposed before obtaining stable data and the length of 480 minutes under hyperoxia. In sum these times exceeded our chosen limit for continuous anaesthesia (12 hours). In addition, to allow for a differentiation of the factors *time since anaesthesia induction* and *time elapsed since switch to hyperoxia*, we also performed sessions where FiO_2 was kept constant at 21% (29 runs).

1.2.7 Retest Experiment

The aim of this experiment was twofold: First, we wanted to strongly vary the timing of the experiment with respect to the circadian rhythm of the animal to prove independence of any observed effects from this rhythm. Second, we aimed to replicate our experimental results from the time course experiment in an animal that had not been available at the time of the time course experiment. Therefore, we measured one additional monkey (J, male, 4.2 kg) with stimuli and hyperoxia identical to the time course experiment, however, shifting the beginning of the experiment by roughly 7 hours with respect to the mean onset of the time course experiments. After an interval of 540 minutes following the induction of anaesthesia the data acquisition began with two normoxic baseline runs followed by the switch to hyperoxia (FiO_2=90%) and acquisition of 8 runs to follow the time course of hyperoxia effects for 270 minutes. This required continuous anaesthesia for 16 hours. Data analysis for this experiment was performed in exactly the same way as for the time course experiment to allow for a later pooling of data from both experiments.

1.2.8 MION Experiment

In this experiment we first recorded and analysed ΔBOLD% in real time as in the preparatory phase of the time course experiment. When a stable signal appeared we recorded the transversal relaxation rate R_2^* (cf. below), and a BOLD fMRI reference run. After this MION was administered IV

in a physiological phosphate buffered saline solution at a dose of approximately 9-11 mg (MION)/kg. We then acquired 2-4 functional EPI runs with MION at FiO_2 of 21% followed by 2-6 runs at FiO_2 of 90%. To account for an elimination of MION from the blood pool (the typical half-life of MION effects [75] is comparable with the typical length of our experiments) we first obtained an estimate of R_2^* before and after injecting MION and then after each fMRI run by acquiring single shot EPI scans using the same slice positions and resolution as in the functional runs but with 6 different echo times (25, 30, 35, 45, 55, 65 ms). We extracted the average whole brain signal from several slices and fitted a mono exponential decay function to obtain either $R_{2baseline}^*$ for the runs prior to MION injection or $R_{2total}^*(t) = R_{2baseline}^* + R_{2MION}^*(t)$ after injection of MION. MION elimination from the blood pool was then modelled by fitting a mono exponential decay function over time to the recorded $R_{2MION}^*(t)$ data to extract the half life of the removal process. This fit was then resampled to get the exact $R_{2MION}^*(t_{midrun})$ contributed at the middle of an fMRI run. A ROI was determined for each session by calculating a GLM of all runs with MION using inverted boxcar predictors and thresholding at $p < 0.05$ (Bonferroni corrected for multiple comparison and corrected for serial correlation). We then calculated the average relative response over all voxels inside this ROI and over all repetitions of the stimulus in each given run as in our BOLD fMRI analysis. The response curves obtained for each run were then subjected to global scaling using $R_{2MION}^*(t_{midrun})$ as described in [75] and subsequently normalised to the respective baseline values obtained at normoxia in the same session. The globally rescaled and normalised response amplitudes were analysed with respect to the influence of time under hyperoxia. The experiment was repeated in two monkeys.

1.2.9 paO_2 Experiment

Animal preparation, hyperoxic ventilation schedule and fMRI data analysis for this experiment were performed identically to the retest experiment. We measured two monkeys (J, P). Under normoxic baseline conditions and under hyperoxic ventilation conditions arterial blood samples were drawn at regular intervals from a catheter placed in the right femoral artery and paO_2 was measured using a blood gas analyser (Radiometer ABL800 flex, Drott Medizintechnik GmbH, Vienna, Austria). The covered time interval spanned from 414 minutes before the onset of hyperoxic ventilation to 332 minutes post the onset of hyperoxic ventilation.

1.2.10 Statistical Analysis for Confound Identification

To maximise statistical power for the identification of potentially influential confounds we pooled two datasets: All data from the pilot experiment and those runs from sessions of the time course experiment where FiO_2 was not varied but instead kept at room air level (this combined dataset is further on denoted as extended pilot experiment). These data were then analysed by linear regression using the inclusion method and the factors: dose of Methohexital, body temperature, $EtCO_2$, time since anaesthesia induction, heart rate, dose of mivacurium chloride, saline infusion rate, end tidal fraction of the anaesthetic agent (termed FeAA, the agent used was Isofluorane), systolic NIBP, FiO_2 level and a second order term for the known synergistic interaction between Isofluorane and Fentanyl (FeAA·Fentanyl) [82].

1.2.11 Statistical Analysis of Time Course Data

To ensure maximum protection from the effects of confound variables identified in the pilot experiment we discarded all runs where variations in the values of these confound variables were below the 15^{th} percentile or exceeded the 85^{th} percentile of any given confound variable. The resulting rejection limits for extreme values in the confound variables are given in table 1.2. Of course, even tighter restrictions would be desirable for improved protection against an influence of confounds. However, even at the current choice of rejection limits the number of data points were in the worst case reduced by a factor of 0.7 per considered confound variable. We, therefore, chose the tightest possible limits that still allowed for a time resolved post hoc analysis. Data were then subjected to the same multiple linear regression analysis as in the pilot study, this time, however, including the time elapsed since the switch to an FiO_2 of 90% (TIME-O2-90) and its square (SQTIME-O2-90) as additional predictors (note that these predictors were not applicable in the pilot experiment). This ensures that any residual influence of confounds does not go undetected while at the same time providing first and second order time dependence measures for the effects of hyperoxia. The inclusion of the square of time elapsed since the switch to FiO_2 of 90% (SQTIME-O2-90) allows for the detection of biphasic temporal modulations as they would be brought about for example by two competing pathways of interaction between oxygen and hemodynamic responses. Finally, to describe the time course of the effects of hyperoxia in detail we performed an ANOVA for a significant influence of the factor time and subsequent post hoc tests (pair wise exact Mann Whitney U) to detect in which time bins BOLD fMRI response

amplitudes under hyperoxia varied from their baseline values acquired at normoxic conditions.

1.3 Results

1.3.1 Physiological Parameters

Table 1.3 presents an overview of the full range, means and standard deviations of physiological parameters recorded during the total of 148 experimental runs (each comprising 23 stimulus repetitions) in the pilot experiment and the time course experiment. Some extreme values of physiological parameters were not suitable for recording ΔBOLD% and experiments were always immediately stopped upon their occurrence. The recorded means, however, represent a reliable anaesthesia regime for BOLD fMRI in the primate.

1.3.2 BOLD fMRI Responses to Visual Stimulation

In all sessions we were able to obtain regions of interest (ROI) for positive ΔBOLD% at a threshold of $p<0.001$ (Bonferroni corrected for multiple comparison and corrected for serial correlation) in the lateral geniculate nucleus (LGN, ΔBOLD-LGN%) and the retinotopic visual areas V1/V2/V3 (ΔBOLD-VC%). A typical single trial BOLD fMRI time course and an averaged response from 23 stimulus repetitions (one run) from monkey K are presented in figure 1.1. Figure 1.2 presents the typical extent of the ROIs in anatomical sections and projected onto the left hemisphere of the reconstructed cortical surface of monkey K.

1.3.3 Extended Pilot Study - Identification of Confounds and of FiO_2 Level Effects

In the extended pilot experiment using a temporally balanced schedule of FiO_2 changes we did not observe an influence of the level of FiO_2. The identified confound variables together with their effect sizes are listed in table 1.2. Table 1.2 also lists the resulting limits for influential confound variables that were later used for protecting experimental results of the time course experiment from confounding effects. Note that we found an effect of the time elapsed since the induction of anaesthesia (figure 1.3). Detailed investigation revealed this to be likely an effect of the anaesthetic Methohexital used for anaesthesia induction. The observed process had a half-live be-

Identification of Influential Confound Variables					
Identified Confound Variable [unit]	Coefficient [BOLD% / unit]	Beta**	p	lower rejection limit	upper rejection limit
time since anaesthesia induction [minutes]	0.001	0.53	0.001	n.a.*(300)	n.a.*(-)
Body Temperature [°C]	0.6	0.39	0.004	38.34	38.60
Fentanyl dose [μg / (kg·h)]	10.8	5.60	0.025	2.95	3.01
Interaction Fentanyl · Isofluorane [% ·μg / (kg·h)]	-36.4	-8.26	0.030	0.79	0.91
Methohexital Dose [mg/kg]	0.030	0.41	0.037	30.17	39.33
Isofluorane (FeAA) [%]	101.799***	5.01	0.040	0.27	0.30

Table 1.2: **: additional analyses indicated that this parameter reflects the washout of the initial anaesthetic Methohexital. We therefore choose to evaluate only data that were recorded later than 300 minutes after the beginning of anaesthesia. ** Beta: coefficient values standardised by the variance of the respective predictor observed in our experiments: beta values should reflect the importance of a confound variable for our data better than the raw coefficients.***: This large positive coefficient for the level of Isofluorane is most likely due to an overestimation of the Fentanyl · Isofluorane interaction predictor. In fact a level of approximately 3 $\mu g(Fentanyl)/(kg{\cdot}h)$ as it was present in our experiments results in the expected overall negative dependency of $\Delta BOLD\%$ on Isofluorane levels.*

Physiological Parameters			
	mean s.d.	Range*(min-max)	measured in n runs:
Body Weight [kg]	7.51.6	5.7 - 9.7	all
NIBP systolic [mmHg]	120.5±23.5	84 - 172	128
SpO_2 [%]	99±3	**	121
$EtCO_2$ [%]	4.00±0.09	3.75 - 4.25	148
FeO_2 [%]	n.a.***	21.4 - 90.3	148
Pulse rate [beats/min]	129±17	84 - 158	121
Anaesthesia Parameters			
Methohexital dose [mg/kg]	36.1±4.7	30 - 45	all
Isofluorane level inspiratory [%]	0.30±0.01	0.26 - 0.32	all
Fentanyl [g/(kg·h)]	3.0±0.2	2.3 - 4.1	all
Mivacurium Chloride $[mg/(kg \cdot h)]$	6.3±0.3	5.6 - 6.9	all
Saline 0.9%vol [ml/(kg·h)]	11.1±4.4	1.0 - 17.4	all
total infusion rate of liquids [ml/(kg·h)]	16.3±4.5	6.0 - 22.8	all

Table 1.3: *This table gives an overview of recorded physiological and anaesthesia parameters in the pilot experiment and the time course experiment. We list mean, standard deviation and minimum to maximum range of all recorded data (pilot experiment and time course experiment). For some of these variables exceptions apply: * Some of the values given as ranges here may indicate a risk to the animal and warrant immediate interruption of the anaesthesia. **Deviations in this parameter were due to device malfunction **** FiO_2 *and hence* FeO_2 *were systematically varied in both experiments.*

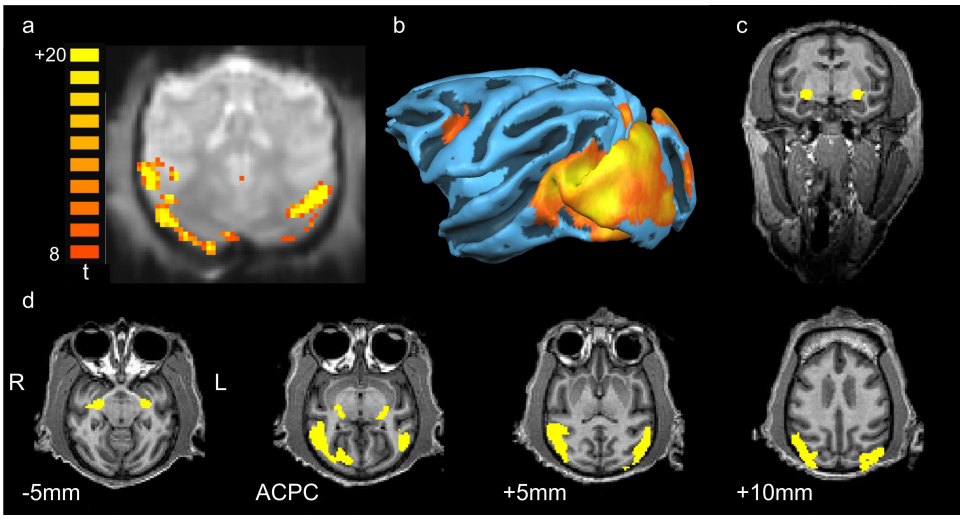

Figure 1.2: *Localisation of ROIs. (a) Single shot EPI image with overlaid single run (Monkey K, run ID 040) t-statistics for activation in visual cortex, thresholded at $t > 8$. Colour scale denotes t values. (b) Reconstructed cortical grey/white matter boundary with overlaid cortical activation from group GLM analysis comprising data from one session. (c) Localisation of ROI in the LGN overlaid on a coronal section of a T1 weighted anatomical (MPRAGE) image. (d) Localisation of ROIs in visual cortex and LGN on a series of transversal sections on or parallel to the ACPC plane, coordinates indicate distance to ACPC plane (+ = dorsal; R=right; L=left). The slight asymmetry of the ROI in visual cortex in this case is most likely due to occlusion of parts of the visual field by rungs of the MRI coil. Note that the upper half of the occipital operculum shows stronger activation (see panel b), an indicator of the predominant stimulation of the lower visual field. However the extent of activated cortex in this case also implies considerable stimulation of the upper visual field.*

tween 67 and 138 minutes (mono exponential fit, simulating the washout of active Methohexital from a biological compartment). We, therefore, chose to limit our data analysis for the subsequent time course experiment to data recorded later than 300 minutes after induction of anaesthesia. Also note that the identification of influential confounds holds for the particular limits of accuracy in controlling parameters of anaesthesia and physiology in our experiment.

1.3.4 Time Course Study - Time Dependent Hyperoxia Effects in Visual Cortex

Figure 1.4 (b) displays average stimulus induced BOLD response curves at various times under hyperoxia. The amplitude of BOLD responses was decreased for data averaged over the interval 1-180 minutes post onset of hyperoxia. Statistical significance of this result was verified using multiple regression analysis (table 1.4). Multiple regression analysis revealed that only the time elapsed since switching to FiO_2 of 90% was present as a significant factor in the ΔBOLD-VC% data of the time course experiment. The negative sign of the linear term in time (TIME-O2-90) and the positive sign of the second order term (SQTIME-O2-90) indicate the presence of a biphasic modulation consisting of an initial drop of ΔBOLD-VC% and a later recovery. The absence of significant effects of confound variables on ΔBOLD-VC% confirms that their influence is successfully controlled by our conservative exclusion limits. It should be noted, however, that a small residual influence of $EtCO_2$ may have been present ($p < 0.12$). To clarify when the drop in ΔBOLD-VC% and the later recovery took place in time we performed a one-way ANOVA with factor TIME-O2-90 and subsequent post hoc testing. To allow post hoc testing with sufficient data points per time bin we had to choose a rather coarse binning (binwidth: 180 min, bins: bin 0 = baseline data, bin 90 = centred at 90 min of hyperoxia, bin 270 = centred at 270 min of hyperoxia). We found a significant influence of factor time ($p < 0.007$). Post hoc tests indicated significant differences of bin 0 versus bin 90 ($p < 0.002$, pair wise exact Mann Whitney U) and bin 90 versus bin 270 ($p < 0.04$, pair wise exact Mann Whitney U), whereas no significant difference was found between bin 0 and bin 270. These results are presented in figure 1.4(d). Note that binning was necessary only for post hoc testing. The existence of time dependent hyperoxia effects was, however, confirmed *independently* by the multiple regression analysis. Time course effects were, thus, not an artefact of binning. For exploratory use

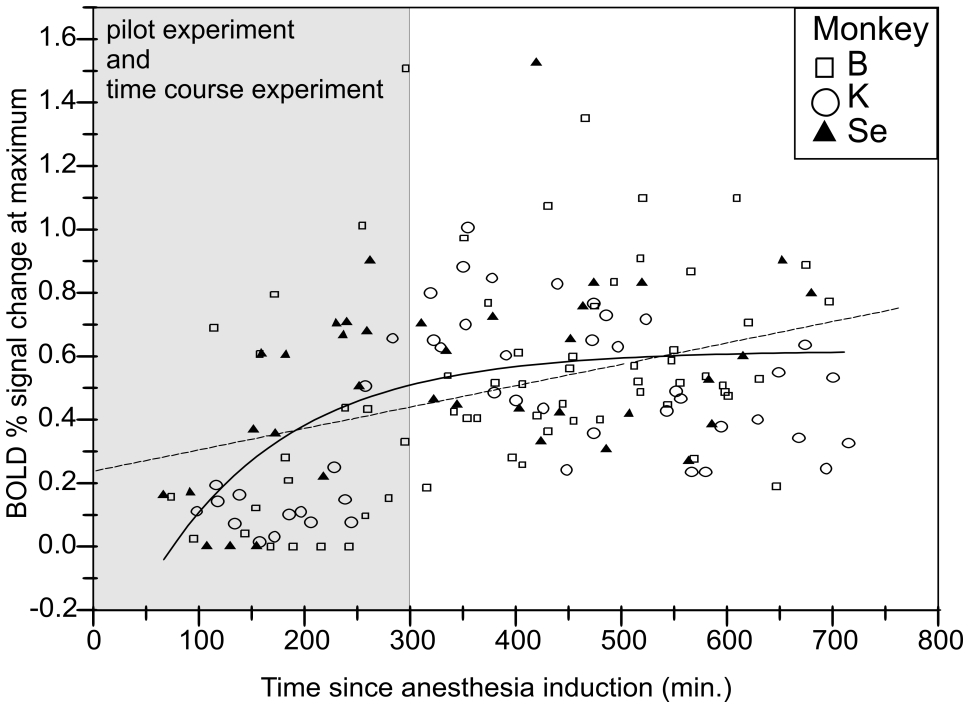

Figure 1.3: *Bold peak amplitudes from single runs in visual cortex versus time elapsed since injection of the barbiturate Methohexital in minutes. Data are pooled from the pilot and the time course experiments. Data symbols: open square - monkey B; open circle - monkey K; solid triangle - monkey Se. Dashed line: linear fit of the data,* $R^2 = 0.14$*; solid line: exponential relaxation fit of the data:* $\Delta\text{BOLD}\%(\text{t}) = \Delta\text{BOLD}\%_{\max}(1-\exp(\text{ct}))$*. The resulting correlation was* $R^2 = 0.23$*; the estimated rate constant c was* $0.0077 \pm 0.0028\text{min}^{-1}$*. The resulting half-life of the exponential relaxation is between 67 and 138 minutes. Note the saturating character of the development of BOLD amplitudes over time. Also note that data are under the influence of another 9 independent factors, which explains the large amount of variance not accounted for by the fitted models. The grey box indicates the rejection criterion: data acquired before 300minutes (approx. 2 half-lives) are considered contaminated by the influence of initial anaesthesia.*

we also provide a plot of the unrestricted data at a smaller bin width to demonstrate that time dependent hyperoxia effects were qualitatively similar in the unrestricted dataset, independent of bin width (figure 1.6 c, d)

1.3.5 MION Functional rCBV Results in Visual Cortex

The estimated MION half-life varied between 12 minutes and 243 min (Monkeys K/M/P/S: 12 / 50 / 207 / 243 minutes). In one of the monkeys (monkey S), injection of MION in phosphate buffered saline produced a transient rise in blood pressure above 170 mmHg. This was most likely due to the amount of administered fluid. Data obtained during this period were excluded from analysis. One further run from one monkey (S) had to be excluded due to an $EtCO_2$ above 4.1%. In monkey M one run had to be discarded due to large signal jumps in the time course, most likely due to an instability of the RF chain of the MR scanner and measurements were discontinued after the appearance of this artefact. Figure 1.5 b presents the results of time resolved analysis of MION fMRI response amplitudes in visual cortex in response to hyperoxia. Pooled globally scaled and baseline normalised MION response amplitudes in visual cortex (Figure 1.5, b) showed a significant decrease ($p < 0.043$ Mann-Whitney U) of functional rCBV response in the time bin from 1 to 180 minutes after the onset of hyperoxia (bin 90; n=15) by 23%. This is consistent with the observed drop in response amplitude for ΔBOLD-VC% in the same time interval.

1.3.6 Time Course Study - Time Dependent Hyperoxia Effects in the LGN

When analysing BOLD fMRI response amplitude from LGN using the same multiple regression analysis that was used for the analysis of cortical signals we neither found an effect of TIME-O2-90 nor an effect of SQTIME-O2-90 (table 1.5). ΔBOLD-LGN% was only significantly modulated by small residual influences of $ETCO_2$ and Body Temperature.

To exclude the possibility that hyperoxia effects in the LGN were missing due to insufficient contrast to noise ratio (CNR) we computed the average ΔBOLD% response curves and the average standard error of the response over stimulus repetitions at each timepoint of BOLD response curves, both, for visual cortex and the LGN. The standard errors were then averaged over all timepoints and runs for the visual cortex and the LGN separately. The ratio of average ΔBOLD% and the average standard error for each region then served as a measure for the respective CNR. We obtained only a very

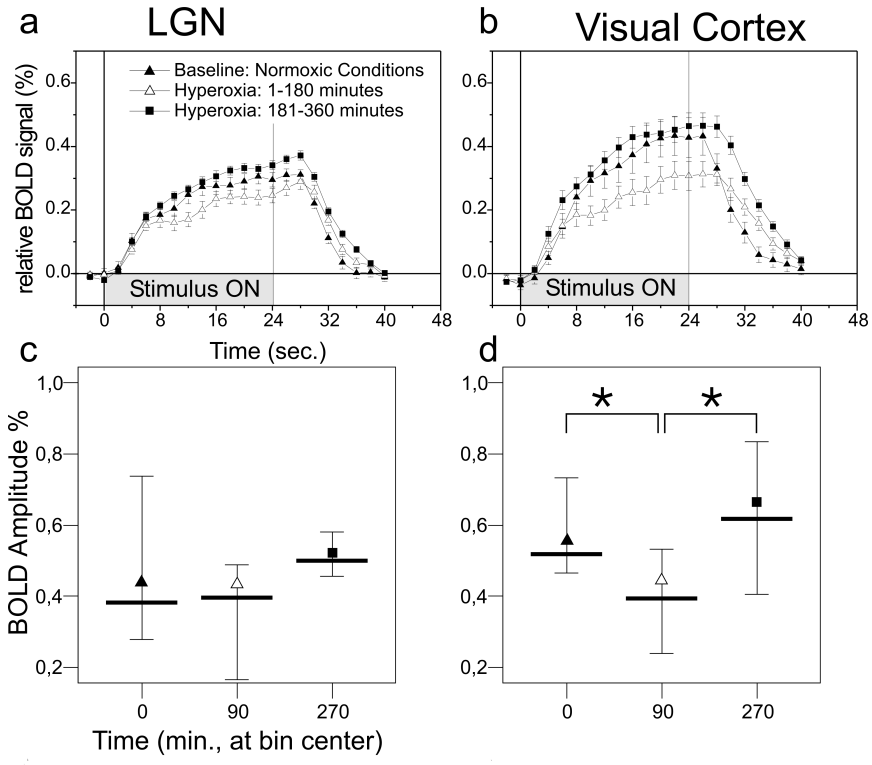

Figure 1.4: *BOLD fMRI results: (left: a, c) results for the LGN, (right: b, d) results for visual cortex. (a,b) BOLD signal vs. time under stimulation: Average BOLD response curves for different bins of time elapsed under hyperoxic ventilation (FiO_2 = 90%): solid triangle - baseline conditions (normoxia), open triangle - 1 to 180 minutes under hyperoxia, solid triangle - 181 to 360 minutes under hyperoxia. Error bars denote one standard error of the mean. All data are recorded later than 300 minutes after injection of Methohexital. (c,d) Plot for relative peak BOLD response amplitudes binned over the time intervals given in (a,b) as indicated by the corresponding symbols. The horizontal bars indicate the median values, error bars denote total range in a given bin. Median values for relative peak BOLD response amplitudes in visual cortex are: 0.52 (bin0); 0.36 (bin90); 0.62 (bin270). Bars connect significantly different bins (* denotes a bin pair wise* exact *Mann Whitney U test, $p < 0.05$). These data are restricted by removal of the 15% lowest and 15% highest values of influential confound variables (cf. table 1.2). Numbers of data points per bin of the restricted dataset: bin 0=9, bin 90=8, bin 270=3.*

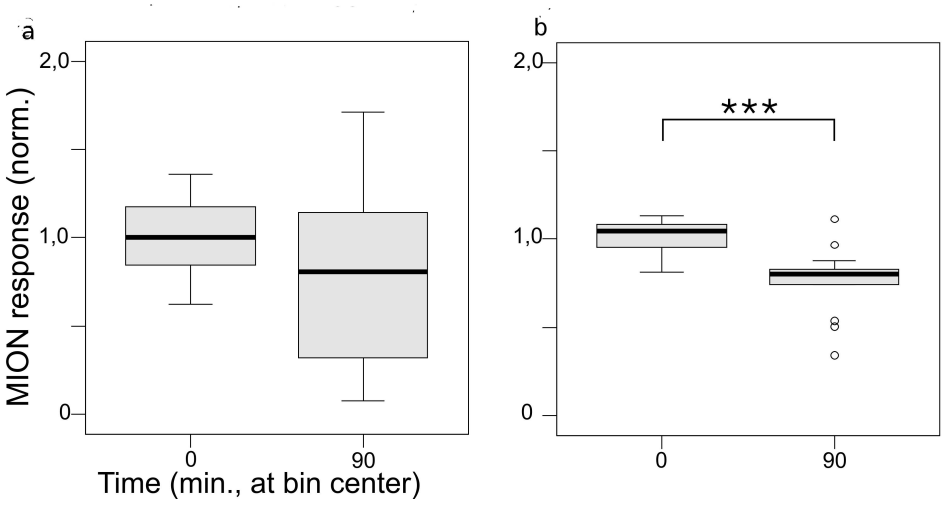

Figure 1.5: *MION fMRI results for LGN and Visual Cortex: (a) results for the LGN, (b) results for visual cortex. All error bars indicate the run to run variability. (a,b) MION response amplitudes normalised by baseline response amplitude versus time. Data are pooled in time corresponding to the first two bins in figure 1.4 (c,d). *** Asterisks denote statistically significant differences to baseline ($p < 0.043$ Mann-Whitney U). Shaded boxes indicate the $25 - 75^{th}$ percentile range. Bars denote the full range of values except statistical outliers. Circles indicate outliers. Number of data points per bin: bin 0=9; bin 90=15. Note the significant decrease in MION response amplitude for the visual cortex (b) between 1-180 minutes (bin 90).*

Significant Variables			
Name [units]	Coefficient [ΔBOLD-VC% / unit]	Beta	p
(time elapsed since FiO_2 switch)^2 SQTIME-O2-90 [minutes^2]	$7 \cdot 10^{-6}$**	2.36	0.001
time elapsed since FiO_2 switch TIME-O2-90 [minutes]	-0.002*	-1.98	0.004
Excluded Variables			
Name	Coefficient [ΔBOLD-VC% / unit]	Beta	p
$EtCO_2$			0.104
time since anaesthesia induction			0.176
Heart Rate			0.249
Dose of Mivacurium Chloride			0.343
Saline Infusion Rate			0.523
FeAA (Isofluorane)			0.536
FeAA·Fentanyl			0.557
NIBPsys			0.576
Fentanyl			0.590
Methohexital Dose			0.605
Temperature			0.693

Table 1.4: *Multiple linear regression of ΔBOLD% data from the time course experiment: Visual Cortex. * the negative sign indicates an initial drop in BOLD response amplitudes. ** The small value of this coefficient is compensated by large values of the square of the time elapsed since the switch to an* FiO_2 *of 90%. Significance of this factor is equivalent to a biphasic modulation over time.*

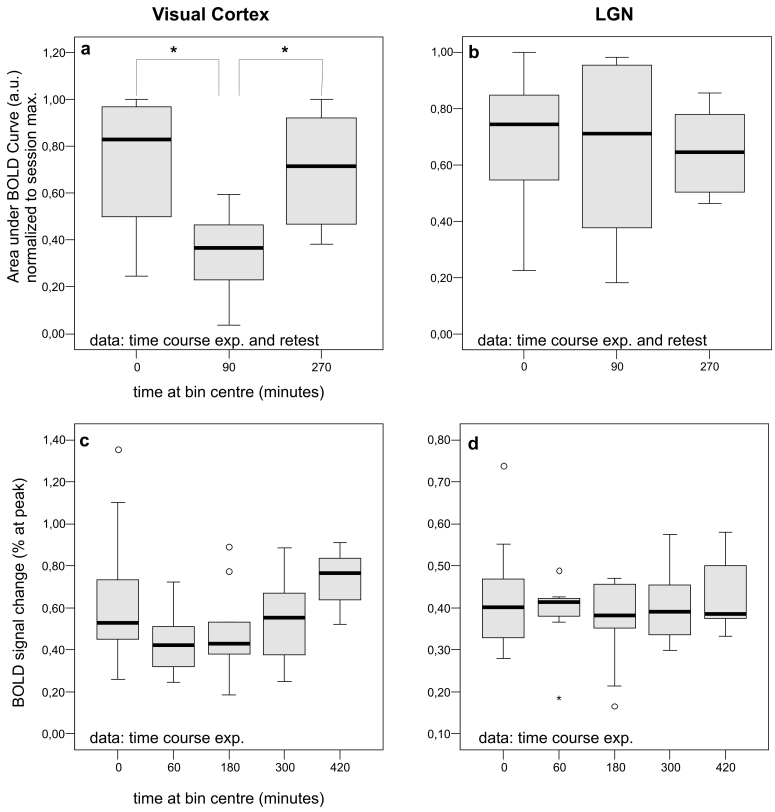

Figure 1.6: *Bin wise plot of combined data of time course and retest experiments and data of the time course experiment at higher temporal resolution. Error bars represent ranges. Shaded boxes represent the* 25^{th} *and the* 75^{th} *percentile. Circles and stars denote statistical outliers. Horizontal bars give the median values. (a,b) Pooled data from time course and retest experiments.* $\Delta BOLD\%$ *(area under curve) versus time elapsed under hyperoxia (bins were chosen as in the time course experiment). The BOLD% signal change was normalized to the within session maximum to eliminate between animal variability. * Significant differences at* $p < 0.05$ *(bin pair wise exact Mann Whintney U). (a) Data from visual cortex expressing biphasic behaviour as described for the time course experiment alone. (b) Data from LGN not expressing any significant time dependence. (c,d)* All *Data from the time course experiment that were acquired later than 300 minutes after injection of Methohexital. The data are presented at a higher temporal resolution (bin width 120 min.). These data still contain a considerable amount of variance related to confound influences. (c) Visual cortex: These data demonstrate qualitatively the presence of time dependent hyperoxia effects in the unrestricted data. (d) LGN: No time dependence of the hyperoxia effects.*

small difference in CNR between visual cortex (CNR = 5.45) and the LGN (CNR=5.40).

Significant Variables			
Name [units]	Coefficient [ΔBOLD-LGN% / unit]	Beta	p
$EtCO_2$ [%]	-0.754	-0.553	0.008
Temperature [°C]	1.860	0.529	0.011
Excluded Variables			
Name	Coefficient [ΔBOLD-LGN% / unit]	Beta	p
(time elapsed since FiO_2 switch)^2 SQTIME-O2-90			0.343
time since anaesthesia induction			0.350
(time elapsed since FiO_2 switch) TIME-O2-90			0.405
NIBPsys			0.488
Heart Rate			0.507
Methohexital Dose			0.587
Saline Infusion Rate			0.666
FeAA (Isofluorane)			0.746
FeAA·Fentanyl			0.752
Fentanyl			0.803
Dose of Mivacurium Chloride			0.892

Table 1.5: *Multiple linear regression of ΔBOLD% data from the time course experiment: Lateral Geniculate Nucleus*

1.3.7 MION Functional rCBV Results in the LGN

Globally scaled and baseline normalised MION response amplitudes, pooled over all four monkeys and binned between 1 and 180 minutes under hyperoxic ventilation, did not reveal a significant difference to baseline in the LGN (figure 1.5 a). Note that we also did not observe a modulation of

the BOLD fMRI signal (ΔBOLD-LGN%) in this structure in this time bin. Responses in the time bin from 1 to 180 minutes after the onset of hyperoxia (bin 90) did however show a significant increase in variance ($p < 0.026$, Levene test) in the LGN. Findings in the *LGN* using MION fMRI were opposed to our findings in the *visual cortex* using MION fMRI. Thus, we observe a correspondence of relative BOLD fMRI and MION fMRI signals in both LGN (both measures showed no effect) and visual cortex (decrease of both measures). This suggests that the effects observed in our BOLD fMRI experiment were due to a hyperoxia related modulation of the relative amplitude of the stimulus induced vascular lumen changes.

1.3.8 Results of the Retest Experiment

Results of the retest experiment can be found in figure 1.7. In visual cortex (figure 1.7, a) we found a decrease of the average ΔBOLD-VC% for the interval from 0 to 180 minutes post onset of hyperoxia (bin 90 from the timecourse experiment) by -53% followed by a smaller recovery of the mean for the interval of 180 – 270 minutes (first half of bin 270 of the time course experiment) to a level of 69% of the pre hyperoxia baseline signal. Pooling these data with those from the time course experiment revealed a significant influence of both, the linear term in time (TIME-O2-90, $p < 0.002$) with a negative coefficient and the second order term (SQTIME-O2-90, $p < 0.009$) with a positive coefficient indicating the presence of a biphasic modulation consisting of an initial drop of ΔBOLD-VC% and a later recovery. In the LGN (figure 1.7, b) we observed a slow decrease of ΔBOLD-LGN% over time that did not recover until the end of the measurement. When these data were pooled with the data from the time course experiment and analysed via multiple regression analysis we did not observe a significant influence of time under hyperoxia on ΔBOLD-LGN%. This analysis of ΔBOLD-LGN%, however, indicated a residual influence of $EtCO_2$ ($p < 0.008$) and body temperature ($p < 0.01$).

1.3.9 Results of the paO_2 Experiment

Figure 1.8 presents the results of the paO_2 Experiment. In this experiment paO_2 was monitored in regular intervals to ensure that stable hyperoxia was present at all times of hyperoxic ventilation and that any time dependent effects observed were not due to fluctuations in the level of paO_2 under hyperoxic ventilation. Results obtained in both monkeys (J, P) for ΔBOLD% in the visual cortex (figure 1.8, a) and the LGN (figure 1.8, b) were quali-

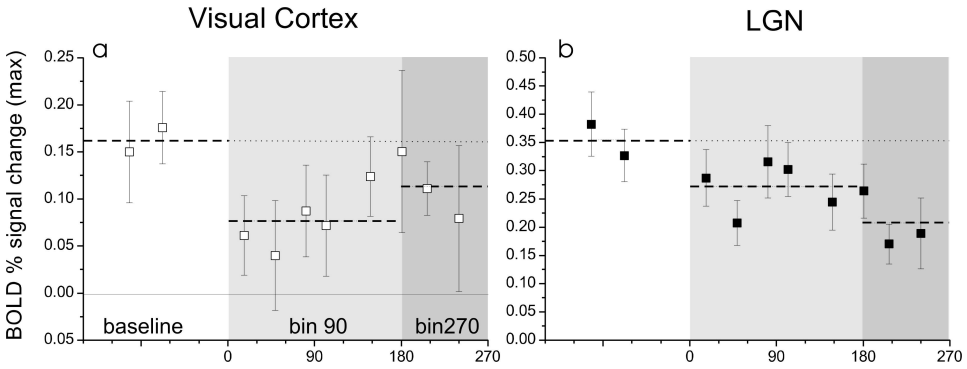

Figure 1.7: *Results of the Retest Experiment. $\Delta BOLD\%$ versus time elapsed since switch to hyperoxia. (a) Data from the visual cortex. Error bars denote one standard error. These data show a marked decrease of ΔBOLD-VC% in the time following the onset of hyperoxia and a later recovery, thus, supporting the results from the time course experiment. When these data were pooled with the data from the time course experiment results on the time dependence of hyperoxia effects (refer to table 1.4) could be replicated using the multiple linear regression analysis. (b) Data from the LGN. Error bars denote one standard error. These data show a slight signal decrease of ΔBOLD-LGN% over time following the onset of hyperoxia, but no later recovery. When these data were pooled with the data from the time course experiment we obtained, however, no significant effect of time elapsed under hyperoxia was found. Leftover significant influences of body temperature and $EtCO_2$ were found, however. This, too, supports the previous findings of the time course experiment. Note that overall amplitudes are generally smaller than in Monkeys B, K and Se due to increased partial volume effects (more inclusion of white matter in cortical imaging voxels) in this particularly small animal.*

tatively similar to the statistical results obtained in the time course experiment: ΔBOLD-VC% showed a transient decrease in the time interval from 0 to 180 minutes post the onset of hyperoxic ventilation and ΔBOLD-LGN% remained more stable. Throughout the whole period of hyperoxic ventilation a stable arterial hyperoxia was maintained with paO_2 levels high above baseline levels (figure 1.8, c; note the vertical axis break). We can therefore exclude the occurrence of hypoxic episodes due to lung injury for the entire duration of the experiment. Furthermore the existing fluctuations in paO_2 under hyperoxic ventilation did not correlate significantly with the observed changes in the BOLD responses in either monkey (figure 1.8, d).

1.3.10 Model Predictions

Table 1.6 presents results for the modulation of ΔBOLD% (given as the ratio $\Delta\text{BOLD}\%_{\text{hyperoxia}}/\Delta\text{BOLD}\%_{\text{normoxia}}$) predicted by our modified deoxyhemoglobin dilution model when switching to hyperoxia (FiO_2=90%). Results are given for various values of hyperoxia induced flow reduction (QCBF:=$\text{rCBF}_{\text{hyperoxia}}/\text{rCBF}_{\text{normoxia}}$, typical values range between 0.67 and 0.87, refer to [68] or [38]), gain of neurovascular coupling (n:=$\frac{\Delta\text{rCBF}}{\text{rCBF}}/\frac{\Delta\text{CMRO}_2}{\text{CMRO2}}$) and strength of neuronal activation in terms of increased energy consumption (ϵ:=$\text{CMRO}_{2act}/\text{CMRO}_{2rest}$). Typical values for the increase in neuronal metabolism under visual stimulation can for example be found in [110] and range between 20% and 40%. The modified DDM (for a derivation see appendix) predicts an increase in ΔBOLD% under hyperoxic conditions compared to normoxic conditions for a variety of values of QCBF (0.67; 0.87; [68, 38]), ϵ (1.05, 1.1, 1.2, 1.5) and n (2-6; n=2 is the low end of measured values [51]; n=4 is derived from a diffusion limited model of oxygen consumption with non-zero mitochondrial O2 concentration [12]; whereas n=6 represents the limit for a diffusion limited model with zero mitochondrial O_2 concentration and also marks the high end of measured values [40]). The predicted modulations of ΔBOLD% (from +19% to +92%) due to hyperoxia are in general higher than those predicted by the classical DDM. Nevertheless even the classical DDM predicted increased ΔBOLD% under hyperoxia, when compared to normoxia (for a derivation see appendix A).

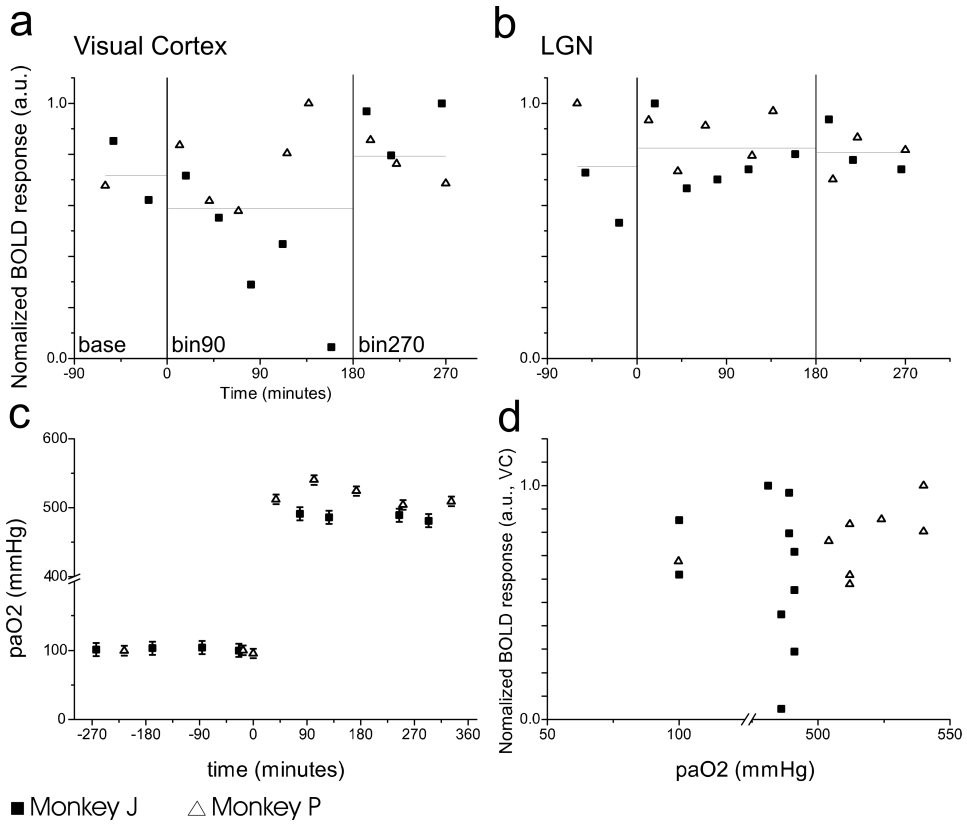

Figure 1.8: *Time dependence of arterial hyperoxia and BOLD response in the* paO_2 *Experiment. (a,b) Baseline normalised BOLD signal change over time under hyperoxic ventilation for two monkeys (J,P). Time points before zero denote the normoxic baseline state. Horizontal bars denote bin mean values. (a) Visual cortex, the same biphasic time dependence as in the time course experiment and the retest experiment is found. (b) LGN, no systematic variation of BOLD signal change with respect to time under hyperoxic ventilation is found. (c) Arterial Hyperoxia (*paO_2*) over time under hyperoxic ventilation. Time points before zero denote the normoxic baseline state. Note that a steady state of arterial hyperoxia is maintained throughout the whole period of hyperoxic ventilation (0 to 360 minutes). (d) Baseline normalised BOLD signal change in visual cortex versus* paO_2*. The association between the amplitudes observed in a BOLD fMRI run and a corresponding* paO_2 *value was made by picking the* paO_2 *value from the blood sampling that was closest in time to the respective BOLD fMRI run. We did not observe a significant correlation between BOLD response levels and fluctuations in the level of* paO_2 *in either monkey.*

Ratio of the Fractional BOLD Response Amplitudes under Hyperoxia and Normoxia: $\frac{\Delta BOLD\%_{hyperoxia}}{\Delta BOLD\%_{normoxia}}$						
$FiO_2 = 90\%$, $PDO_2C = 1.58$ $vol\%$, QCBF = 0.87						
	gain of neurovascular coupling : n					
ϵ*	*2.0*	*2.5*	*3.0*	*4.0*	*5.0*	*6.0*
1.05	1.39	1.28	1.24	1.21	1.20	1.19
1.10	1.41	1.29	1.25	1.22	1.21	1.20
1.20	1.46	1.32	1.28	1.24	1.22	1.22
1.50	1.65	1.41	1.34	1.29	1.27	1.25
$FiO_2 = 90\%$, $PDO_2C = 1.58$ $vol\%$, QCBF = 0.67						
	gain of neurovascular coupling : n					
ϵ*	*2.0*	*2.5*	*3.0*	*4.0*	*5.0*	*6.0*
1.05	1.67	1.57	1.53	1.50	1.49	1.48
1.10	1.70	1.58	1.54	1.51	1.50	1.49
1.20	1.75	1.61	1.56	1.53	1.51	1.50
1.50	1.93	1.70	1.63	1.58	1.56	1.55

Table 1.6: *Predictions made by the modified deoxyhemoglobin dilution model with included plasma oxygenation for the ratio of fractional BOLD fMRI responses under hyperoxia versus normoxia. For a detailed derivation refer to Appendix A. * The parameter ϵ describes changes in neuronal metabolic demand and is dependent on the stimulation used. Literature values for visual stimulation are typically in the range of 1.2-1.4 [110].*

1.4 Discussion

1.4.1 Hyperoxic Ventilation and Arterial Hyperoxia

Long term exposure to increased levels of oxygen in the inspired breathing gas has effects on several parameters of pulmonary function and can, thus, influence pulmonary gas exchange (for a recent review see [16]). Therefore, ventilation of the animal with increased levels of oxygen does not fully guarantee arterial hyperoxia under all circumstances. Sampling of arterial blood during the measurements provided a control for this source of error. We did neither find a systematic decrease of paO_2 over the time interval investigated in the paO_2 experiment nor a significant correlation between paO_2 and ΔBOLD%. We, therefore, exclude low or fluctuating levels of paO_2 as a cause for the observed time dependent effects.

1.4.2 Use of a Standard Hemodynamic Response Template for Model Driven Identification of ROIs

Our results demonstrated that hyperoxia changed cerebral hemodynamic responses. In this light the validity of our approach to identify stimulated Regions of Interest (ROI) using a GLM with predictors build from a standard hemodynamic response template may be questioned. At first sight a definition of ROIs based on anatomical landmarks seems like a valid alternative. However, this approach suffers from the fact that the regions of visual cortex in question are not stimulated entirely due to the limits on stimulated visual angles that can be reached with stimulus projection in the scanner bore. Thus, within one anatomical region activated (stimulated) and inhibited (non-stimulated) parts of cortex neighbour each other. An anatomical definition of ROIs would, therefore, mix data from entirely different brain processes. To probe alternative ways of defining ROIs we have, however, used lag correlation analysis of our data with respect to a boxcar function as a model driven approach with the least possible constraints. Results of this analysis were virtually identical to the standard GLM analysis with a hemodynamic template function (data not shown). In addition we used the model free approach of self organising clustering ICA (sogICA) [35] on 95 datasets from two monkeys (K,B) from the Pilot and the Time Course experiments. ROIs from both approaches were largely overlapping on an individual run basis. The reader may compare for example figures 1.2 (GLM ROI) and 2.39 (single run decomposition with ICA). Details on the sogICA analysis can be found in chapter 2.

1.4.3 Influence of Confound Variables

Results from our pilot experiment indicated that fMRI data recorded in anaesthetised animals may be normally dominated by variations in certain confound variables (table 1.2). In our experiment we found that a restriction of variations in body temperature in a range of 0.5-1°C that is usually found in the literature [119, 31, 76, 102] was insufficient to measure the effects of hyperoxia without serious confound influence, due to the effect size of the factor body temperature on BOLD response amplitudes (approx. 0.6 ΔBOLD%/°C, pilot experiment, visual cortex; table 1.2). Another rather unexpected finding is the long time constant of the effects of the initial anaesthetic Methohexital, which in our study had vascular or neuronal effects influencing ΔBOLD% for up to 5 hours, while its direct anaesthetic action is rather short lasting (5-7 minutes at typical doses used for anaesthesia induction). By discarding data that did not meet our strict criteria on confound variation we could, however, exclude effects of confounds successfully as was demonstrated by the multiple regression analysis. It is worth noting that, for statistical soundness, this procedure requires to identify confound influences from independent data as was done here with data from our pilot study.

1.4.4 Effects of Long Term Anaesthesia

When an organism is exposed to anaesthesia of considerable length, as in this study, the question about the stability of responses over time inevitably arises independent of the experimental manipulation under investigation (hyperoxia). Four measures of precaution were taken in this study to separate effects of hyperoxia from anaesthesia effects: First, we acquired baseline response data (without hyperoxia) over complete sessions, i.e. even for the very late stages of anaesthesia *normoxic* data were analysed. Second, the onset of hyperoxia was jittered with respect to the induction of anaesthesia. Third, time elapsed since anaesthesia induction was kept as a predictor in our multiple regression analysis. This enabled us to detect residual influence of this factor. We did, however, not find a significant contribution. Fourth, in the retest experiment the interval between anaesthesia induction and the onset of hyperoxia was > 540 minutes, introducing yet a bigger jitter than those used in the original hyperoxia experiment to disentangle anaesthesia and hyperoxia effects. Furthermore it should be noted that the anaesthesia protocol used in this study yielded a rather light anaesthesia. On average animals were fully awake and alert roughly 15 minutes after ending the ad-

ministration of anaesthetics. We thus think that the impact of time elapsed under anaesthesia on BOLD fMRI responses did not lead to a systematic error in our results.

1.4.5 Potential Effects of BOLD and MION Signal Baseline Changes

When performing fMRI experiments effects of signal baseline drifts might influence results. We, however, investigated the fractional response amplitudes, relative to an immediately preceding local baseline. While physiological baseline/response effects that are related to the fractional response amplitude are still detectable (and are discussed when trying to explain the failure of the modified Deoxyhemoglobin Dilution Model) simple confounding effects of the physical BOLD signal baseline can be excluded. For our MION experiments measuring the baseline value of $T2^*$ (dominating signal intensity) is actually necessary to calibrate the obtained response amplitudes for the amount of MION present in the blood pool. For the MION experiments presented in this thesis the obtained wash out curves for MION were investigated and no unexpected behaviour was found.

1.4.6 Hyperoxia Effects - Comparison to Model Predictions

The deoxyhemoglobin dilution model (DDM) as derived by Hoge and colleagues predicts an increase in ΔBOLD% for reduced baseline blood flow as it is encountered for example under hypocapnia. A similar reduced baseline blood flow as in hypocapnia was measured under hyperoxia over a wide range of species and physiological states from anaesthetized rats [25] to conscious human subjects [38]. However, the DDM does not apply to this case in a straightforward manner as non negligible concentrations of physically dissolved oxygen in the plasma reduce the proportionality between venous deoxyhemoglobin concentration ($[\mathrm{dHb}]_{\mathrm{venous}}$) and $CMRO_2$ to a mere linear dependency with an offset. This is due to the fact that physically dissolved oxygen is metabolized first before significant dissociation of oxygen from haemoglobin can occur. Thus, the equation used by Hoge and colleagues to describe [dHb]venous must be replaced by (for a derivation see appendix):

$$[dHb]_{venous} = \frac{1}{4} \cdot \frac{CMRO_2 - PDO_2C \cdot rCBF}{rCBF} \tag{1.1}$$

Here PDO_2C denotes the concentration of physically dissolved oxygen in the blood plasma. PDO_2C is around 1.5-1.8vol% at FiO_2 100% [98]. When choosing a PDO_2C of 1.6vol% for FiO_2 of 90% our modified DDM (mDDM)

predicts a relative increase of ΔBOLD% due to hyperoxia between 19% and 92%, depending on the chosen values for the reduction in rCBF under hyperoxia (QCBF), for the increase in neuronal metabolism by stimulation (ϵ) and the gain of neurovascular coupling (n).

Surprisingly our data were neither in accord with the predictions made by the modified deoxyhemoglobin dilution model, nor with those made by the classical DDM. We observed no change in ΔBOLD% in the LGN. In visual cortex we observed a temporary decrease of ΔBOLD% which was the opposite of our predictions. Responses in visual cortex were first reduced for data averaged from onset of hyperoxia to 180min, later recordings showed a recovery to pre-hyperoxia baseline amplitudes. Despite this difference between LGN and visual cortex it should be noted that both structures failed to show the predicted increases in ΔBOLD%. Thus, measured values in the LGN fall short at least 19% (relative) of the predictions when expressed in units of normoxic ΔBOLD%. Results from visual cortex deviate from the predictions by at least 40%, expressed in the same units. In addition, the observed effect in visual cortex was time dependent, another feature not explained by the modified DDM.

Reasons for these deviations may be found in potential violations of one or several assumptions of the modified DDM: Our derivation of the modified DDM assumed no change in relative stimulation induced increases of neuronal activity and metabolism under hyperoxia when compared to normoxia. It is known, however, that prolonged high doses of hyperbaric oxygen can produce seizures ([44] for a recent study see [99]), indicating adaptive changes in the excitability levels of cortical and subcortical networks under hyperoxia. A mechanism of seizure generation based on nNOS derived NO has recently been proposed by Demchenko and colleagues [26]. Changes in nNOS activity may be due to changes in intracellular calcium under hyperoxia as pointed out by Wang and colleagues [113]. This suggests the possibility that weaker effects of hyperoxia on neuronal circuitry exist even at normobaric conditions. This seemingly conflicts with evidence of unchanged somatosensory evoked potentials under hyperoxia [76]. However, even unchanged evoked potentials do not imply that the total metabolic response to a sensory stimulus is left unchanged under hyperoxia. The non-stimulus locked parts of the response (often termed *induced* responses) may contribute significantly to the increased energy consumption after stimulation and correlate well with the BOLD signal [78] and the very similar response measured with optical recording [94]. Therefore, hyperoxia dependent changes in the induced responses under hyperoxia will strongly alter

BOLD fMRI responses but escape a classical evoked potential analysis.

The second assumption in the derivation of the DDM that is probably not met under hyperoxia is that the gain (n) of neurovascular coupling remains constant when switching from normoxic to hyperoxic conditions. It is likely that this gain n changes as a function of direct chemical reactions between increased levels of superoxide radicals under hyperoxia or increased physically dissolved oxygen and substrates involved in neurovascular coupling. Reactions of this kind are known for SNOHb [104, 88], PGE2 [89] and NO [3]. Further molecules that both play a role in neurovascular coupling and directly interact with excess oxygen may exist. The available data on biological time constants of these reactions and compensatory processes only allow exclusion of certain substances like SNOHb, for which time constants of oxygenation effects are on the scale of fractions of a second [88], whereas the effects we observed here developed over several tens of minutes. We did not find any data on the time course of basal rCBF modulation under normobaric hyperoxia for more than 2 hours. Thus, the late recovery we observed could in principle be based on a further reduction of basal rCBF and be in accordance with the modified DDM. However, this is rather unlikely as rCBF was reported to rise and not to fall at later stages of hyperoxia, at least in the hyperbaric case [3].

While one or both of the above mentioned processes may have contributed to the failure of the modified deoxyhemoglobin dilution model, a potential explanation of our findings must, at the same time, explain the differences between LGN and visual cortex and the temporal evolution of ΔBOLD% in visual cortex. In the following two sections we will discuss the two potential mechanisms of hyperoxic influence that were identified above with respect to their ability to account for *all* of the observed effects.

Changes in the Gain of Neurovascular Coupling by Direct Oxygen to Modulator/Mediator Interaction

As outlined above, solid evidence exists for an involvement of NO in the mediation of the effects of hyperoxia on baseline blood flow. A study by Atochin and colleagues on hyperoxia in anaesthetised rats which covered exposure durations slightly over an hour [3] provided time resolved measurements of modulations of basal rCBF. Interestingly, in these experiments a biphasic modulation of basal rCBF and of NO availability was observed similar to the biphasic modulation of ΔBOLD% in our experiments. This suggests a possible mechanism for an interaction between hyperoxia and cerebral va-

soregulation with two competing pathways having different time constants (another possibility to explain the biphasic nature of the observed effect are vascular autoregulatory processes). Combining this finding of modulated available NO levels over time under hyperoxia with the observation that NO availability modulates hemodynamic response amplitudes [28] would account for our findings in visual cortex. This interpretation, however, does not directly explain why we did not find time dependent effects in the LGN. One possibility is that the changes in the LGN were smaller than in the cortex and hidden in fluctuations caused by other variables. This is supported by the fact that we found residual confound influences for the LGN in the pooled data from time course and retest experiments. It should be noted that the above mentioned study by Dirnagl and colleagues [28] used systemic or topical application of N^{ω}-nitro-L-arginine (L-NA) which blocks, both, neuronal Nitric Oxide Synthase (nNOS) and endothelial Nitric Oxide Synthase (eNOS). At the vessel wall the block of eNOS should lead to similar effects as the action of superoxide radicals (present under hyperoxia) that directly react with NO to form the non-vasoactive compound OONO. In their experiment they measured changes in stimulus induced rCBF responses only once after 60 minutes of NO synthase block. Unfortunately, they did not perform further time resolved measurements.

Changes in Cortical and Thalamic Excitability Levels

Considering the evidence of hyperoxia induced epileptic seizures [44, 99, 26] it seems plausible that even small doses of oxygen modulate excitability levels of neuronal networks. Increased neuronal activity due to enhanced excitability is likely to produce increased metabolic demand. This increased background metabolic demand will decrease, rather than increase, the *fractional* stimulus driven activity, as reflected by the parameter ϵ of the model. Ultimately, this would yield lower values of ΔBOLD%, as this is also a *fractional* measure. Furthermore, a study by Aghakhani and colleagues [2] demonstrated the possibility of negative BOLD responses (or, hence, a reduction of response amplitude if added to positive responses) due to epileptic spiking and reported less frequent detection of spiking related BOLD fMRI responses in the thalamus. This agrees with our observation that hyperoxia effects were prominent in cortex only. Finally, auto regulatory mechanisms may drive excitability thresholds back to their pre-hyperoxia values and this could account for the biphasic changes observed in the visual cortex. In order to further explain the differences between visual cortex and LGN

three mechanisms may be considered. First, cortical synapses may exhibit faster and stronger adaptivity under hyperoxia induced activity changes than thalamic synapses. This is suggested by the fact that changes in the network properties in a deafferentation paradigm lead to rapid reorganisation in visual cortex within a few hours [19] whereas changes in the LGN were only found after 30 days and later [37]. Second, differences may be due to recurrent excitation in the cortex and the lack of such coupling in the LGN. Changes in local excitability are bound to have stronger effects in networks with positive feedback, even though there are inhibitory mechanisms that counteract the build up of supracritical excitation [30]. These inhibitory mechanisms may in fact autoregulate excitatory activity after disturbances like the proposed excitability shifts under hyperoxia. Thalamic circuits by contrast are dominated by recurrent inhibitory connections with the corticothalamic projections constituting the only potential feedback loop [103]. Third, oxygenation effects on the levels of other neurotransmitters like dopamine [112, 1] or on GABA transmission [6] may play a role. If modulation of neuronal activity by these transmitters is different between cortex and the LGN (for a recent investigation on the role of dopamine in the LGN see [42]) the reason for differential effects of hyperoxia may be found here. A layer resolved investigation of the activity in the LGN, which would separate magno- and parvocellular contributions and their corresponding neurotransmitter profiles may shed light on this issue. Unfortunately neither the stimuli used in our study nor the spatial resolution of fMRI as used here can provide such a layer resolved analysis.

While this neuronal model has the potential to account for both, the dissociation of effects between cortex and the LGN and the biphasic time course of the cortical response modulations, more data are required to reach final conclusions: Data are still lacking on the effect of normobaric hyperoxia on neuronal excitability and sustained background activity. Recordings of unit activity and local field potentials under hyperoxia, in combination with fMRI or with optical imaging data [78, 94] could resolve this issue. Data are also missing on the molecular action of excess oxygen and of reactive oxygen species on synaptic transmission. Such effects are likely because superoxide radicals react with neuronally derived NO. Neuronally derived NO is thought to serve as second messenger in the adjustment of synaptic transmission [97].

1.4.7 Comparison with Existing Literature

While not confirming the predictions of our modified DDM, nor of the classical DDM, our results for ΔBOLD% are nevertheless compatible with measurements of Lindauer and colleagues, who recorded whisker stimulation-induced hyperoxygenation responses in rat somatosensory cortex [76] using microfiber optical spectroscopy (500-590 nm). Lindauer and colleagues observed a decrease in relative stimulus induced rCBF[2] responses under hyperoxia of 22 minutes. In contrast to their study and to our results, Kashikura and colleagues [66, 67] measured an increased BOLD fMRI response after application of hyperoxic conditions for up to 200 seconds. The difference to our results is likely to be explained by the fact that Kashikura and colleagues did not stabilize $EtCO_2$. Under hyperoxic conditions $EtCO_2$ and $paCO_2$ are usually altered in freely breathing subjects and animals due to hyperventilation [38, 102]. The reason for this is retention of CO_2 at central chemoreceptors due to reduced binding to haemoglobin under hyperoxia, the Haldane effect ([20]; for a review of CO_2 to O_2 interactions in binding to hemoglobin see: [61]) - triggering increased breathing rates. Thus, it is possible that the measurements made by Kashikura are dominated by vascular effects of arterial hypocapnia on BOLD fMRI response amplitudes as they were described by Cohen and colleagues [21].

Our data, however, are in contradiction to the results of a closely related study by Matsuura and colleagues [80]. This group investigated relative local cerebral blood flow responses to electrical stimulation of the hind paw in rats, both, under normoxic and hyperoxic conditions. They found increases in relative response amplitudes at 20-80 minutes after onset of hyperoxia, while confirming the typical slight vasoconstriction induced by hyperoxia. One potential explanation for the discrepancy observed between the results of Matsuura et al. on one hand and, on the other hand, those of Lindauer et al. and our results may lie in the cortical areas investigated. The eyes and the whiskers represent the principal senses for orientation in primates and rats, respectively. This might result in specific adaptivity mechanisms, metabolic demands and vascularisation in the cortices that process these particular sensory signals. In these cortices vascularisation and metabolic demand may therefore differ from those of somatosensory cortex responsible for processing of tactile or painful stimuli. Differences between the modulation of fMRI responses from V1 and somatosensory cortex by hyperoxia have been found previously also by Boakye and colleagues [9] under free

[2]The rCBF responses can be deduced from the hyperoxygenation response.

breathing conditions. As far as the late effects of prolonged hyperoxia are concerned we are not aware of studies that investigated stimulus induced hemodynamic responses beyond the time span of 80 minutes covered in the study of Matsuura and colleagues [80]. Our data thus fit the most closely related existing evidence [76] and extend the knowledge on hyperoxia induced modulation of functional hemodynamic responses to longer time spans than previously investigated. However, the observed temporary decrease is add odds with the classical theory of the BOLD effect *if we do not assume* a direct influence of excess oxygen or superoxide radicals either on neuronal function or the biochemical cascade of neurovascular coupling. Furthermore the observed recovery indicated that at least two competing mechanisms of interaction between oxygen and the BOLD fMRI signal are at work. Although the failure of the classical and the modified DDM may at first seem unsatisfying, our new findings may stimulate further research and ultimately foster our understanding of the BOLD effect, especially as the paradigm of excess oxygenation can be easily applied to a large variety of experimental preparations from slices to conscious subjects. Intracortical recordings under hyperoxia show the greatest promise to further our understanding of hyperoxia effects on the brain.

1.5 Conclusion

For the first time this study presents a time resolved analysis of the effects of prolonged normobaric hyperoxia on BOLD fMRI response amplitude. In visual cortex we demonstrated a biphasic behaviour consisting of a transient drop in average BOLD response amplitudes in the time bin from 0 to 180 minutes after onset of hyperoxia followed by a later recovery to baseline level. Our study supports previous observations made by Lindauer and colleagues [76]. Functional rCBV response measurements using MION furthermore suggest that these changes were induced by changes in neuronal activity or vasoreactivity under hyperoxia rather than by the changes in baseline blood oxygenation. We did not observe any effects in the LGN. Both observations contradict the deoxyhemoglobin dilution model [50], even though we incorporated the influence of non-zero plasma oxygen levels. The deoxyhemoglobin dilution model and, thus, Davis formalism for the calculation of CMRO2 [22] are, therefore, not applicable to the case of severe hyperoxia. Our results warrant cautious interpretation of studies on functional $CMRO_2$, rCBF and BOLD fMRI signal changes that employ hyperoxia, as the effects of hyperoxia are neither stable over time nor consistent over brain

regions.

Chapter 2

Independent MRI Signal Components in the Anaesthetised Macaque Monkey

2.1 Introduction

2.1.1 Motivation

The GLM analysis approach used in chapter 1 has three important drawbacks: First, we can only investigate phenomena about which sufficient previous knowledge exists to formulate a GLM model. Wrong assumptions that enter the GLM model will, in the best case, lead to its failure, detecting nothing in the data. In the worst case Type I error will lead to false positive results for a model that does not describe the true phenomena correctly.

Second, the GLM analysis will only explain a certain part of the variance present in the data, considering the unexplained variance as noise rather than as interesting phenomena that were just not included in the model.

Third, the GLM model used in fMRI is *massively univariate*, i.e. tests of the GLM are performed on a voxel by voxel basis. Information that is contained in the covariance structure of the data is lost this way. An example may elucidate this third point: Imagine an experiment with two experimental conditions. For condition 1 the *value of a voxel x is always high* when *the value of voxel y is low and vice versa*. Let the temporal mean of both voxels in this condition be a certain number $A1$. In condition 2

we find that the *value of voxel x is always high* when *the value of voxel y is also high and the value of voxel x is always low* when *the value of voxel y is also low*. Let the temporal mean of both voxels in this condition be a certain number $A2$. The GLM will only detect a difference between the two experimental conditions, if $A1 \neq A2$ which need not necessarily be the case. The fundamental, qualitative, difference of the two conditions, which consists of the differential coupling[1] of the two voxels x and y goes completely unnoticed. While a multivariate formulation of the GLM is possible, the inherent restriction that a model has to be specified a priori remains.

In fMRI datasets variance comes from a variety of sources: Variance is for example contributed from functional (neuronal) sources via neurovascular coupling, it stems from physiological influences (like pulsatile blood flow), signals that relate to the anaesthesia procedure or typical machine related artefacts (radio frequency power instabilities, magnetic field drifts due to temperature effects). More, but unexpected, sources may exist in a given dataset. Typically these sources of variance have a distinct spatial layout. Number, presence, location and strength of these sources are, however, not or not fully known a priori. One is therefore interested in *blindly* extracting groups of voxels that share a common behaviour (e.g. partially correlated or anticorrelated signal time courses) without being able to specify additional information. Algorithms from the field of blind source separation (BSS), especially Independent Component Analysis (ICA) are able to extract such unknown sources under some weak and very general assumptions, most importantly the assumption of statistical independence of the sources as will be explained below. The usefulness of ICA in fMRI data analysis has first been demonstrated by [84, 83]. Since then this method has been successfully applied to fMRI data to answer a variety of experimental questions [4, 13, 14, 15, 17, 18, 34, 35, 36, 39, 83, 84, 85, 86, 87, 90, 91, 92, 105, 106, 111, 121, 70].

2.1.2 Independent Component Analysis for BOLD fMRI Data

Independent Component Analysis (ICA) is a way of linearly transforming multivariate datasets (such as fMRI series of images or Electroencephalographic recordings) given as realisations of a random vector into a new random vector where the components of the new random vector are statistically independent, thus separating the *inherent modes* of the dataset. Another

[1] This differential coupling is contained in the covariance structure of the data, evaluated separately for the two conditions.

way to put this is that the ICA transformation minimises redundant or mutual information between the vector components. The concept of statistical independence will be explained in more detail below. ICA dates back to the early 1980s [48] and was initially designed to analyse neurophysiological data (for a review on the history of ICA see [64]). ICA gained more widespread attention when the two most popular algorithms to perform the ICA task that are in use today, FastICA and INFOMAX, were introduced in the mid 1990s (for the FastICA algorithm see [53] for the INFOMAX algorithm used here refer to [5]; for recent reviews on ICA and its application to neurophysiological and imaging data see [59] and [63]).

The concept of statistical independence and its implications are crucial in order to understand the algorithms and results of independent component analysis. Random vectors $\mathbf{x}$, $\mathbf{y}$, $\mathbf{z}$ are said to be *statistically independent*, if and only if their joint probability density function $p_{\mathbf{x},\mathbf{y},\mathbf{z}}(\mathbf{x},\mathbf{y},\mathbf{z})$ factorises into the product of their marginal probability densities $p_{\mathbf{x}}(\mathbf{x})$, $p_{\mathbf{y}}(\mathbf{y})$ and $p_{\mathbf{z}}(\mathbf{z})$:

$$p_{\mathbf{x},\mathbf{y},\mathbf{z}\ldots}(\mathbf{x},\mathbf{y},\mathbf{z},\ldots) = p_{\mathbf{x}}(\mathbf{x})p_{\mathbf{y}}(\mathbf{y})p_{\mathbf{z}}(\mathbf{z})\ldots \tag{2.1}$$

An important consequence of this is the fact that the *expectation E of the product of* arbitrary *functions* $g_i(i)$ of *statistically independent* random vectors i equals the *product of the separate expectations* $E\{g_i(i)\}$ as long as all the respective expectations exist:

$$E\left\{\prod g_{\mathbf{i}}(\mathbf{i})\right\} = \prod E\left\{g_{\mathbf{i}}(\mathbf{i})\right\} \tag{2.2}$$

The ICA task can be described as finding a linear transformation (matrix[2]) $\mathbf{U}$ that transforms a *set*[3] of *observed* random variables (i.e. a random vector) $\mathbf{X}$ in such a way that the obtained random variables $\mathbf{S}$ are as statistically independent as possible:

$$\mathbf{S} = \mathbf{UX} \tag{2.3}$$

Estimation Principles for ICA Algorithms used for performing ICA typically exploit the fact that the distribution of a linear combination of two *independent* random variables is more gaussian than either distribution of each of the independent variables[4], unless the linear combination would

[2]This matrix is typically referred to as the unmixing matrix

[3]Realisations of set of random variables x_i can be written in matrix notation in such a way that the rows of the matrix are the different variables and its columns are the observed realisations

[4]This is basically the central limit theorem. Of course, the necessary prerequisites for its applicability must be fulfilled.

only contain a nonzero coefficient for exactly one of the independent random variables. Thus, it is possible to obtain the independent random variables by finding linear combinations of the *observed* random variables (which themselves are, in turn, mixtures of assumed *independent* random variables) such that the distributions of these linear combinations are as non-gaussian as possible.

Different measures of non-gaussianity exist. A popular measure for non-gaussianity is the negentropy of a distribution of a random vector $\mathbf{y}$. For a random vector $\mathbf{y}$ its information theoretical entropy $H(\mathbf{y})$ is defined as:

$$H(\mathbf{y}) = -\int p_{\mathbf{y}}(\eta) \log p_{\mathbf{y}}(\eta) d\eta \tag{2.4}$$

with $p_{\mathbf{y}}(\eta)$ being the density of $\mathbf{y}$. Its negentropy $J(\mathbf{y})$ is then defined as:

$$J(\mathbf{y}) = H(\mathbf{y}_{gauss}) - H(\mathbf{y}) \tag{2.5}$$

with $\mathbf{y}_{gauss}$ being a random vector with gaussian distribution but identical correlation and covariance matrix as $\mathbf{y}$. In practice the distribution $p_{\mathbf{y}}(\eta)$ is not known and hard to estimate. Fortunately several computationally efficient approximations of the negentropy exist that allow its estimation from the data neither knowing $p_{\mathbf{y}}(\eta)$, nor estimating it directly. Moreover, we only need to estimate the negentropy of the 1-D distributions of the vector *components* to measure their non-gaussianity and maximise it. A popular approximation for the negentropy in the 1-D case is [54]:

$$J(y) = k_1(E\{G_1(y)\})^2 + k_2(E\{G_2(y)\} - E\{G_2(\nu)\})^2 \tag{2.6}$$

with $k_{1,2}$ being positive constants, ν being a gaussian variable with zero mean and $G_1(y)$ and $G_2(y)$ defined as:

$$G_1(y) = \frac{1}{\alpha_1} \log\cosh \alpha_1 y \tag{2.7}$$

$$G_2(y) = -\exp(\frac{-y^2}{2}) \tag{2.8}$$

where $1 \leq \alpha_1 \leq 2$ must hold. This approximation of negentropy in equation 2.6 is especially robust to outliers in the data. It is used for example in one of the most popular ICA algorithms - *FastICA* [54].

Another approach to solving the ICA task is to minimise the redundant or *mutual* information between between the components of the transformed random vector $\mathbf{S}$ in equation 2.3. The mutual information of the k scalar components s_i of $\mathbf{S}$ is defined as:

$$I(s_1, s_2, \ldots s_m) = \sum_{i=1}^{k} H(s_i) - H(\mathbf{s}) \tag{2.9}$$

with $H(\ldots)$ being the entropy defined as in equation 2.4. It can be shown that minimising mutual information between all s_i and maximising the sum of the non-gaussianities of the s_i is equivalent under some additional constraints [55]. It can also be shown that the minimisation of mutual information is approximated by the choosing the model such that it maximises the likelihood of the data (ICA via maximum likelihood estimation). This is important as the INFOMAX algorithm [5] that is widely used in ICA applications and also in this work is based on a principle that can be shown to be equivalent to maximum likelihood estimation of the ICA transformation [55, 56].

Data Layout in ICA of Spatio Temporal Imaging Data In the 4 dimensional datasets resulting from fMRI (3 spatial dimension, 1 temporal dimension) there are in principle two ways of defining the dimension(s) that host the random variables. The remaining dimension then provides multiple measured realisations of these random variables. For these random variables ICA then provides a linear transformation into a new set where the new random variables are statistically independent (implying, among other things, uncorrelatedness of the realisations of the new variables).

- One can treat the spatial dimensions as defining the set of random variables (each voxel resulting in a separate row of the matrix $\mathbf{X}$ filled with the values of the voxel time course) and the temporal dimension as providing samples of these random variables (i.e. each time point providing a column of $\mathbf{X}$ with one value per voxel. In this case one would obtain new random variables (weighted sums of voxels that can be thought of as spatially weighted maps) that have maximally independent time courses. This variant is referred to as *temporal* ICA (tICA) in the neuroscientific literature. This version of ICA is typically referred to as a solution to the so called *cocktail party problem* in introductory texts on ICA [57]. In a neuroscience context it is typically used on electroencephalographic data.

- One can treat the temporal dimension as defining the set random variables (each time point resulting in a row of the matrix $\mathbf{X}$) and the spatial dimension as providing samples of these random variables (i.e. each voxel providing a column of $\mathbf{X}$). After ICA one would obtain a set of new random variables (weighted sums of time points of the original data) that have statistically independent spatial maps. Hence, this variant of ICA is usually termed *spatial* ICA (sICA). Due

to the dimension of the dataset (many voxels - providing empirical realisations; few time points = variables to estimate) this is the default variant used in the analysis of fMRI data[5].

The data model underlying *spatial* ICA of imaging data where the data $\mathbf{X}$ of n voxels at m time points are generated by mixing k independent components (cp, Matrix $\mathbf{S}$) via the mixing Matrix $\mathbf{M}$ - containing the component time courses *cptc* can be written as:

$$\begin{array}{c} \\ t_1 \\ \vdots \\ t_m \end{array} \begin{array}{c} \begin{array}{ccc} \textit{voxel } 1 & \cdots & \textit{voxel } n \end{array} \\ \begin{pmatrix} x_{11} & \cdots & x_{1n} \\ \vdots & \ddots & \vdots \\ x_{m1} & \cdots & x_{mn} \end{pmatrix} \end{array} = \begin{array}{c} \begin{array}{ccc} \textit{cptc } 1 & \cdots & \textit{cptc } k \end{array} \\ \begin{pmatrix} M_{11} & \cdots & M_{1k} \\ \vdots & \ddots & \vdots \\ M_{m1} & \cdots & M_{mk} \end{pmatrix} \end{array} \begin{array}{c} \begin{array}{ccc} \textit{voxel } 1 & \cdots & \textit{voxel } n \end{array} \\ \begin{pmatrix} S_{11} & \cdots & S_{1n} \\ \vdots & \ddots & \vdots \\ S_{k1} & \cdots & S_{kn} \end{pmatrix} \end{array} \begin{array}{c} \\ cp_1 \\ \vdots \\ cp_k \end{array}$$

$$\mathbf{X} \qquad = \qquad \mathbf{M} \qquad\qquad \mathbf{S} \tag{2.10}$$

For the unmixing problem to be well defined we have to require $k<\mathtt{n}$, i.e. more time points have to be observed than the components that form part of the mixture $\mathbf{X}$. The ICA task was correspondingly stated in equation 2.3 with the same assignments of Matrices $\mathbf{X}$ and $\mathbf{S}$ and the unmixing matrix $\mathbf{U}$. The algorithm now estimates $\mathbf{U}$ in such a way that the independence of the components in $\mathbf{S}$ is maximised. If one is interested in the mixing matrix $\mathbf{M}$ this matrix can be obtained as the pseudo inverse of U.

Algorithmic Realisations of ICA Popular algorithmic implementations of this procedure are the *FastICA* fixed point algorithm [53] and the INFOMAX algorithm [5]. While algorithms may vary in their stability and ability to separate certain sorts of components (for an in depth treatment see [58]), some fundamental limitations and caveats exist[6]:

- The algorithm typically cannot decide how many independent components should be extracted.
- The algorithm can extract only one component that has a gaussian probability distribution.

[5]The use of temporal ICA on fMRI data necessitates the choice of a small subset of the voxels as an a priori region of interest

[6]There are efforts to alleviate or solve these problems. This is, however, still a field of active research and the above mentioned limitations definitely apply to the algorithms used in this work

- The algorithm typically yields a result, independent of whether the number of components was ill-chosen or more than one component with a gaussian probability distribution was present.
- The algorithm can, for real world data, only *approximate* statistical independence.
- The variance of the independent components cannot be estimated. It can easily be seen from equation 2.10 that any multiplication of a source with a constant factor can be cancelled by a division of the corresponding column of the mixing matrix by the same scalar. Therefore one can require either the time course or the component to be of unit variance as a convention.
- The sign of an independent component cannot be estimated unambiguously for the same reason stated above.

Subsequent tests of ICA results must be designed with these limitations in mind.

2.1.3 Group ICA in the Analysis of BOLD fMRI Acquired under Anaesthesia

Extending ICA to Multiple Datasets

Faced with the output of an independent component analysis (where components have no predefined order) it is desirable to distinguish somehow between meaningful results (components of interest, COIs) and the 'rest'. This problem gets more demanding if several sets of independent components from multiple decompositions (e.g. several subjects, multiple runs, different experimental conditions) have to be treated. The selection should of course be performed preferentially in a *model free* way, if possible, so as not to lose the advantages of a data driven approach like ICA. Basic research is interested in information on a population rather than on the particularities of the individual case. For this setting a possible model free selection strategy is to select those components that can be obtained repeatedly over subjects. As components will not be exactly identical some measure of similarity together with a clustering algorithm have to be used. An algorithm performing this task for fMRI datasets called 'self organising group ICA' (sogICA) has recently been published by Esposito [35] and is used here to select groups of independent components from the ICA decompositions of the single runs of this study.

A Novel Approach

Group level ICA, using clustering of independent components derived from single datasets (runs) alleviates the problem of judging which components in an ICA decomposition are meaningful - and repeatedly present over subjects [49]. It does not help however with the interpretation of the obtained separate component clusters. This problem has forced researchers to sort components (or component clusters) according to their correlation with an existing paradigm (basically a return to a model driven approach), to classify them based on mere anatomical constraints [70, 13] or to select them according to some expected features that guaranteed interpretability (like the selection of components that have known eye blink related topographies or dipolar topographies that is successfully used in the analysis of the electroencephalogram [23]).

Here we propose to test clusters of unknown origin for a sensitivity of their member components with respect to a set of independent physiological variables. As such a test should be as model free as possible to preserve the potential richness of ICA results, we only assume a monotonic dependency of individual map voxel values on the respective variable[7].

Calhoun and colleagues have proposed a seemingly similar approach [13] to test (via calculating z-scores and thus consistency) grouped independent components of several subjects. They, however used manual selection of components based on identifiable, *a priori* known anatomical structures and do not test for effects of independent variables within the component groups. The output of their method is roughly equivalent to the results of the first step in our analysis, the grouping via self organised clustering (resulting in z-score maps as well).

The ultimate goal of the new method proposed here is to aid the *interpretation* of component clusters. To this aim we can derive an *initial* hypothesis using the anatomical location of the peaks (most informative parts of the component distributions) in the cluster mean map, which are derived solely based on the inherent similarity of the components and no a priori knowledge. Time courses (columns of the mixing matrix) of individual member components can then lend support to the initial hypothesis or falsify it. Then difference maps are derived by sorting the member components of a cluster into two groups - above or below the median of an independent

[7]Note, however, that even this definition of a dependency excludes certain more complicated effects from being seen by the analysis. An example for this would be the influence of the variable *time elapsed since switching to hyperoxia* on BOLD fMRI responses that shows a non monotonous, biphasic behaviour

variable - and subsequently testing for significant differences between the two groups on a voxel by voxel basis. These difference maps can then be used to see if an influence of a certain variable exists. If so, we can evaluate whether an influence of this variable is consistent with the preliminary hypothesis proposed for the cluster under investigation. If this is not the case one can return to the first step and try to design an alternative hypothesis about the cluster that can be reconciled with anatomical location, time courses *and difference maps*. We thus rest the identification of a cluster on a broader base than on anatomical features or time courses alone. In this way it is often possible to derive a clear cut hypothesis about the origin of a component cluster that would otherwise not be interpretable. Our method thus helps to choose the few component clusters that warrant further investigation among the many resulting from multiple ICA decompositions with subsequent clustering. Moreover, for the case where a component is unequivocally identified by its map and time course alone, testing for the influence of independent variables can yield new insights into the physiologic mechanisms underlying that particular component.

2.2 Methods

2.2.1 Overview of Analysis Workflow

Figure 2.1 presents an outline of the analysis used in this chapter. The methods are described in further detail below, while a coherent presentation of the workflow is the aim of this section. 95 datasets (runs) from two monkeys (B, K) were taken from the previous experiment. After standard preprocessing we performed an ICA decomposition using the INFOMAX algorithm on each separate dataset (run), yielding 30 spatially independent components (spatial maps of z-transformed intensity values) per run. Thus a total number of 2850 components were obtained. Next we used self organising clustering as described in [49, 35] to cluster the independent components into 30 clusters based on their spatial similarity. As an additional constraint we required that each run could contribute maximally one component to each cluster. For these clusters we formulated the hypothesis that certain anaesthesia or physiological variables should change the data in such a way that differences in some (but not necessarily all[8]) of the obtained independent component maps should occur. To operationalise this we tested for differences in the

[8]Machine artefacts like shim drifts should not be influenced by anaesthesia or physiological parameters

member maps of a cluster that depended in a monotonic fashion on changes in the independent variables (anaesthesia related or physiological). To this aim we constructed for each independent variable a list that contained the runs sorted by the value of this variable in the respective run. For each pairing of an independent variable and a cluster we then sorted the independent components of that cluster into two subgroups, depending on whether the value of the independent variable in their *run of origin* was above or below the median. An example may help understand this sorting better [9]: cluster 17 might contain independent components 123 and 2538, coming from run 5 and run 85, respectively. These two runs may in turn be associated to an average heart rate of 110/min (run 5) and 140/min (run 85). Assume that 110/min is below the median of all observed values for the variable heart rate and 140/min is above this median. The component 123 would than be sorted into the subgroup 'lower' of cluster 17 while component 2538 would be assigned to the subgroup 'higher'. To avoid systematic differences that may be based on a systematic difference of the values of an individual variable between the two animals (monkey B, K) we balanced the groups for this factor. In order to test for statistical differences between the subgroups we used a voxel wise t-test with a false discovery threshold [41] of $q<0.05$ for significance.

2.2.2 fMRI Data Preprocessing

Slice based functional MRI datasets were preprocessed using intra session alignment between subsequent runs and using 3D sub millimetre motion correction. While motion correction is in general not considered optimal for subsequent ICA, it was considered necessary here as drifts of the magnetic field moved the image centre more than 4 voxels in some runs. After spatially normalising[10] and coregistering the slice based fMRI data to the brain of a reference monkey (B) 4–D volume time course datasets were created. Data were then smoothed with a gaussian kernel of 2mm full width at half maximum. Typically smoothing with a broader kernel is applied to

[9] It may also help to think of the ICs in a cluster being sorted by the values of the independent variables. This formulation is only sloppy insofar as runs, not components, are originally associated with values of the independent variables.

[10] Spatial normalisation was achieved by using a pseudo talairach normalisation - independently transforming the twelve compartments of the standard talairach space in such a way the the ratios of talairach coordinates of the defining points in talairach space (anterior commissure, posterior commissure, frontal pole, posterior pole, superior pole, inferior pole, left pole, right pole) to those of standard talairach space were identical for all datasets of all monkeys after transformation.

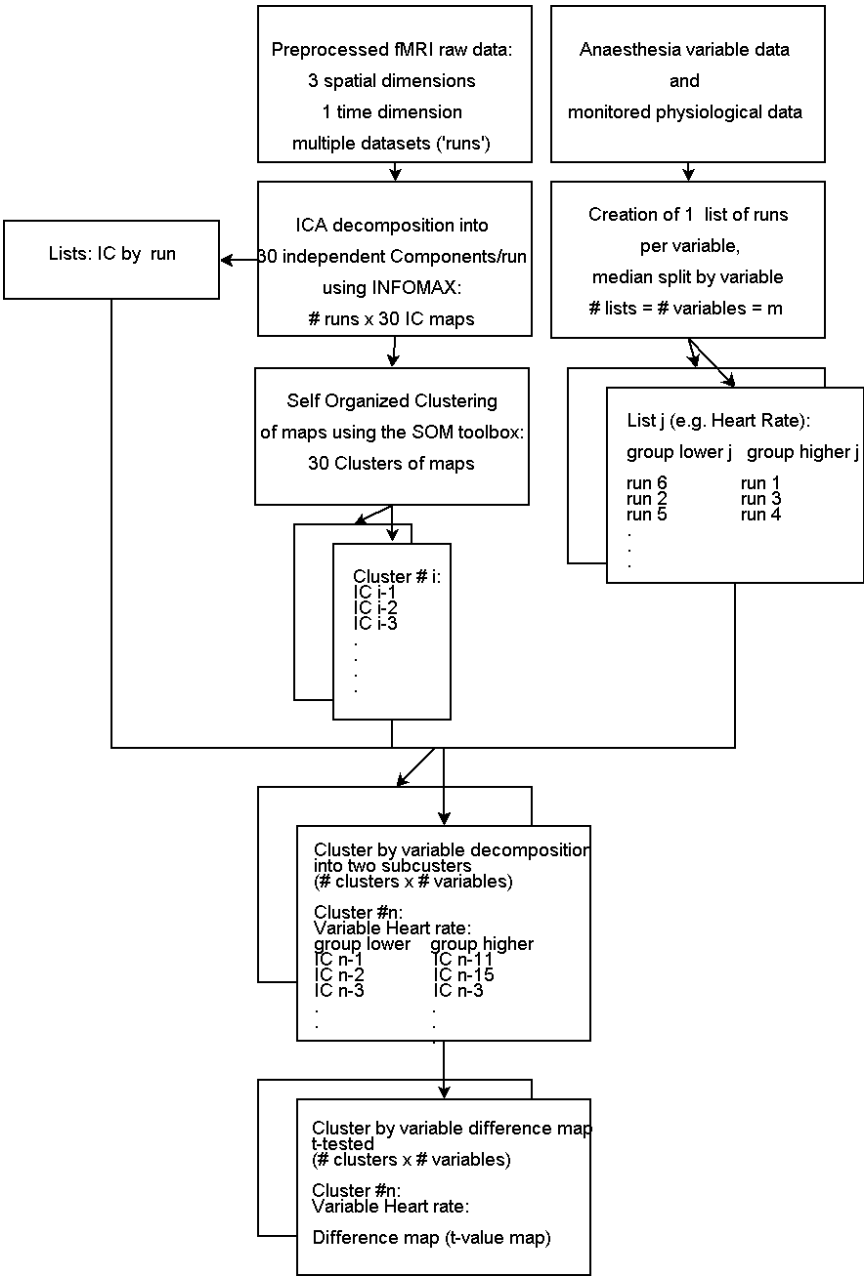

Figure 2.1: *Testing for significant influences of anaesthesia related variables on ICA decompositions: The central step is where Cluster List, IC-by-run list and run lists sorted by independent variables converge. An IC from a cluster is taken, its corresponding run of origin is looked up. For this run it is evaluated whether the value of the independent variable is above or below the median. Depending on this decision the IC is sorted into the* lower *or* higher *cluster subgroup. the two subgroups are then compared using a t-test.*

fMRI datasets before ICA and subsequent clustering to improve the match of independent components before clustering. We chose to use a smaller kernel because of the small size of anatomical structures in a monkey brain[11]. Therefore, higher values for the dissimilarity of the component maps in a cluster are expected compared to those reported in the literature [35].

2.2.3 ICA Algorithm and Software

We first reduced the dimensionality of the data to 30 temporal dimensions using PCA. For each subject we then estimated 30 independent components using the INFOMAX algorithm of Bell and Sejnowski [5] for the ICA decomposition. This algorithm was part of a MATLAB® software package for self organised group ICA and visualisation of spatial component clusters. The MATLAB software containing the algorithm was provided by F. Esposito [35] and V. Van de Ven [111] kindly provided wrapper functions to these algorithms. Details on the used algorithms can be found in [35].

ICA algorithms cannot determine how many independent components are hidden in a given dataset. Choosing too few independent components for extraction will result in components that are still mixtures and not as independent as they would have been with the optimum choice. Forcing the algorithm to yield more independent components than are actually contained in the data will lead to independent components that are split which prevents the data from being described optimally. The choice of 30 components as a target for component extraction was based on the following heuristics: We knew that a certain component should reflect the BOLD fMRI response to visual stimulation of the primary visual cortices. An upper limit of the number of independent components is found by increasing this number up to a point where the component that reflects this response is actually split into two or more components that do not show a reasonable time course for functional activation any more. Note that this limit may vary from run to run. This approach is also not applicable when this particular component is missing altogether as it was the case for some runs recorded early after injection of Methohexital (see figure 1.3). A consistent number of components after the decomposition was necessary for the subsequent clustering step, however. We therefore chose a value of 30 which was small enough to avoid splitting of the functional BOLD fMRI response component in any of those runs where we observed a stimulus driven component, while the dimension reduction to 30 dimensions using PCA kept more than 99% of the variance

[11] The grey matter thickness, for example, is below 2 mm in our datasets

in the data.

2.2.4 Self-Organising Group ICA: sogICA

We computed the matrix (**SM**) of absolute values of the spatial correlation coefficients of the component maps as a similarity measure[12]. To obtain a distance for clustering values of this matrix were transformed into a dissimilarity measure **DM** [49, 35]:

$$\mathbf{DM}(i,j) = \sqrt{1 - \mathbf{SM}(i,j)} \quad \forall i,j = 1 \ldots \textit{overall number of components} \tag{2.11}$$

This distance measure was used as an input into the self organised clustering algorithm as it was described in [35]. We used the constraint that each run contributed exactly 1 component to each cluster.

2.2.5 Choice of Independent Variables for Analysis

Our experimental data provided a rich set of independent variables that contained information about anaesthesia settings, feedback controlled physiological variables and recorded physiological covariates. Due to the size of the resulting Cluster–by–Independent Variable space[13] we had to limit our analysis to the most important ones to satisfy our current constraints on computing power. Here we chose those variables that had a significant influence on the stimulus driven functional activation patterns in the pilot experiment (refer to table 1.2). Of these variables we omitted the interaction term of Isofluorane dose and Fentanyl, as it did seem to be confounded with the linear Isofluorane effect (see note in the caption of table 1.2). It is very important to note at this point that variables that did not influence the *stimulus driven* fMRI BOLD signal amplitude could very well make a difference with regard to *non stimulus driven* signal patterns. As an example it is conceivable that the dose of the paralytic (mivacurium chloride) does not change functional activation per se but has a profound effect on the amount of eye movement related artefacts in the signal. Or, else, large veins that often show up as a spatial map in independent component analysis of fMRI data could be influenced by the heart rate although this variable did not show a significant influence on the fMRI BOLD response signal amplitude.

[12] **SM** stands for spatial similarity matrix and is *not* the product of matrices **S** and **M** mentioned previously

[13] The initial number of obtained Difference Maps is equal to the number of Component clusters (30) times the number of independent variables (10) that were used for median splitting the clustered components into subgroups below and above the respective median.

We therefore chose to include the *dose of mivacurium chloride*, *heart rate* and also the *infusion rate of saline solution* in our list of independent variables. In order to confirm also the missing *time independent* influence of the inspiratory oxygen fraction we also included FiO_2 as an independent variable.

2.2.6 Construction of Cluster Subgroups

For each cluster X we determined the runs of origin of its clustered independent component maps. For each of the runs of origin we then determined whether the independent variable Y had a value above or below the median of Y for all runs of origin that contributed components to the cluster X. We could thus sort the independent components in cluster X into two groups:

1. independent components from runs where Y was below the median and

2. independent components from runs where Y was above the median.

For n clusters and m independent variables we thus obtained $n \cdot m$ cluster subgroup pairs for statistical comparison.

2.2.7 Statistical Tests

As the sign of an independent component is assigned arbitrarily during ICA analysis we first took the absolute of the z-transformed independent component maps. This transformation keeps the information on the informative (extreme) ends of the signal distribution of a map intact. The transformed maps can vary in their deviation from zero, depending on the influence of the independent variable Y on the results of the preceding ICA decomposition. Our null hypothesis for the subsequent test between the two subgroups within a cluster X with respect to the independent variable Y can be stated as follows:

> The absolute z-value of a voxel in a spatially independent component map is *not different* between the group of maps in cluster X that come from runs where Y had a value *below* the median (of Y over *all* cluster members) and the group of maps in cluster X that come from runs where Y had a value *above* the median.

This hypothesis was tested on a voxel wise basis using a two tailed t-test. The significance threshold was based on the false discovery rate (FDR,

threshold denoted as q) as described in [41]. We assigned significance to t-values corresponding to q < 0.05. The use of FDR based statistics is mandatory in imaging data due to the large number of t-tests performed, that leads to a severe multiple comparisons problem [14].

2.2.8 Choosing Results for Presentation

Our aim was to identify variables that influenced the characteristic parts of the clustered IC maps. By characteristic parts we mean those voxels that drove the identification of the ICs in the first place during the use of the INFOMAX algorithm and at the same time were consistent over IC maps from different runs leading to their clustering. These parts are identifiable by high values of the mean of the absolute of the component maps collected within a cluster (further on called cluster map)[15]. To identify those variables that influenced the characteristic parts of a cluster map we computed for each cluster-independent variable pair the cross correlation coefficient of the cluster map and the absolute of the binary map of voxels that displayed a significant difference. Here we present all difference maps where the absolute of this cross correlation coefficient *exceeded 0.1.*

2.3 Results

2.3.1 Spatial Clusters and Cluster-by-Variable Difference Maps

Here we present the results of spatially clustering the independent component resulting from the ICA decomposition of individual runs. Clusters were constrained to contain one and just one component contributed from each run, thus resulting in 95 cluster members for each of the 30 clusters. Cluster similarity distances are presented in figure 2.2. A visualisation of the clusters in a 2-D cluster distance space using curvilinear component analysis [49] is presented in figures 2.3 and 2.4. Cluster 1-6 had a relatively compact and well separated structure with few outliers, the worst clustering being present in cluster 6 with 16 outliers (17%) (figure 2.3; note that each cluster has 95 member components, most of which are invisible due to overplotting). Clusters 7-12 had a different structure consisting of a more or

[14]The alternative Bonferroni correction typically proves to be overly conservative for these kind of data, as one has to deal with $10^5 - 10^6$ voxels and, thus, t-tests.

[15]One has to take the individual component maps to the absolute here as the sign of a voxel in an IC map is arbitrary. It is only the sign of the entries in the (un-)mixing matrix together with the sign of the entries in the components that has a meaning, i.e. the product of mixing matrix and component matrix has to restore the original data faithfully.

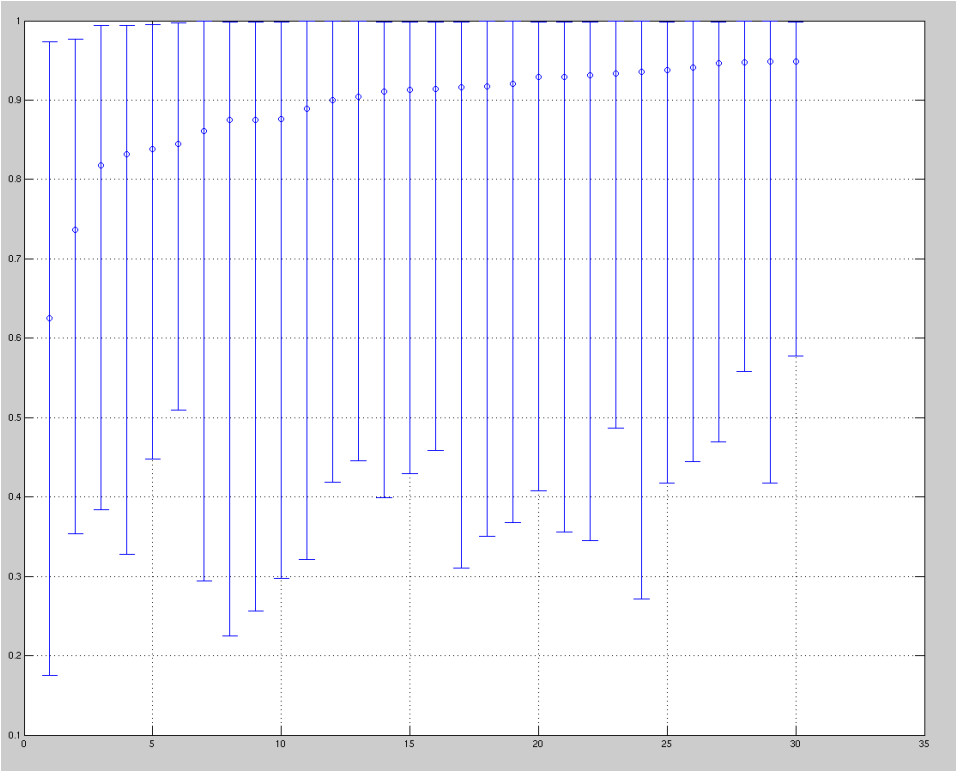

Figure 2.2: *Results of clustering. x-axis: cluster number. y-axis: Dissimilarity measure (min, mean, max) within cluster. Clusters are sorted by their mean within cluster dissimilarity.*

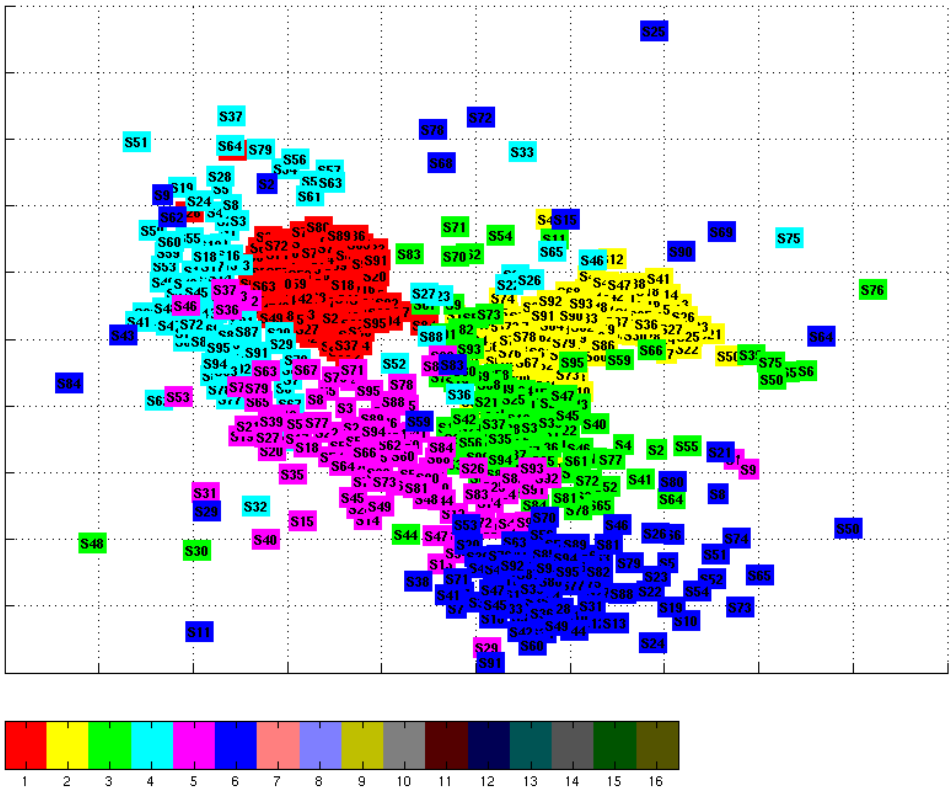

Figure 2.3: *Results of clustering. Visualisation of clusters 1 to 6 using CCA. Colour bar indicates cluster number as used in the text. S + Number refers to the sequence of inclusion of the components into a specific cluster. Note that not all members (95) of a cluster are visible due to severe over-plotting.*

less dense cluster core and relatively many outliers (figure 2.4). Intra cluster dissimilarities (figure 2.2) were higher than reported in the literature [35]. This was expected, however, as no spatial smoothing had been applied to our data. Cluster map results are displayed in radiologic convention[16]as z-value (taken per individual map) IC maps averaged over the 95 cluster members in figures 2.5 to 2.38. Locations of maximal map values are indicated by the hairlines in the figures and given in the figure legend as well as in table 2.1. Coordinates are defined relative to the midline sagittal plane, a plane that was perpendicular to this sagittal plane and contained the anterior commissure (AC) and the posterior commissure (PC), and a third coronal plane

[16]The anatomical left side is the right side of the printed figure. This is the accepted default for fMRI data presentation.

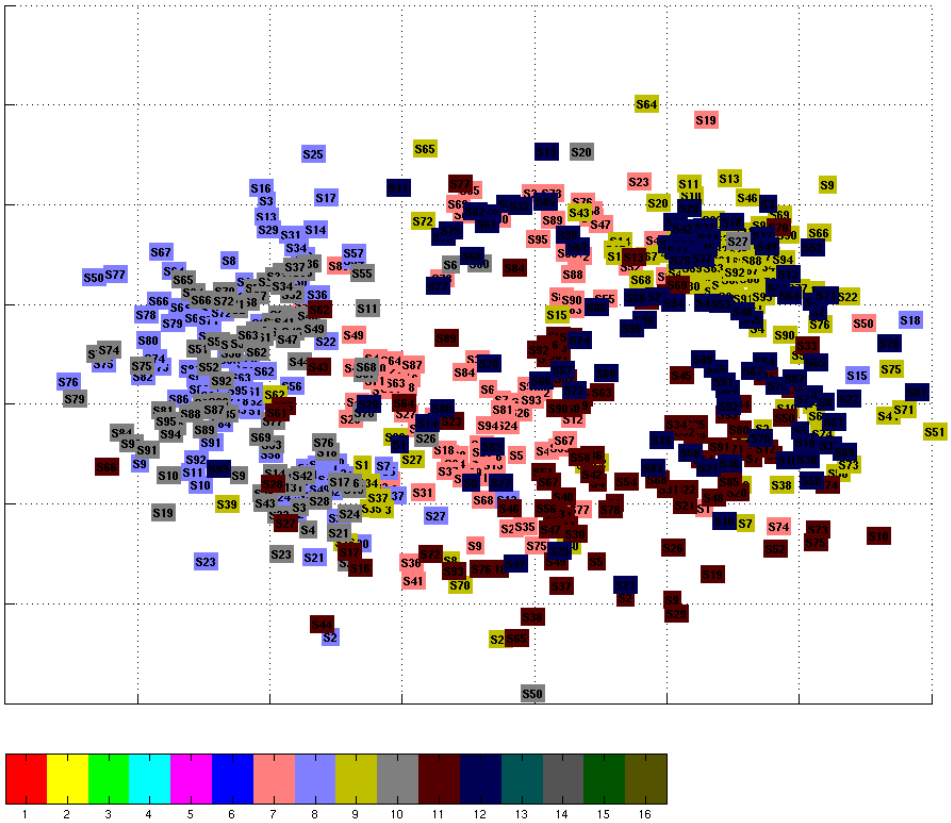

Figure 2.4: *Results of clustering. Visualisation of clusters 7 to 12 using CCA. Colorbar indicates cluster number as used in the text. S + Number refers to the sequence of inclusion of the components into a specific cluster. Note that not all members (95) of a cluster are visible due to severe over-plotting.*

through AC[17]. This coordinate system is compatible with the one used by Martin and Bowden in their stereotaxic atlas of the macaque monkey brain [79]. As sign is arbitrary after ICA decomposition we opted to choose the sign for each independent component in such a way that spatial correlation was maximally positive before averaging the cluster member (component) maps. For the resulting cluster mean maps we chose the sign such that their maximum was positive. For each cluster we also show a typical IC member

[17]The midline point of the anterior commissure (AC) is defined as (0,0,0). RL - Right to left axis; negative values indicate a position right of the midline. AP - Anterior to Posterior axis; negative values indicate a position posterior of AC. DV - Dorsal to Ventral axis; negative values indicate a position ventral of AC. Values in brackets are added for easier reading: R = right of midline; L = left of midline; A = anterior of AC; P = posterior of AC; D = dorsal of AC; V = ventral of AC.

Cluster	Coordinates[18] (RL, AP, DV)	Anatomical Correlate
1	-0.7 -15.3 -15.3	brain stem and skull base
2	0.0 -21.3 6.0	occipital sagittal sinus
3	17.3 21.3 -9.3	left eye, vitreous humour
4	-8.0 -15.3 -7.3	vascular structure next to collateral sulcus
5	0.0 -10.7 24.0	central sagittal sinus
6	12.0 21.3 -2.0	left eye, vitreous humour
7	0.0 -14.7 2.0	lateral ventricles
8	-10.0 -8.0 -8.7	dorsal nucleus of the lateral geniculate body or nearby vascular structure
9	-12.0 11.3 -6.0	superior oblique muscles of both eyes
10	-27.3 -0.7 0.7	lateral sulcus, anterior subcentral sulcus, superior ramus of the arcuate sulcus
11	-20.0 21.3 -13.3	right eye, vitreous humour
12	-24.0 -26.7 3.3	bilateral early visual cortex (areas V1-V3)

Table 2.1: *Locations of maximum z-values in cluster maps and corresponding anatomical structures at these locations.*

map taken from an individual run (Monkey K; date: February 9th 2004; run Nr.: 7, Dataset ID: 40) that was present in most cluster cores[18]. For this single run map we also present the associated time course of the component (i.e. the respective column of the estimated mixing matrix). Note that it does not make sense to present averaged time courses of the cluster members as this would imply locking of the time course to some event, which is necessarily present for all independent component time courses. We limit ourselves to the presentation of those clusters that later were significantly modulated by the influence of at least one independent variable (clusters 1-5, 10, 12; see subsection 2.2.7) or had a lower mean intra cluster dissimilarity measure than these (clusters 6-9, 11; refer to figure 2.2). Furthermore we present the difference maps for all the identified (see methods) influential variables for each cluster. These maps are overlaid on a T1 weighted

[18]For clusters where this was not a member of the cluster core, we present an alternative run additionally.

Independent Variable	Range (Units)
Dose of Fentanyl	2.5 - 3.5 ($\frac{\mu}{kg \cdot h}$)
Dose of Mivacurium Chloride	6.1 - 6.9 ($\frac{mg}{kg \cdot h}$)
Saline Infusion Rate	6.2 - 17.4 ($\frac{ml}{kg \cdot h}$)
Heart Rate	84 - 157 ($\frac{1}{min}$)
Isofluorane level (end tidal)	0.23 - 0.31 (% vol.)
Systolic Blood Pressure (non invasive measurement)	89 - 173 (mmHg)
Body Temperature (rectal)	37.58 - 38.89 ($°C$)
Time elapsed since Injection of Methohexital	98 - 709 (min.)
FiO_2	22 - 94 (% vol.)

Table 2.2: *List of independent variables used in the search for significant influences on the cluster maps.*

anatomical [19] image averaged over the monkeys analysed. Significant voxels (FDR q < 0.05) are presented in pseudo colours. The blue to green colour scale indicates that the subgroup of component maps with lower values in the independent variable also had lower average *absolute* z-values in the respective voxel. Put in another way, at the blue to green voxels the subgroup of component maps with the higher values of the independent variables had more extreme z-values.

Figure 2.40 may serve as an example: The investigated cluster 12 most likely represents the functional activation by the visual stimulus. In the GLM analysis of part 1 the amplitude of this activation rose with increasing temperature. As the component map was normalised during the ICA decomposition this amplitude increase should result in higher z-values in the corresponding independent component maps. Hence, the group with the *higher* average temperature should have, on average, more extreme absolute z-values, colour coded in the blue to green colours. This is exactly the finding depicted in figure 2.40. Correspondingly the red to yellow colour scale denotes voxels were the group of maps with *lower* values in the independent variable actually had higher absolute z-values at the corresponding voxels.

Cluster 1

Cluster Description The main focus of this cluster map (figure 2.5) was a large convex region on the brain stem at its entry point at the skull

[19] MR acquisition sequence: MPRAGE, see chapter 1, methods.

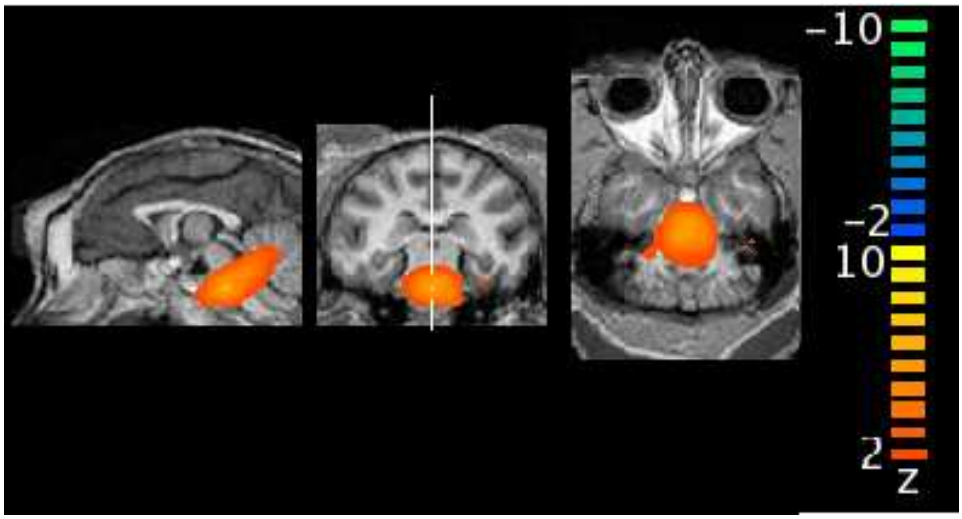

Figure 2.5: *Cluster 1 - thresholded z-value map at $|z| > 2$. Hairline indicates map maximum. Coordinates relative to anterior commissure and midline: RL: -0.7mm (R), AP: -15.3mm (P), DV: 15.3mm (V).*

base. This region was on the one hand in the bottommost slices of the slice stack of our EPI sequences and, on the other hand in an anatomical region where the paramagnetism of the large bone structures of the skull base renders the magnetic field rather inhomogeneous - leading to weak signal or signal dropout. As our scanning parameters led to excessive heating of the shim iron of the scanner we typically observed a B_0 drift that translated to a strong image shift from anterior to posterior. The size of this drift was typically on the order of 4 image pixels (4-6mm) While both, scanner software (in k-space) and our analysis software (BrainVoyagerQX) tried to compensate for these effects, they can, in general, not be corrected fully, due to their nonlinear nature. ICA is known to detect, both, remaining image motion effects and those of attempted motion correction [36]. We therefore assumed this independent component cluster to represent shim drift effects in the regions of greatest susceptibility effects and image intensity gradients. As heating of the shim irons built up linearly over the duration of a scan we expected the timecourse of this ICA component to be linear. This can indeed be seen in the timecourses of the single run IC components that form the cluster. An example of this behaviour is given in figure 2.6.

Difference Maps Cluster1 was significantly influenced by the independent variables *Fentanyl dose* and *saline infusion rate* as can be seen in fig-

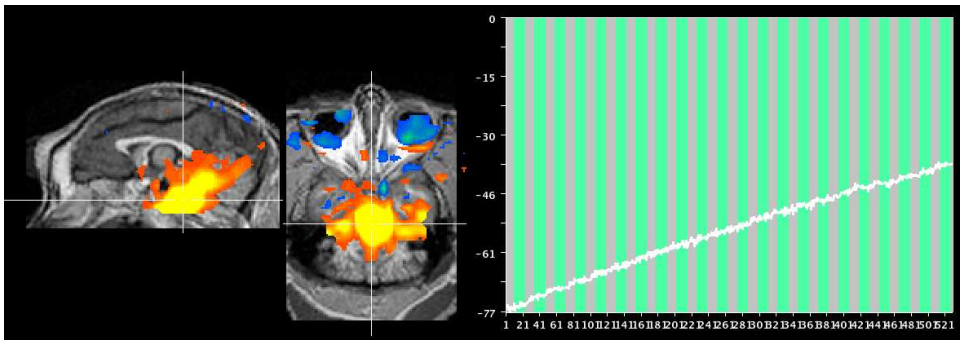

Figure 2.6: *Cluster 1 member component from single run (ID 040) - thresholded z-value map. Hairline indicates the position of the cluster map maximum. Coordinates relative to anterior commissure and midline: RL: -0.7mm (R), AP: -15.3mm (P), DV: 15.3mm (V). Component time course is displayed on the right side. Green shading indicates stimulus ON intervals.*

ures 2.7 and 2.8. For the case of Fentanyl the observed influence was rather unexpected. The structure of the difference map was, in addition, quite different from the structure of the cluster map itself. It is therefore probably that we observed a merely coincidental effect of Fentanyl here. Typically Fentanyl doses were increased when anaesthesia was less stable. This also led to increased breaks between subsequent runs, possibly enhancing the thermal effects that led to shim drifts.

For the case of Saline the observation of significant effects was surprising as well. One possible cause could be the overlap of the regions most sensitive to shim drifts with those that contain large vessel structures at the skull base. Signal from these large vessel structures will of course be influenced by the blood volume fraction in a voxel which, in turn, depends on the sufficient supply of fluids during anaesthesia.

Cluster 2

Cluster Description The main feature of this cluster map perfectly overlapped with the sagittal sinus. We therefore propose that this cluster represented the vascular signal contributions from the large draining veins in the occipital parts of the brain and the sagittal sinus. Data from single run member components were in agreement with this interpretation (see figure 2.10): they, too, had their most prominent map features around the sagittal sinus. Moreover, the oxygenation level of the venous blood in the large occipital draining veins and the sagittal sinus should reflect the periodic

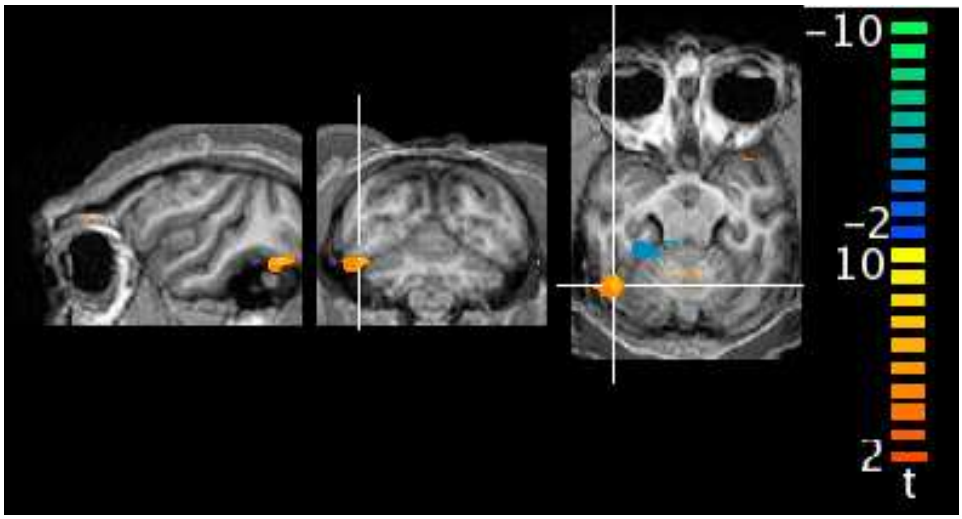

Figure 2.7: *Cluster 1 - sites of maximum influence of Fentanyl dose.*

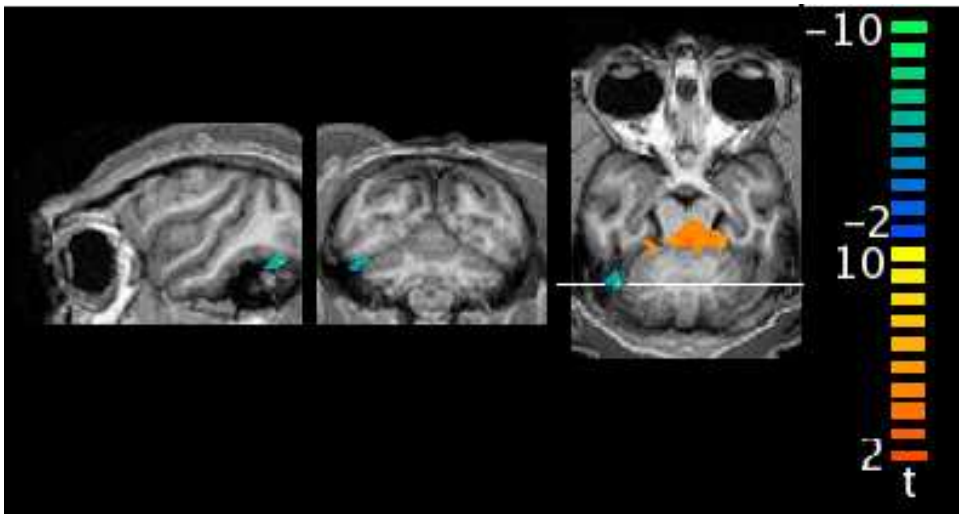

Figure 2.8: *Cluster 1 - sites of maximum influence of saline infusion rate*

activation of large parts of visual cortex by our visual stimulation (refer to to chapter 1, methods section). This was indeed the case as can be seen in the time course representation in figure 2.10. The component time course showed a strong periodic modulation with the stimulation frequency. The sign of the modulation (positive in stimulated periods) multiplied with the sign of the map maximum (positive) yielded the correct sign for the BOLD fMRI effect, as expected. The activation (elevated signal levels) seemed, however, to lag behind the stimulation more than expected for the typical BOLD fMRI response in activated parenchyma. This, too, was to be expected for signal changes in large downstream vessels far away from the locus of neuronal activation and has been described previously [77].

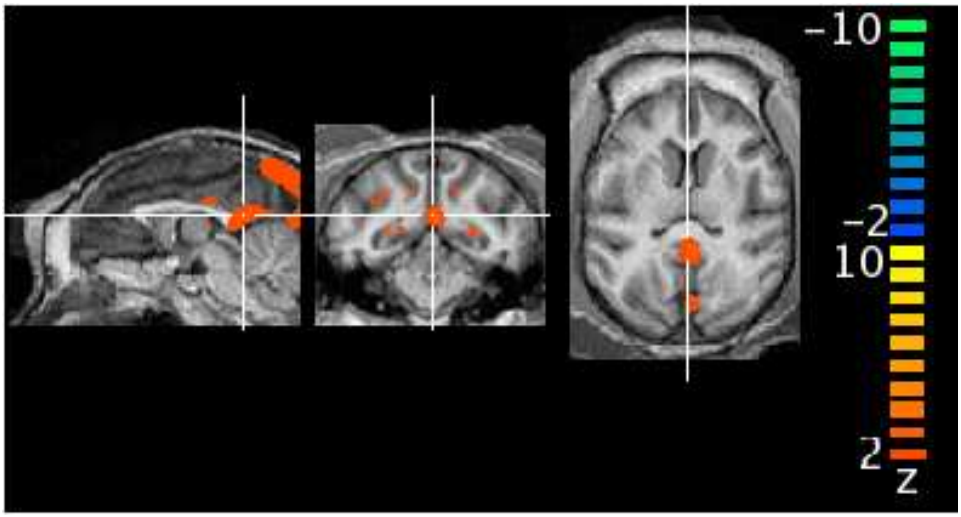

Figure 2.9: *Cluster 2 - thresholded z-value map at $|z| > 2$. Hairline indicates the position of the cluster map maximum. Coordinates relative to anterior commissure and midline: RL: 0.0mm, AP: -21.3mm (P), DV: 6.0mm (D).*

Difference Maps This cluster was significantly influenced by the independent variables *time since injection of Methohexital*, *heart rate* and *Isofluorane level*.

For the case of *time since injection of Methohexital* the maximum of the difference map overlapped with the main cluster map feature, the sagittal sinus. We observed a negative value at the maximum of the difference map. According to the conventions for the display of difference maps laid out above (section 2.3.1) a negative value is equivalent with larger z-values of the cluster subgroup that had larger values of the independent variable.

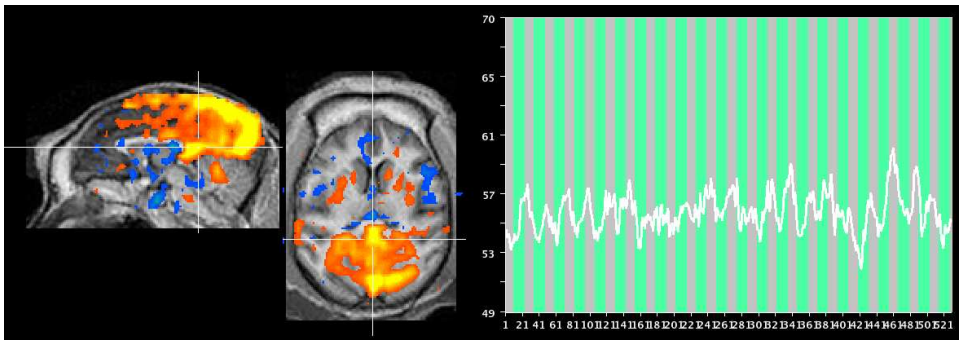

Figure 2.10: *Cluster 2 member component from single run (ID 040) - thresholded z-value map. Hairline indicates the position of the cluster map maximum. Coordinates relative to anterior commissure and midline: RL: 0.0mm, AP: -21.3mm (P), DV: 6.0mm (D). Component time course is displayed on the right side. Green shading indicates stimulus ON intervals. Note the periodic signal changes that follow the time course of the stimulation.*

Here, this meant, independent components of the cluster where more time had elapsed since the injection of Methohexital had larger amplitudes in the maps. This was consistent with our previous observation that the strength of the BOLD fMRI responses increased with time after the injection of the barbiturate. It was a new finding, however, compared to the GLM analysis in chapter 1, that this influence can also be seen and followed in the large draining veins almost down to the level of their exit from the skull (confer figure 2.9).

The spatial pattern of the main influence of the independent variable *heart rate* was more speckled, very symmetric and often located in the sulci and close to the liquor spaces (see figure 2.12). These features indicated a vascular locus of the influenced parts of the cluster map as well. The sign of the difference map in these regions was positive, indicating that the cluster members with lower heart rate showed higher values in these regions. Lower heart rates were typically observed towards the end of our experiments, due to the accumulation of active metabolites of Fentanyl [101] and their tachycardic effects. Why this would change the signal amplitude in the map regions described above is, however, unclear at present.

Figure 2.13 displays the difference map for the independent variable *Isofluorane level*. This variable influenced the cluster map in a very similar way to the influence of *time since injection of Methohexital* and complementary to the influence of *heart rate*. The sign (negative) of the main parts

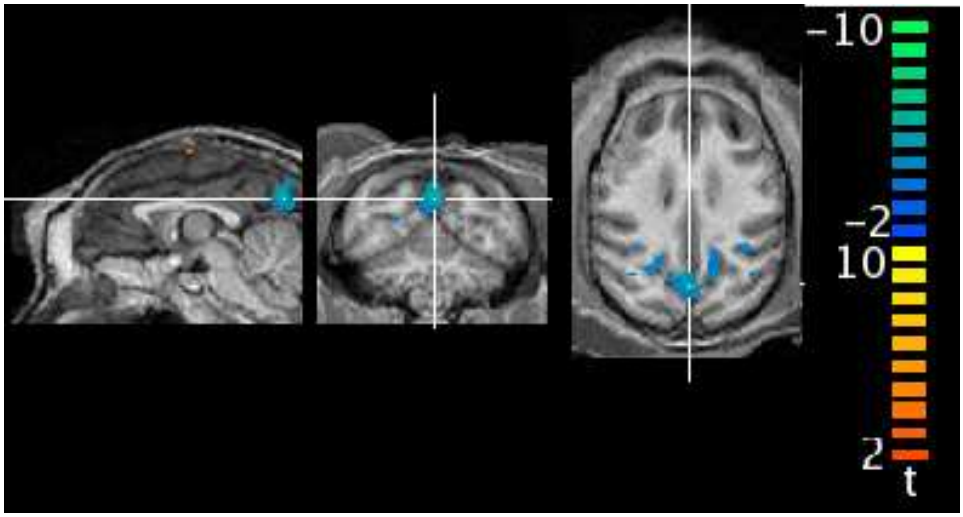

Figure 2.11: *Cluster 2 - sites of maximum influence of time elapsed since Methohexital injection*

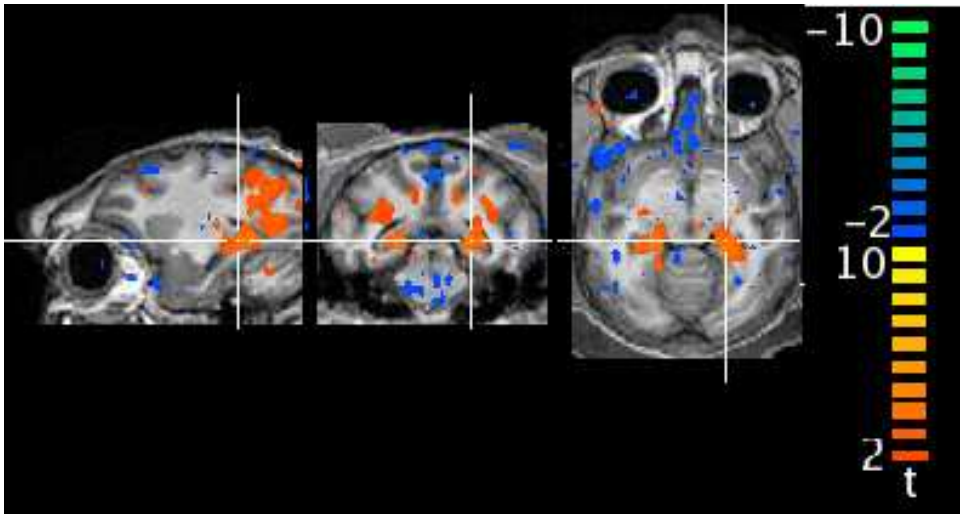

Figure 2.12: *Cluster 2 - sites of maximum influence of heart rate*

of the difference map indicated that higher Isofluorane levels yielded higher map values. This may be attributed to the vasodilating and metabolism reducing effects of Isofluorane [47]. Increased cerebral blood flow in conjunction with decreased neuronal activity will lead to an increase in oxygen saturation in the large veins that make up the main feature of the map of cluster 2. Increased oxygen saturation will reduce the paramagnetism of the venous blood and thus strongly increase the signal - potentially leading to the observed negative sign in the difference map.

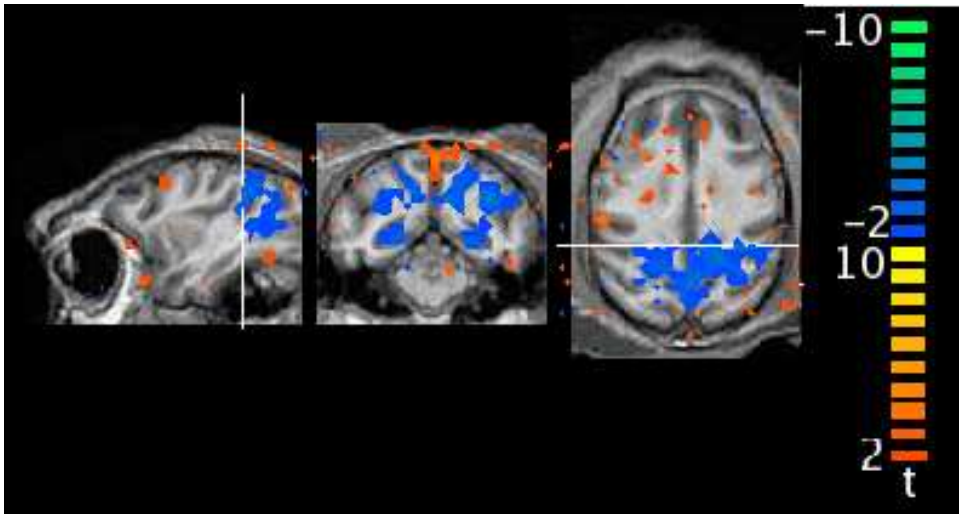

Figure 2.13: *Cluster 2 - sites of maximum influence of end tidal Isofluorane level*

Cluster 3

Cluster Description Cluster 3 showed largest cluster map values in the region of the vitreous humour of the left eye. As this eye was covered during scanning we could exclude that this component was due to the BOLD fMRI effect in the retina (retinal BOLD fMRI effects have been described in [32] for example). We rather propose that this signal component was generated by residual eye movements. Such movements were occasionally observed despite paralysis. While we aborted the experiments when large eye movements were observed during calibration of the stimulus setup (see figure 1.1) we cannot exclude that small residual eye movements were present during the scanning session. This view was supported by data from the single run component presented in figure 2.15. This component showed large signal maxima in both eyes that filled the vitreous humour completely. The time course of

this component was partially following the stimulation but also had erratic signal components (refer to the rightmost part of the timecourse display).

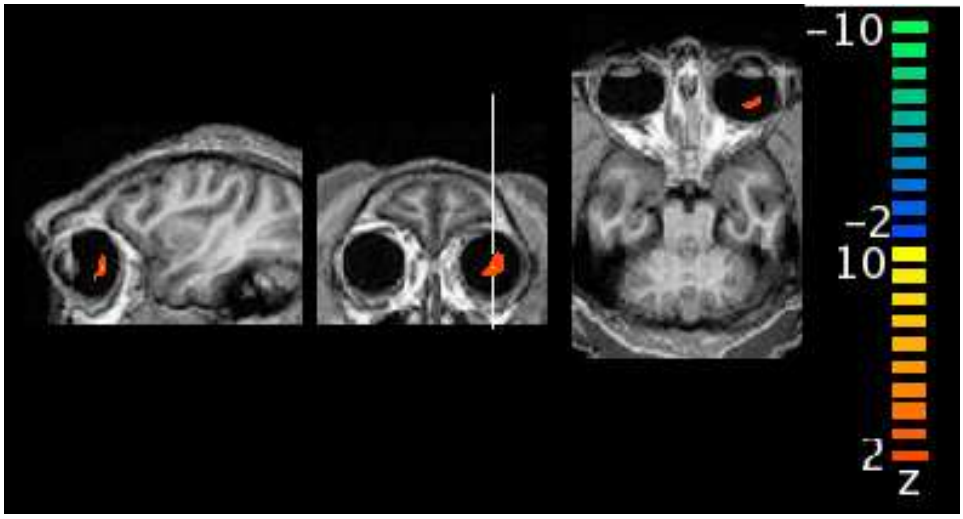

Figure 2.14: *Cluster 3 - thresholded z-value map at $|z| > 2$. Hairline indicates the position of the cluster map maximum. Coordinates relative to anterior commissure and midline: RL: 17.3mm (L) , AP: 21.3mm (A), DV: -9.3mm (V).*

Difference Maps Cluster 3 was only significantly influenced by the dose of Fentanyl given. The maximum of the difference map for this variable was found in the left occipital cortex, close to the representation of the fovea in area V1 (see hairline in figure 2.16). While it was conceivable that eye movements were coupled to signal changes in this region, it is unclear why Fentanyl should influence eye movements per se.

Cluster 4

Cluster Description The maxima of the cluster map of cluster 4 were found bilaterally in the liquor spaces between collateral sulcus and the brain stem (figure 2.17). This location might indicate that this component was of arterial origin. The time course of the corresponding single run member component (figure 2.18) showed an intermittent high frequency signal on the order of the Nyquist frequency of our scanning sequence. This signal frequency would be compatible with a signal component created by pulsatile flow. It is also obvious from figures 2.17 and 2.18, however, that cluster map and single run map did not correlate well. This may have been due to the

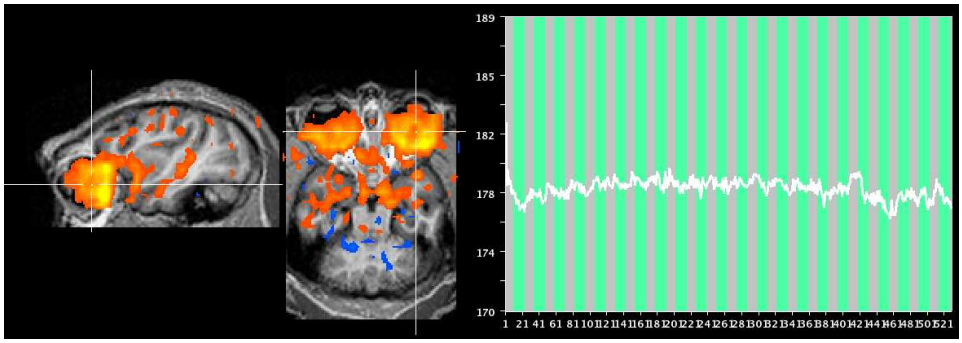

Figure 2.15: *Cluster 3 member component from single run (ID 040) - thresholded z-value map. Hairline indicates the position of the cluster map maximum. Coordinates relative to anterior commissure and midline: RL: 17.3mm (L) , AP: 21.3mm (A), DV: -9.3mm (V).*

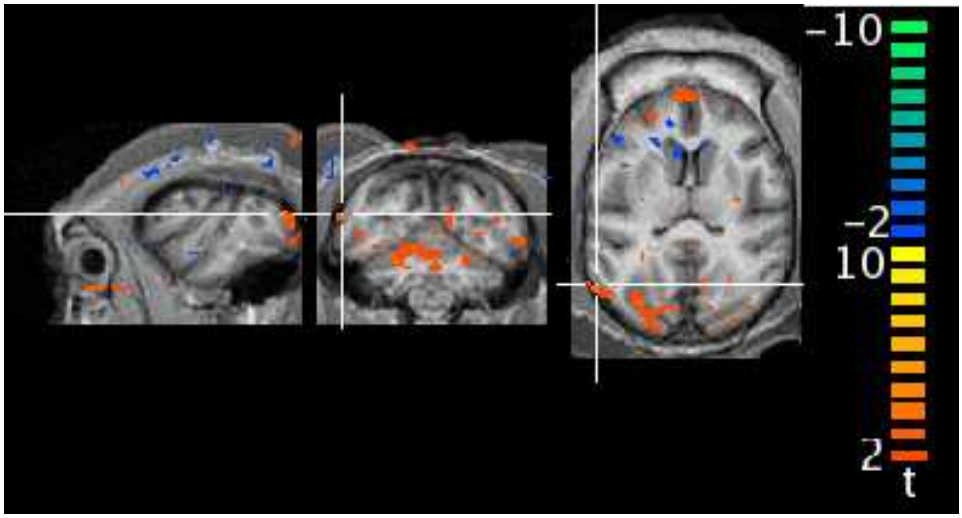

Figure 2.16: *Cluster 3 - sites of maximum influence of Fentanyl dose*

fact that the large arteries at the skull base were well aligned from single run component to single run component (in the cluster) while this overlap for smaller arteries may have suffered from slightly varying image distortions from single run component to single run component. Thus only the large and stable map features survived the averaging in the cluster map, while individual components showed a much richer structure. Note that a similar degradation of map features was also observed for cluster 2 that comprised larger and smaller venous structures (confer figure 2.9 and 2.10).

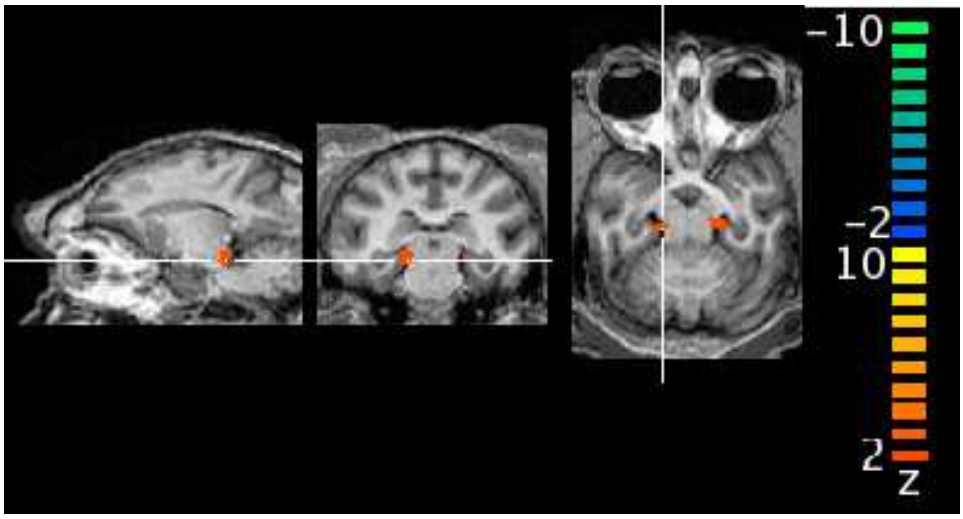

Figure 2.17: *Cluster 4 - thresholded z-value map at $|z| > 2$. Hairline indicates the position of the cluster map maximum. Coordinates relative to anterior commissure and midline: RL: -8.0mm (L) , AP: -15.3mm (A), DV: -7.3mm (V).*

Difference Maps Cluster 4 was significantly influenced by the independent variables *Fentanyl dose*, *heart rate* and *saline infusion rate*. This combination of variables is consistent with an arterial origin of the signal: Fentanyl has tachycardic effects. Variations in heart rate are bound to show in the arterial signal, especially due to changing inflow effects of unsaturated spins in the lower slices of the imaging stack [33, 62]. Saline infusion rate will change the intravascular volume and thus also influence the signal.

The difference maps for *Fentanyl dose* and *Saline infusion rate* showed a strong overlap (compare the arc shaped structures with an anterior knee and posterior ends in the middle of the maps in the transversal imaging sections in figures 2.19 and 2.20). In these overlap regions higher saline infusion rates

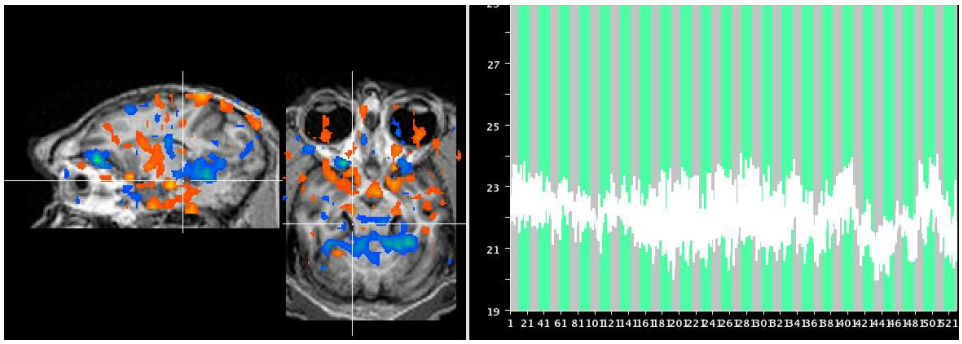

Figure 2.18: *Cluster 4 member component from single run (ID 040) - thresholded z-value map. Hairline indicates the position of the cluster map maximum. Coordinates relative to anterior commissure and midline: RL: -8.0mm (L) , AP: -15.3mm (A), DV: -7.3mm (V).*

led to less extreme values of independent component maps while higher Fentanyl doses increased the amplitudes of these parts of the maps. An interpretation of this effect based on the presented data is, however, difficult.

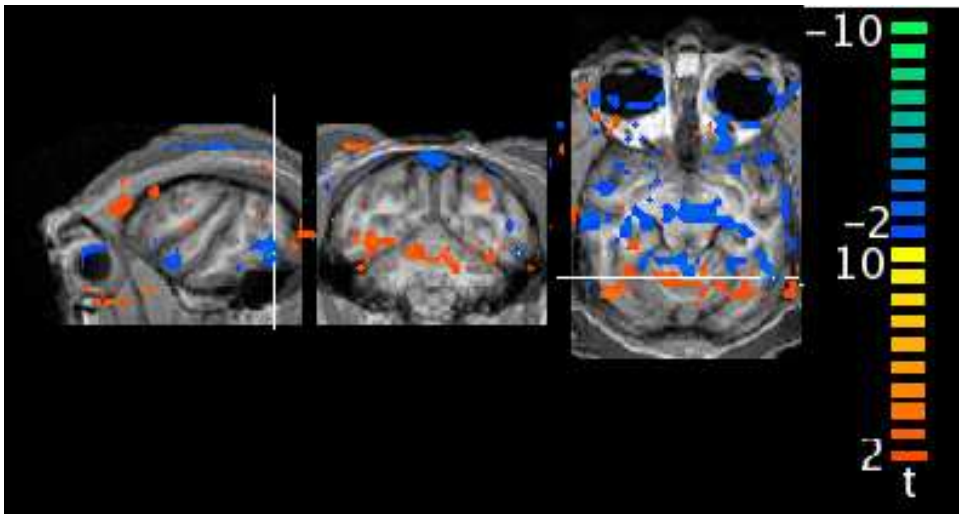

Figure 2.19: *Cluster 4 - sites of maximum influence of Fentanyl dose*

The difference map for the variable *heart rate* had a more occipital focus compared to those for Fentanyl dose and saline infusion rate (figure 2.21). While highly significant and symmetric[20] we cannot provide an interpreta-

[20]The symmetric difference maps followed the internal symmetry of the brain and were thus an indicator that differences were not due to chance or an artifact unrelated to physiology or anatomy.

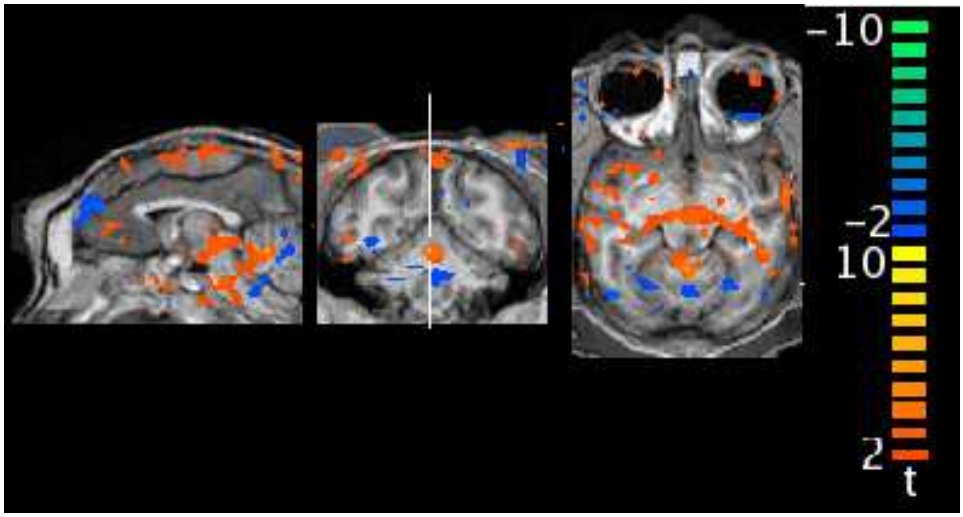

Figure 2.20: *Cluster 4 - sites of maximum influence of saline infusion rate*

tion of this map at present.

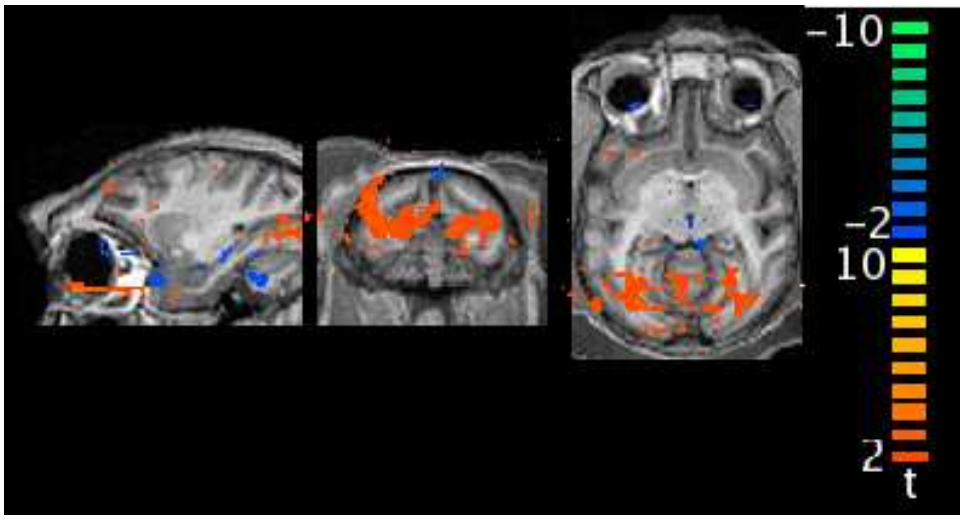

Figure 2.21: *Cluster 4 - sites of maximum influence of heart rate*

Cluster 5

Cluster Description The cluster map maximum for cluster 5 consisted of a large central midline structure 24 mm dorsal of the ACPC plane (figure 2.22). This led us to propose that this cluster represented central venous structures. Note that these could have been in principle decomposed to-

gether with the sagittal sinus in only one venous component. However, due to the external drive of visual cortex by the stimulation the time courses (columns of the mixing matrix) of occipital and central venous compartments were most likely too different for this to occur. The assumption that this cluster map represents venous structures was supported by the corresponding single run maps (figure 2.23). These single run maps showed strongly overlapping map features (central midline) and much richer detail than the cluster map (this is similar to our observation for cluster 2, sagittal sinus). In the single run component maps we observed that parts of this component followed the main sulci, additionally supporting a vascular origin of this signal component. The time course of the single run component loosely followed the time course of the stimulation, however, with large deviations towards the end of this particular run. The temporal spectrum of the displayed single run component was consistent with a hemodynamic BOLD response, as expected for venous signals.

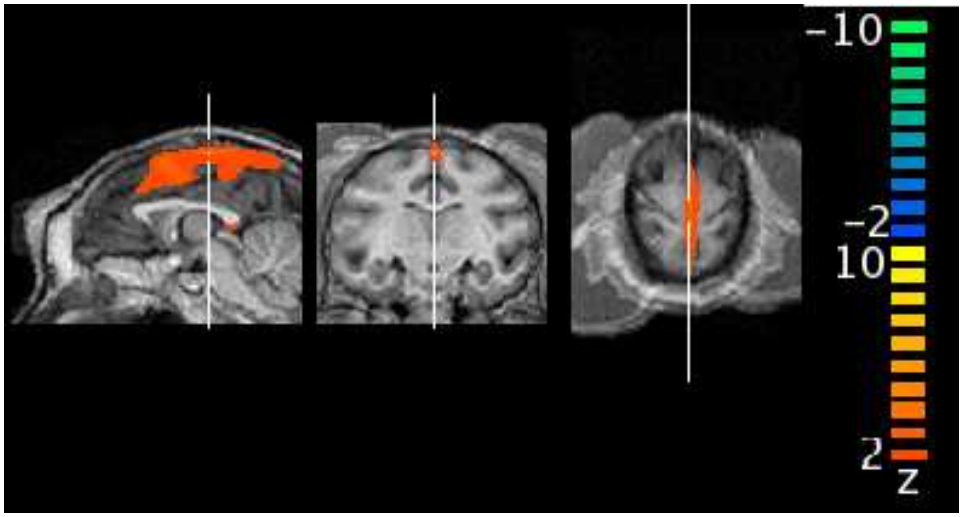

Figure 2.22: *Cluster 5 - thresholded z-value map at $|z| > 2$. Hairline indicates the position of the cluster map maximum. Coordinates relative to anterior commissure and midline: RL: 0.0mm (-) , AP: -10.7mm (P), DV: 24.0mm (D).*

Difference Maps Cluster 5 was significantly influenced by the independent variables *time since injection of Methohexital* and *heart rate*. Longer times since the injection of Methohexital led to more extreme values in the cluster member maps at the location of the cluster map maximum. This

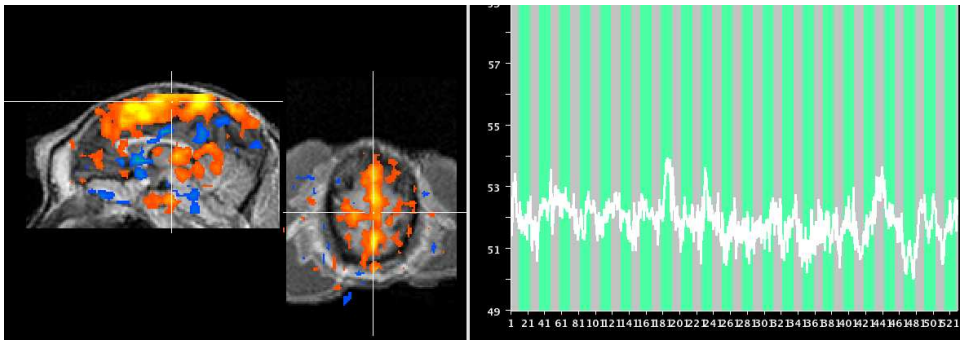

Figure 2.23: *Cluster 5 member component from single run (ID 040) - thresholded z-value map. Hairline indicates the position of the cluster map maximum. Coordinates relative to anterior commissure and midline: RL: 0.0mm (-) , AP: -10.7mm (P), DV: 24.0mm (D).*

was consistent with the assumption that this component reflects hemodynamic/BOLD fMRI responses to neuronal events, as barbiturates are known to strongly suppress neuronal activity (see, for example [45] and references therein). The maxima of the difference map for the independent variable *heart rate* were also located on the midline and in the sulci of temporal and parietal cortices, locations that were compatible with venous structures. Higher heart rate led to less extreme values in the cluster member maps. The interpretation of this finding is unclear at the moment.

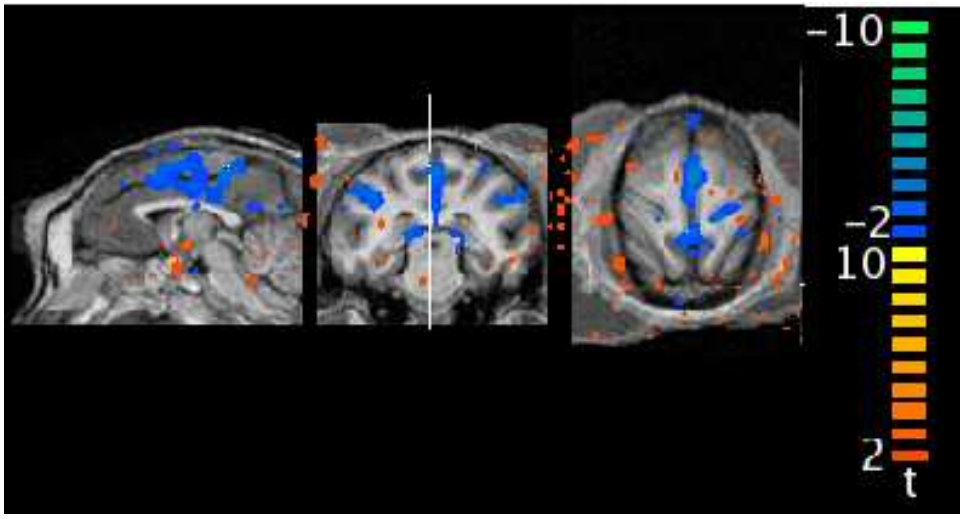

Figure 2.24: *Cluster 5 - sites of maximum influence of time elapsed since Methohexital injection*

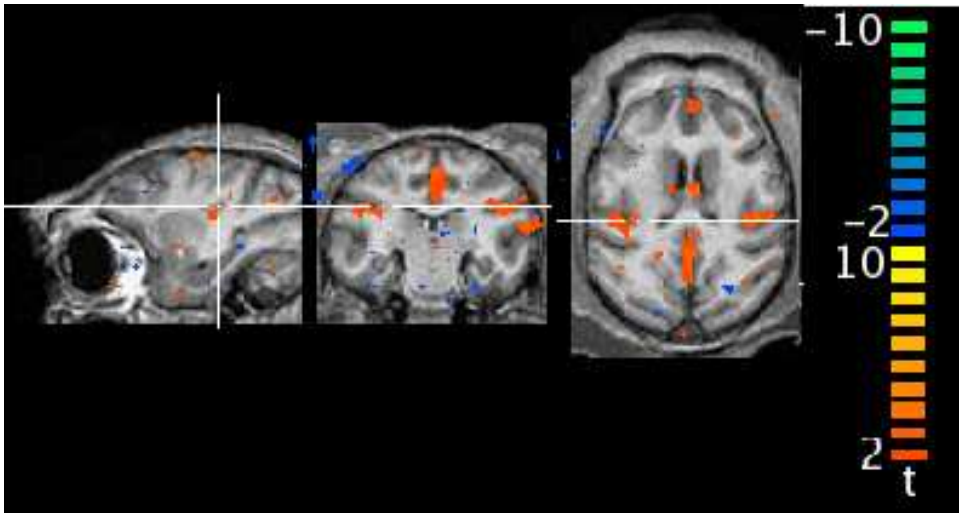

Figure 2.25: *Cluster 5 - sites of maximum influence of heart rate*

Cluster 6

Cluster Description The maximum of the cluster map of cluster 6 was located in the dorsomedial part of the orbita of the left eye (figure 2.26). The corresponding single run component maps had extended maxima that spatially trace the orbital fat of both eyes (figure 2.27). This part of the component map showed a sign reversal from positive to negative when going from the dorsal to ventral section of the orbita. The time course of the component map showed an erratic structure in the intermediate frequency range. One might therefore propose that this cluster, at least in parts, comprised signal changes due to eye movements, possibly of rotational nature around the LR axis. However, as will be pointed out below, the absence of any significant influences of independent variables on the maximum of this cluster map pointed to machine artefacts like RF instabilities as another likely source for this signal component.

Missing Difference Maps We did not find any significant changes between cluster subgroups with respect to any of the investigated independent variables. This would rather indicate machine related artefacts as a signal source, as opposed to eye movements as pointed out above. If this cluster represented eye movements one would expect a potential influence of the dose of Mivacurium Chloride, which we did not observe.

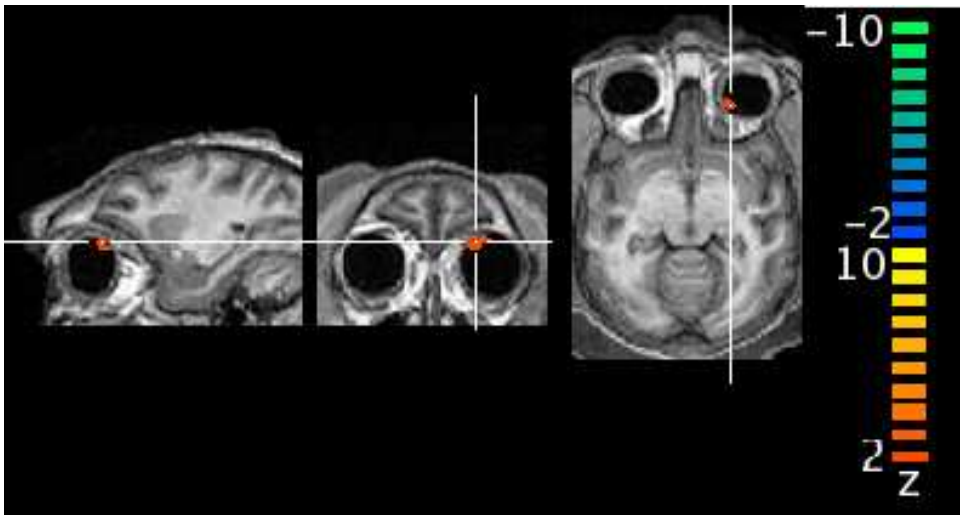

Figure 2.26: *Cluster 6 - thresholded z-value map at $|z| > 2$. Hairline indicates the position of the cluster map maximum. Coordinates relative to anterior commissure and midline: RL: 12.0mm (L) , AP: 21.3mm (A), DV: -2.0mm (V).*

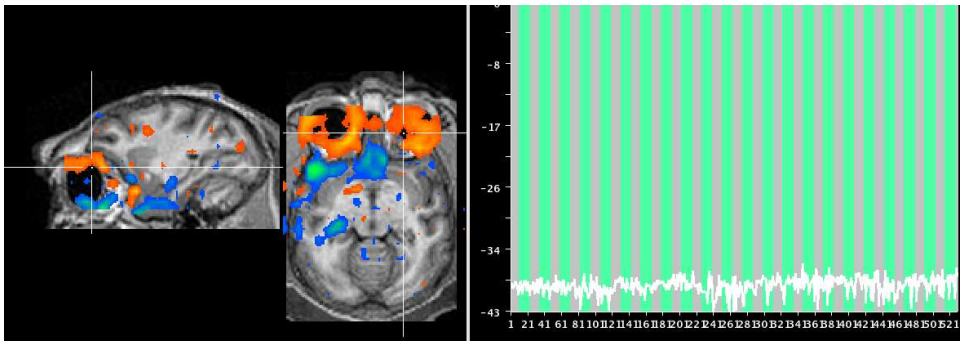

Figure 2.27: *Cluster 6 member component from single run (ID 040) - thresholded z-value map. Hairline indicates the position of the cluster map maximum. Coordinates relative to anterior commissure and midline: RL: 12.0mm (L) , AP: 21.3mm (A), DV: -2.0mm (V).*

Cluster 7

Cluster Description For cluster 7 no voxels with a z-value exceeding 2.0 were found. We therefore present the clustering results for this cluster at a *lowered threshold* (z > 1.2) in figure 2.28. Extremely low maximal z-values of a cluster map indicated that indeed features of single component maps do not overlap well. It is therefore unclear whether this cluster represented a valid signal component or was a forced mixture of several signal components. This cluster was, therefore, not analysed further.

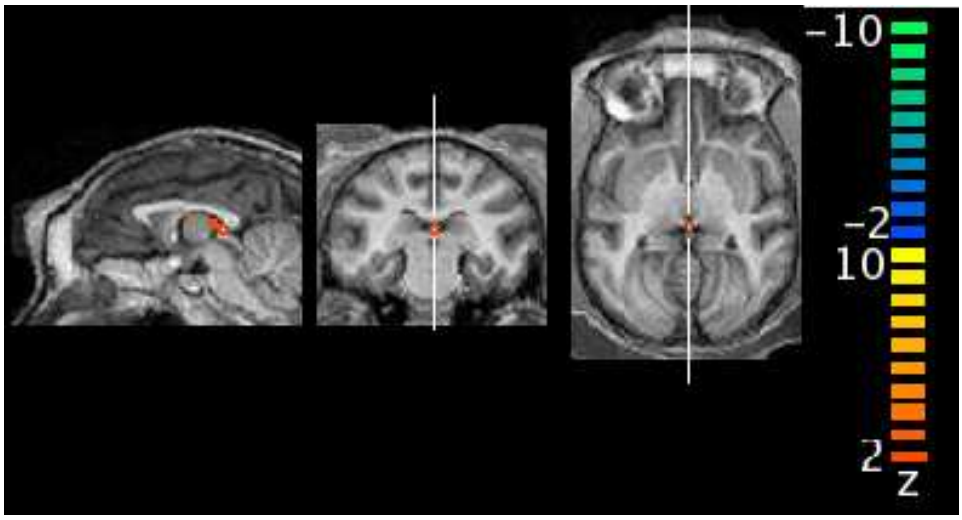

Figure 2.28: *Cluster 7 - thresholded z-value map at z > 1.2. Hairline indicates the position of the cluster map maximum. Coordinates relative to anterior commissure and midline: RL: 0.0mm (-) , AP: -14.7mm (P), DV: 2.0mm (D).*

Cluster 8

Cluster Description As for cluster 7 also for cluster 8 no voxels with a z-value exceeding 2.0 were found. We therefore present the clustering results for this cluster at a *lowered threshold* (z > 1.2) in figure 2.29. Extremely low maximal z-values of a cluster map indicated that indeed features of single component maps do not overlap well. It was therefore unclear whether this cluster represented a valid signal component or is a forced mixture of several signal components. This cluster was, therefore, not analysed further.

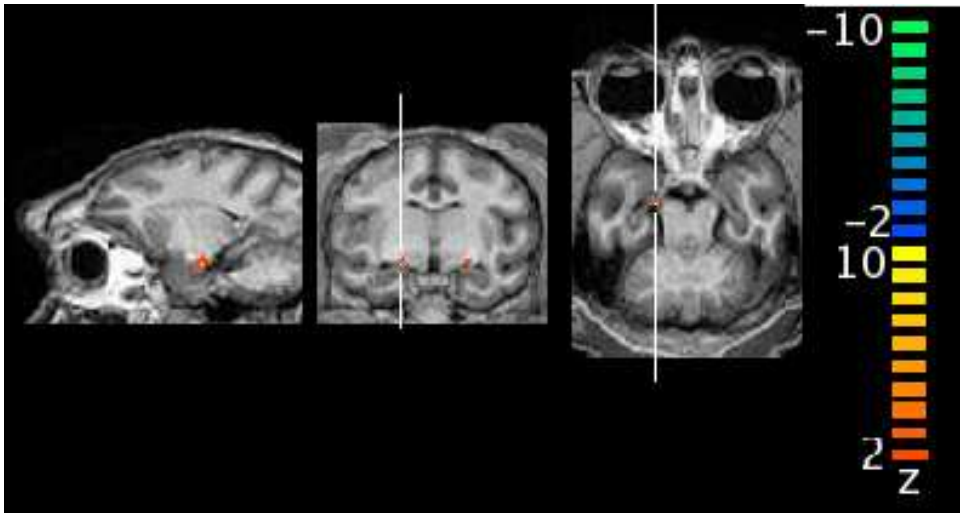

Figure 2.29: *Cluster 8 - thresholded z-value map at z > 1.2. Hairline indicates the position of the cluster map maximum. Coordinates relative to anterior commissure and midline: RL: -10.0mm (-) , AP: -8.0mm (P), DV: -8.7mm (D).*

Cluster 9

Cluster Description Maximum values of the cluster map for cluster 9 were found in the superior oblique muscles of both eyes. It seemed therefore highly likely that this cluster collected components that were related to eye movements. The corresponding single run component presented here also showed high values around the muscles of both eyes (most likely the reason for participating in this cluster) as seen in figure 2.31. This component however also had notable features at other locations. These other locations with signal were found displaced in the phase encoding direction of the images (anterior to posterior direction in our data). Therefore, the single run results were in principle still consistent with the hypothesis of eye movements because moving objects cause repeated artifacts in this direction over the whole image. The time course of the single run component, however, contained high frequency components that seemed rather atypical for eye movements, rendering the initial hypothesis for this cluster - eye movements - dubious. Unfortunately none of the investigated independent variables influenced this cluster significantly. We could thus not derive an alternative hypothesis for the origin of this cluster.

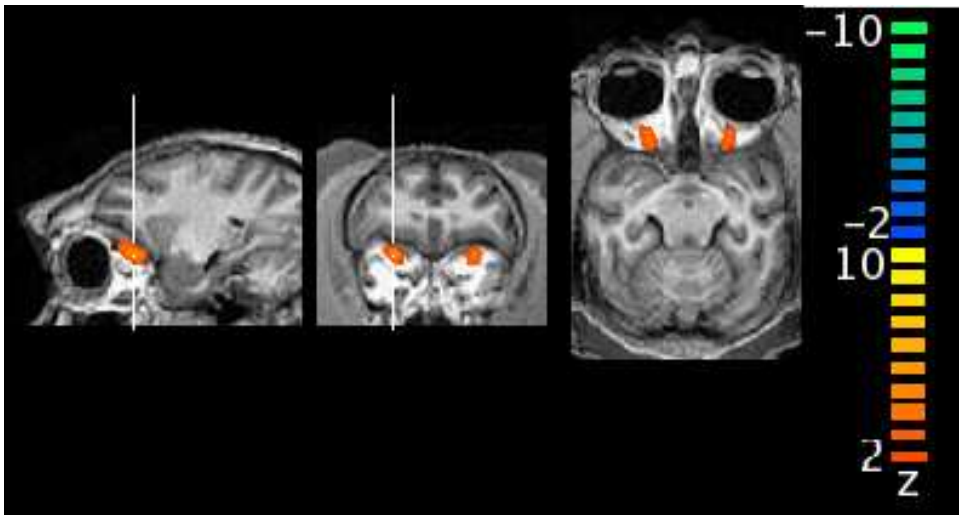

Figure 2.30: *Cluster 9 - thresholded z-value map at $|z| > 2$. Hairline indicates the position of the cluster map maximum. Coordinates relative to anterior commissure and midline: RL: -12.0mm (L) , AP: 11.3mm (P), DV: -6.0mm (D).*

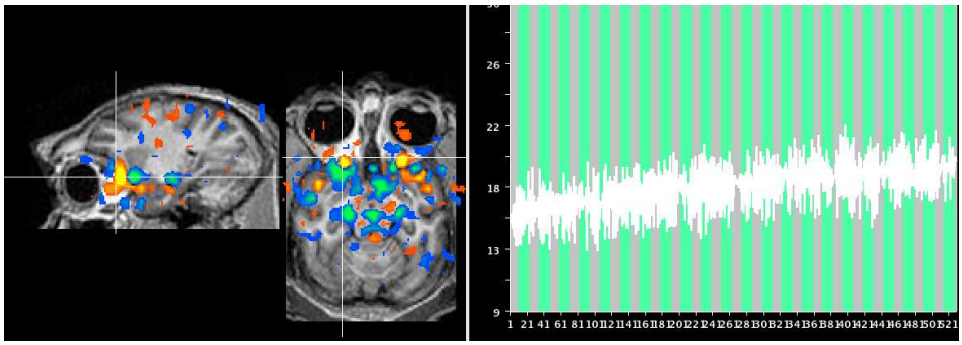

Figure 2.31: *Cluster 9 member component from single run (ID 040) - thresholded z-value map at $|z| > 2$. Hairline indicates the position of the cluster map maximum. Coordinates relative to anterior commissure and midline: RL: -12.0mm (R) , AP: 11.3mm (P), DV: -6.0mm (D).*

Cluster 10

Cluster Description The cluster map of cluster 10 showed distinct maxima around the lateral sulcus (but not the insula), the anterior subcentral sulcus and the superior ramus of the arcuate sulcus (possibly the frontal eye field) as can be seen in figure 2.32. The lateral sulcus contains secondary somatosensory cortex (SII) and the parietal ventral area (PV) (see [72]). These areas contain representations of the body surface including the face. The time course of the corresponding single run component map (figure 2.33) displayed small signal elevations correlated to the stimulation, and two larger deviations towards the end of the run. The time scale of these changes would be compatible with BOLD fMRI responses driven by neuronal activation. The correlation to the stimulus might additionally point in this direction. It is however unclear which aspect of the stimulation may have driven these, presumably somatosensory, responses.

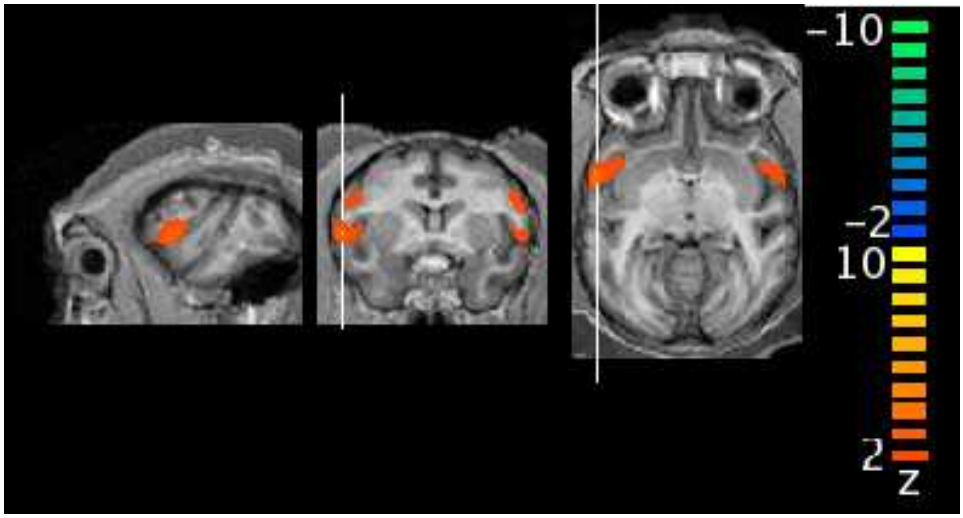

Figure 2.32: *Cluster 10 - thresholded z-value map at $|z| > 2$. Hairline indicates the position of the cluster map maximum. Coordinates relative to anterior commissure and midline: RL: -27.3mm (R) , AP: -0.7mm (P), DV: 0.7mm (D).*

Difference Maps This cluster map is significantly influenced by the variable *heart rate*. Higher values of the heart rate yielded less extreme values of the member components at the location of the main cluster map features (lateral sulcus, anterior subcentral sulcus and the superior ramus of the arcuate sulcus). Lower heart rates were present predominantly towards the

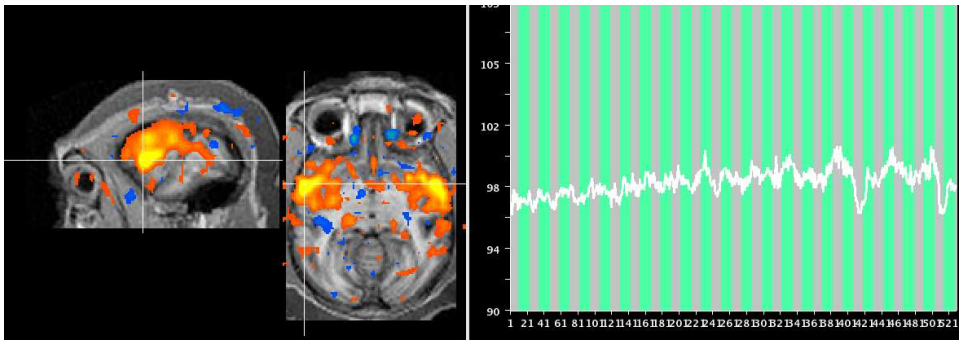

Figure 2.33: *Cluster 10 member component from single run (ID 040) - thresholded z-value map at $|z| > 2$. Hairline indicates the position of the cluster map maximum. Coordinates relative to anterior commissure and midline: RL: -27.3mm (R) , AP: -0.7mm (P), DV: 0.7mm (D).*

end of the experimental sessions, after several hours of anaesthesia, due to an accumulation of *active* [101] metabolites of Fentanyl. Heart rate in our experiments also correlated with depth of anaesthesia. Deeper anaesthesia - as indicated by smaller responses to somatosensory manipulation of the monkey during the experiment (irrigation of the eyes, emptying the bladder)- went along with lower heart rate and less variability of the heart rate. For an interpretation of this cluster two opposing findings would have to be reconciled: first, a location of the main cluster map features in secondary somatosensory cortices. Second, an *increase* of the extreme values of these map features with increasing depth of anaesthesia and stronger analgesia. Thus, while we found map features that well fit known anatomical subdivisions of the cortex, timecourses of single run maps that indicate BOLD fMRI responses to neuronal events and a significant result for an influence of heart rate, it was not possible to formulate a clear hypothesis about the origin of this cluster.

Cluster 11

Cluster Description The maximum of cluster map 11 is found in the vitreous humour of the right eye as depicted in figure 2.35. The single run member component from the run selected for presentation here (Monkey K; ID040 date: February 9^{th} 2004; run Nr.: 7, component 28) had unfortunately captured a large artefactual signal (see green anterior to posterior stripe in the left hemisphere in figure 2.36) in addition to the part of the map that led to clustering with cluster 11. To better asses the typical time

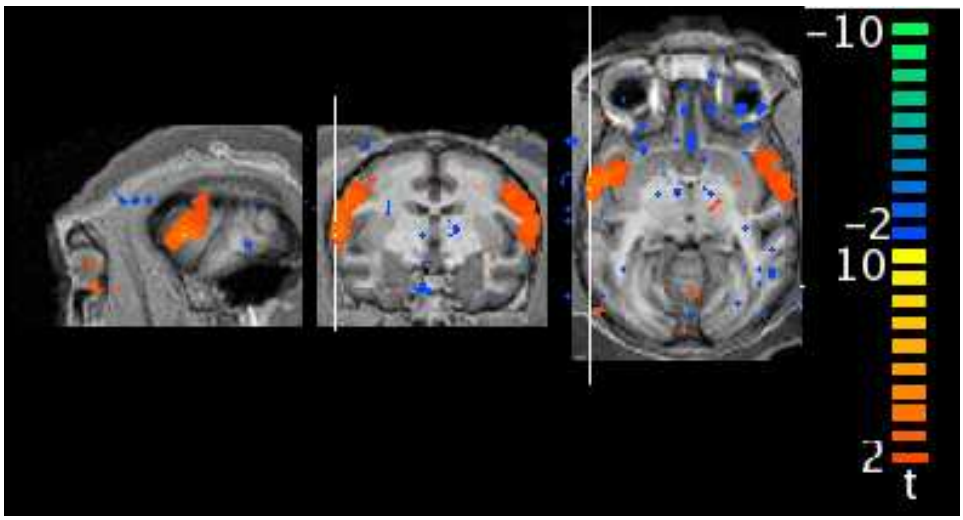

Figure 2.34: *Cluster 10 - sites of maximum influence of heart rate*

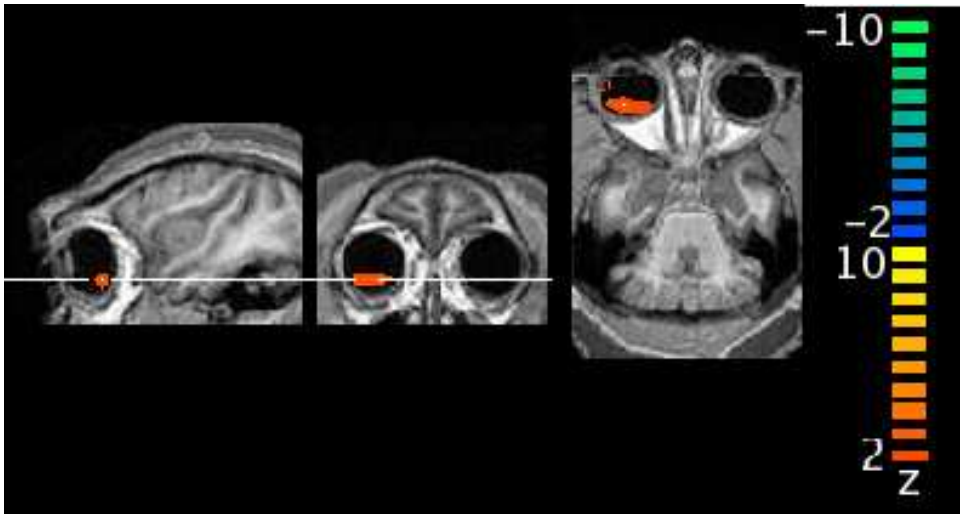

Figure 2.35: *Cluster 11 - thresholded z-value map at $|z| > 2$. Hairline indicates the position of the cluster map maximum. Coordinates relative to anterior commissure and midline: RL: -20.0mm (R) , AP: 21.3mm (A), DV: -13.3mm (V).*

course of a single run member component we therefore present an additional component from the cluster centre (Monkey K; ID 174 date: January 13^{th} ; run Nr. 14: , component 25; figure 2.37). This single run component map also showed main features in the vitreous humour of both eyes and in addition features that followed strong contrast gradients in the image, especially around the eye and the orbita. The timecourse of this artifact free single run component was dominated by high frequency signal fluctuations. The fact that both eyes, stimulated and non stimulated, were part of the maximum map features excluded the possibility that this component represented retinal BOLD fMRI effects. The high frequency timecourse pointed at a breathing related signal fluctuation[21] as a source of this component.

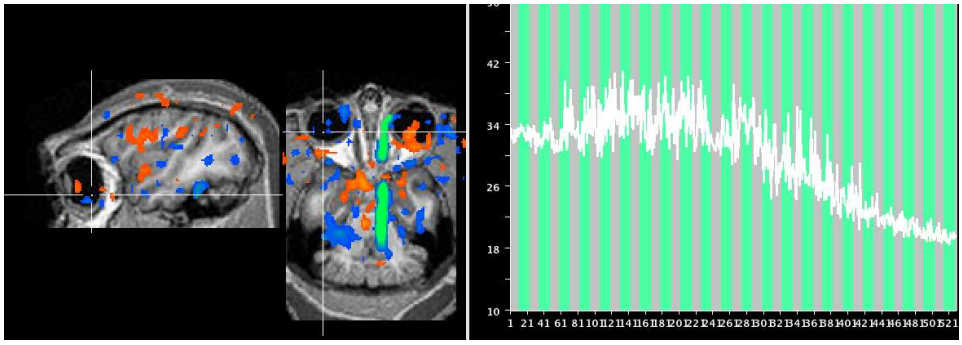

Figure 2.36: *Cluster 11 member component from single run (ID 040) - thresholded z-value map at $|z| > 2$. Hairline indicates the position of the cluster map maximum. Coordinates relative to anterior commissure and midline: RL: -20.0mm (R) , AP: 21.3mm (A), DV: -13.3mm (V). Note the large artifact (green stripe in anterior to posterior direction) captured by and possibly dominating this component.*

.

Missing Difference Maps We did not find a significant influence of any of the tested independent variables on cluster 11. This finding supported the notion that cluster 11 was due to breathing related artefacts, as breathing frequency was regulated independently of the other variables tested here.

[21] the breathing frequency was approximately 12 strokes per minute or 0.2Hz whereas the sampling frequency was $frac1image2seconds = 0.5Hz$, resulting in breathing artefacts appearing close to the Nyquist sampling limit.), either directly due to motion induced by the ventilation or via a change in the susceptibility of the lung that are more or less filled with paramagnetic O_2.

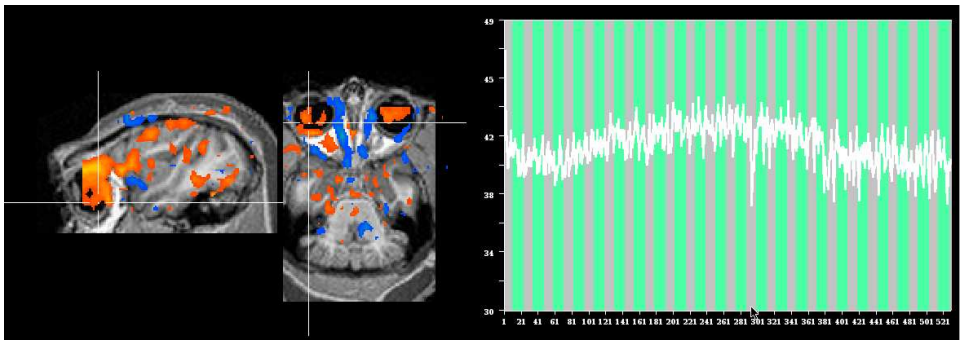

Figure 2.37: *Cluster 11 member component from an additional single run (ID 174) - thresholded z-value map at $|z| > 2$. Hairline indicates the position of the cluster map maximum. Coordinates relative to anterior commissure and midline: RL: -20.0mm (R) , AP: 21.3mm (A), DV: -13.3mm (V). This single run component is free of the artifact observed for the component in figure 2.36.*

Cluster 12

Cluster Description The maximum map feature of cluster 12 was found bilaterally at the ventral end of the lunate sulcus, corresponding to the border of visual areas V1 and V2 (figure 2.38). At this anatomical location a representation of the vertical meridian of the visual field, including its foveal part is typically found (see [108] for an early imaging study using 2-deoxyglucose mapping and [107] for an overview of imaging results from fMRI). Lowering the threshold for this cluster map expanded the map parts that were above threshold to most of areas V1 and V2. The anatomical location of the cluster map maxima coincides with stimulated parts of cortex found in the GLM analysis in chapter 1. The corresponding single run component maps also had its maxima bilaterally in visual areas V1, V2, V3 (figure 2.39). The single run component time course closely follows the stimulus with a signal shape compatible with BOLD fMRI responses driven by the visual stimulus (compare figure 1.1).

Difference Maps This cluster map was significantly influenced by the variables *body temperature* and *end tidal level of Isofluorane* as can be seen in figures 2.40 and 2.41. The locations of maximum changes in the difference map for the independent variable *body temperature* coincided with the main features of the cluster map (compare figures 2.38 and 2.40) although their centre of mass was slightly dorsal of the location of the highest z-values

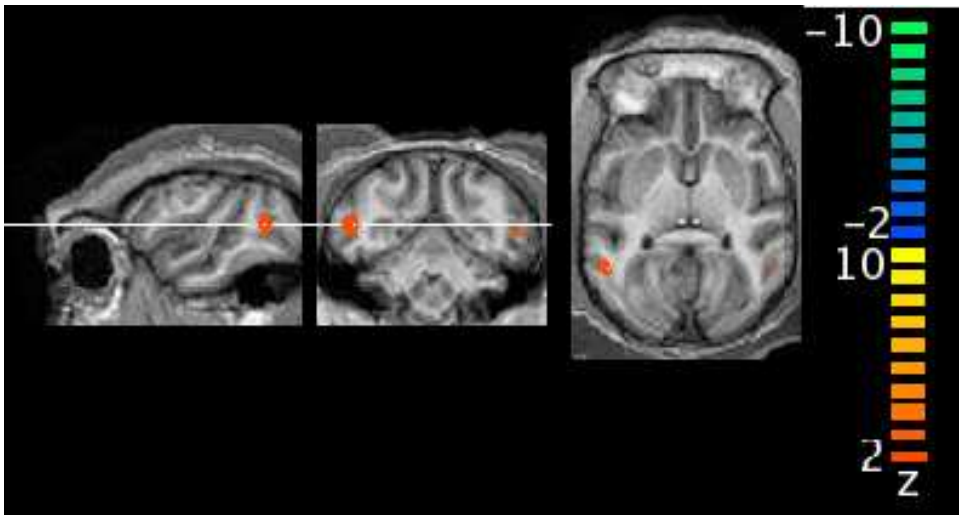

Figure 2.38: *Cluster 12 - thresholded z-value map at $|z| > 2$. Hairline indicates the position of the cluster map maximum. Coordinates relative to anterior commissure and midline: RL: -24.0mm (R) , AP: -26.7mm (P), DV: 3.3mm (D).*

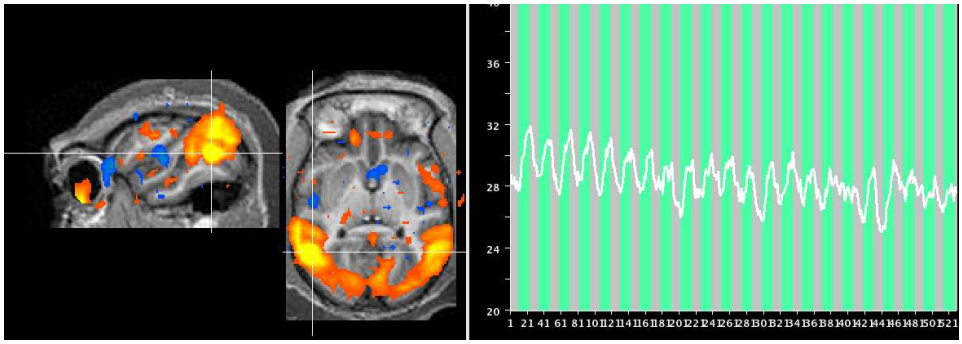

Figure 2.39: *Cluster 12 member component from single run (ID 040) - thresholded z-value map at $|z| > 2$. Hairline indicates the position of the cluster map maximum. Coordinates relative to anterior commissure and midline: RL: -24.0mm (R) , AP: -26.7mm (P), DV: 3.3mm (D). The part of the component in the right eye maybe retinal BOLD fMRI signal that has been slightly misplaced by susceptibility artifacts.*

.

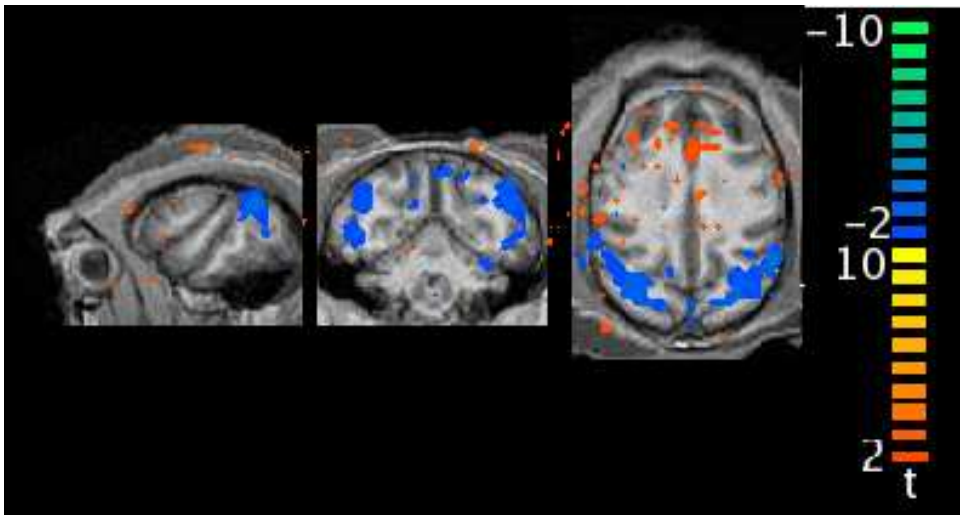

Figure 2.40: *Cluster 12 - sites of maximum influence of body temperature*

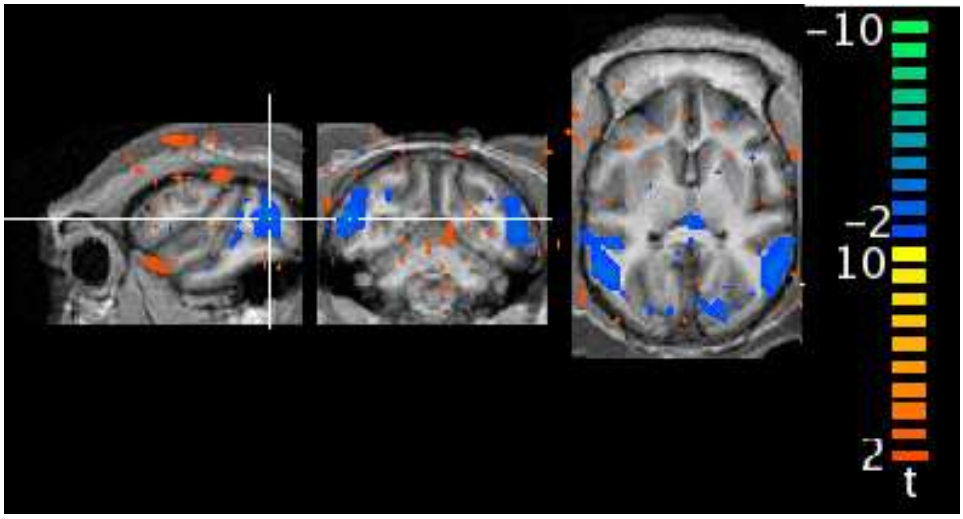

Figure 2.41: *Cluster 12 - sites of maximum influence of end tidal Isofluorane level*

in the cluster map. Independent components from runs with higher body temperature showed on average more extreme component map values in these locations. This finding was consistent with the previous result from the GLM analysis (chapter 1, table 1.2) where a higher body temperature led to a stronger BOLD fMRI response.

The locations of maximum changes in the difference map for the independent variable *end tidal level of Isofluorane* coincide well with the main features of the cluster map (compare figures 2.38 and 2.41). Higher values of the end tidal level of Isofluorane led to more extreme component map values.

2.3.2 Influence of Independent Variables

The influence of physiological or anaesthesia related independent variables was investigated as a means to help the interpretation of the independent component clusters we found. It is interesting, however, also to have a look at these effects sorted by the independent variables. Such an approach would of course be circular if a cluster was first assigned an interpretation based on the influential variables (e.g. 'this cluster is of venous origin because it is influenced by Isofluorane') and later on we attempted to make a statement on which physiological processes are influenced by an independent variable (e.g. 'Isofluorane influences the clusters of venous origin'). The approach is valid, however, if we confine ourselves to noting which independent variables had a detectable influence *on any cluster at all* and which didn't. It would also be valid if we had been able to derive the origin of a component cluster without looking a the influence of the independent variables first, which was the case for cluster 12.

Influential Independent Variables

The dose of Fentanyl influenced clusters 1, 3, 4 and 5. The Saline Infusion rate had an influence on clusters 1 and 4. The time since the initial injection of Methohexital only influenced cluster 2. The end tidal level of Isofluorane influenced clusters 2 and 12. An influence of heart rate was seen for clusters 4,5 and 10. The body temperature only influenced cluster 12.

Independent Variables without a Detectable Influence on cluster Maps

Neither the dose of Mivacurium Chloride nor the non invasively measured systolic blood pressure nor the inspiratory fraction of oxygen[22] FiO_2 had a detectable influence on any of the investigated cluster maps (clusters 1-12).

2.4 Discussion

2.4.1 Finding the Correct Number of Independent Components

As pointed out in the methods section current ICA algorithms cannot determine how many independent components are hidden in a given dataset and our choice of 30 components to be extracted was based on a heuristic approach. Some validity can be assigned to this choice *post hoc* as clustering picked out *one* cluster that well reflected the functional BOLD fMRI response in visual cortex. Severe over fitting of the data by extraction of too many independent components would have most likely resulted in several clusters that reflected this functional BOLD fMRI response. It may be argued that the clusters 2 and 5 also represented BOLD fMRI responses and should thus be part of cluster 12 - indicating over fitting. These clusters however, exhibited strongly differing time courses (although this is not a result required by spatial ICA) indicating they reflected truly different processes. Another concern is whether actually too few components were chosen for extraction - resulting in components that were still mixtures of other components. As we reduced the dimensionality of the dataset to 30 using PCA *before* ICA, the ICA algorithm estimated the maximal number of independent components that could be estimated from the reduced data. Differences between the hypothetical 'true' independent components and those we obtained here are, thus, due to the dimensionality reduction via PCA. This dimensionality reduction kept more than 99% of the variance in investigated runs. We can therefore claim that alterations of the components were small in size. The maximum number of independent components $NrCpts_{max}$ that can be reliably estimated from a dataset with n realisations of the random variables is usually approximated by [24]:

$$NrCpts_{max} \approx 30 \cdot n^2 \tag{2.12}$$

[22] In the analysis of difference maps we looked for *time independent* effects of FiO_2. As in the GLM Analysis of the Pilot experiment we did not find any.

The number n of realisations of the random variables in our dataset is given by the number of voxels which is approximately 27000. The number of reliably extractable components is thus around 30. Our choice therefore avoided over fitting, while the remaining variance after PCA dimensionality reduction guaranteed that the extracted independent components would describe the true data well.

2.4.2 Clustering

Results of the clustering algorithm are displayed in figures 2.2, 2.3 and 2.4. The mean intra cluster dissimilarities were, as expected, slightly higher than those reported in the literature [35] due to the omitted spatial smoothing in our analysis. Clusters 1-6 were relatively compact with few outliers. This indicated that indeed similar, corresponding components from each run were clustered together. For clusters 7-12 this did not hold. The number of members of the more dense cluster core in these clusters was comparable to the number of 'outliers'. This indicated that the component type that formed the cluster core was simply not present in all of the investigated runs. The clustering algorithm then forced dissimilar components into the cluster. This result was expected for example for cluster 12, representing stimulus driven BOLD fMRI activity. This stimulus driven activity was absent in runs that were acquired early after injection of Methohexital as demonstrated by the GLM Analysis (figure 1.3). From these runs other components that were most similar to the BOLD fMRI activity were forced into the cluster.

The fact that components from potentially different origin enter one cluster slightly alters the interpretation of significant difference maps of an independent physiological or anaesthesia related variable: Significant results could also indicate that the independent components from one subgroup form a more homogeneous subcluster than those from the other subgroup. These significant results could be interpreted as an appearance or dissappearence of that subgroup with changes in the independent variable rather than a gradual modulation of a certain component process that had been present in both subgroups.

Replication of Findings from the GLM Analysis - Cluster 12

As in other ICA studies that analyse data from an experiment initially designed with a GLM analysis in mind our ICA results can be compared to those of the GLM analysis. Here, we were able to show that ICA extracted

the components that were known from a previous GLM analysis (e.g. stimulus related BOLD fMRI activity, extracted in cluster 12). Moreover, we could replicate the influence of the parameter *body temperature* on the BOLD fMRI response to stimulation as it was observed in the Pilot study (table 1.2). The influence of the parameter *end tidal level of Isofluorane* was also reproduced. This finding was surprising as the amplitude of BOLD fMRI responses (that are the assumed source of this cluster 12) is reported to fall with increasing levels of Isofluorane. One reason for the observed behaviour may be that rather small variations in this variable were used in our experiments (see table 2.2), whereas in previous studies larger variations were used [29]. It is also possible that the influence of Isofluorane renders the venous compartment more visible due to increased flow, resulting decreased overall levels of deoxyhemoglobin and reduced local field inhomogeneity. This would increase the overall MR signal level, but reduce stimulus driven BOLD fMRI responses as reported in [29]. This finding hints at the possibility that spatially clustered components may share the same maps but represent distinct physiological processes. For an inhomogeneous cluster such as cluster 12 this possibility should be considered.

Traces of stimulus driven hemodynamic and metabolic changes were actually found in three distinct clusters (clusters 2,5,12). Cluster 12 was located at the site of neuronal activation and close by venous structures as described above. The two other clusters (2, 5) were located at very large draining vessels. Although all three clusters partially reflect functional BOLD fMRI activation, they were separated by ICA due to their differing locations (via clustering) and time courses (on the single run level).

Identification of Signal Components Unrelated to Physiology

Cluster 1 is a clear example for a component that was reliably present in all investigated datasets (hence the high degree of clustering, see figures 2.3 and 2.2). This component did most likely represent the effect of shim drifts and resulting image drifts due to thermal instabilities of the MR Scanner. Effects of this kind were not easily detectable in the data after the k-space motion correction was performed by the MR Scanner to correct for the drift - they did however contribute to variance in all of our datasets as revealed by ICA. Detection of unexpected artefacts or signal components is one of the strengths of a data driven analysis approach, and was nicely illustrated by this finding. The detected artifact could now be removed from the data to enhance the sensitivity of the GLM analysis by removing extraneous, non

physiological variance not covered by the GLM model.

Clusters with Maxima at the Eyes

Three clusters (3, 6, 9) were located at positions indicating potential eye movements (despite paralysis). In none of these clusters independent variables influenced the cluster map at the site of its maximum. This finding did not confirm the hypothesis of eye movements as an influence of the dose of Mivacurium chloride would be expected. It does not disprove, however, the hypothesis of eye movements either, as the variations in dose might have been too small to detect such an effect. Another reason for a null effect of the dose of Mivacurium chloride may have been the development of a tolerance for the agent over repeated anaesthesia sessions, obscuring an actual dose effect. One further cluster (cluster 11) also had its maximum at the eyes, however, the missing influence of any independent variable and the single run time courses made us hypothesise that the observed signal component may have been due to breathing related fluctuations in the magnetic field homogeneity.

Cluster 4

The location of the cluster map maxima of cluster 4 indicated a potential arterial origin of this component cluster. Individual component time courses and the set of influential independent variables (Fentanyl dose, rate of saline infusion, heart rate) are compatible with this interpretation.

Cluster 10

Cluster 10 had a well circumscribed maximum of the cluster map in secondary somatosensory cortices, single run time courses compatible with BOLD fMRI responses and a clear influence of heart rate on the cluster map. It is however unclear what process would drive neuronal activation in secondary somatosensory cortices in our experiment. It might be considered that some somatosensory stimulus, possibly of visceral origin, which was constantly present throughout the experimental run presented in figure 2.31 was gated by the arousal produced by the visual stimulus and that we therefore observed some degree of stimulus correlation.

Other Components

For several other clusters we found that the maximum z-value of the cluster map did not exceed 2, possibly indicating forced clustering of components from a variety of sources. These clusters were not analysed further.

2.4.3 Testing for Dependence on Physiological Variables after ICA versus Direct Testing of the Full Spatio-Temporal Datasets

ICA transforms the 'as recorded' spatio-temporal fMRI data (3+1 dimensional) to a more abstract representation (n independent component maps in 3 D space and n corresponding time courses). This was done using *algorithms* that try to implement the abstract concept of statistical independence by maximising the negentropy of the resulting 'independent' components or minimising their mutual information. Subsequently we clustered the resulting components to find those that were reliably present over repeated runs and across individual monkeys. The member components of clusters that indicated this type of reliability were then tested for an influence of physiological or anaesthesia related variables. How does this novel approach compare to a model based investigation of an influence of these variables?

It is possible to test for the influence of these variables on a *univariate predefined dependent variable* - like the BOLD fMRI response amplitude in a region of interest defined by a GLM analysis as it was done in chapter 1. Note, however, that all of the analysis presented in chapter 1 only covers a tiny aspect of the data - merely the 1% signal change that is contributed by stimulus driven BOLD fMRI responses and covered by cluster 12 in the ICA analysis. Effects of physiological or anaesthesia related variables on aspects of the signal that were unrelated to visual stimulation had to be completely ignored in the GLM analysis.

It is hard to conceive how a more general investigation of the various influences of physiological or anaesthesia related variables could be performed on the *untransformed* spatio-temporal dataset. A 4-D (3D space x time) point wise statistical comparison of groups of runs with different values of the independent variable would require the effects to share more or less identical time courses over all runs to yield significant effects. While this requirement is fulfilled for stimulus driven effects it is almost inevitably violated for most other effects. Averaging the data per run across time to obtain maps comparable to the ones obtained with ICA will also be of no

use if the effects of physiological or anaesthesia related variables concern phenomena that do indeed have a time structure (like e.g. vasooscillations that are observed under anaesthesia [70]). ICA with subsequent clustering circumvents this problem by allowing for individual time courses of the effects in each separate run and just exploiting overlapping map features for clustering the components into a group to be analysed.

2.4.4 Influential and Non-Influential Independent Variables

Most of the investigated independent variables had an influence on at least one of the investigated component clusters. Influential variables comprised: dose of Fentanyl, saline infusion rate, time since the initial injection of Methohexital, end tidal level of Isofluorane, heart rate and body temperature. All of these variables must be tightly monitored and controlled in order to perform an artifact free BOLD fMRI experiment under anaesthesia. Notably the dose of Mivacurium Chloride and the non invasively measured systolic blood pressure did not have a detectable influence. Changes in the dose of Mivacurium chloride, thus, did not seem to influence physiological parameters in an way that MRI could retrieve the effect (once its basic paralytic action was established, which was the case in the investigated runs of our study). Effects of changing blood pressure on the BOLD fMRI signal have previously been reported in the literature [65]. An effect of systolic blood pressure detectable by fMRI may have been missed in our study due to a variety of reasons. First and most likely, the signal to noise ratio of the *non invasively measured* blood pressure signals may have been to poor to detect subtle effects. Previous studies used intra arterial measurements, instead, which could not be safely performed with our equipment. Second, the MRI signal is most sensitive to flow changes, which are auto regulated in the brain and are, therefore, at least partially independent of central blood pressure.

2.5 Conclusion

ICA analysis of fMRI data acquired under anaesthesia revealed several major MRI signal contributions other than stimulus driven BOLD responses.

A major remaining motion artifact due to machine related signal drifts could be discovered (cluster 1) even though k-space based motion correction had been performed on the MR scanner.

Traces of stimulus driven hemodynamic and metabolic changes were

found in three clusters (2, 5, 12) with different locations and physiological significance (cluster 12 - activated parenchyma and local vessels; clusters 2, 5 - large downstream vessels). These clusters were influenced by variables that were compatible with a venous origin of the signal (clusters 2, 5, 12) and BOLD fMRI responses to neuronal activation (cluster 12). The major influential factor on BOLD fMRI responses which was detected in the pilot experiment (body temperature) was replicated in the ICA analysis.

Three clusters were found which had maxima at the eyes (clusters 3, 6, 9). However neither single run time courses nor analysis of the influence of independent variables could confirm or disprove the hypothesis that these clusters were due to eye movements.

One cluster (10) had clear maxima at identifiable cortical locations (secondary somatosensory cortices, bilaterally) and single component time courses indicating a neuronal origin of this component. Moreover this cluster was significantly influenced by heart rate. We cannot give a clear interpretation of this cluster, however.

The fact that not all clusters were well clustered, indicates that more sophisticated clustering algorithms are necessary in future research on group ICA which allow for clustering only components of identical origin by using variable cluster sizes. This is, however, a difficult problem for most clustering approaches.

We conclude that ICA was sensitive enough to replicate findings of the GLM analysis, while detecting a variety of important additional signal components. Despite our efforts to further the interpretation of the results of independent component analysis in fMRI by testing for the influences of several independent variables, not all reliably detected components could be interpreted. This was most unfortunate for our findings in secondary somatosensory cortices which will require further research.

The analysis of influential versus non-influential independent variables revealed that at least the parameters *dose of Fentanyl, Saline infusion rate, time since the initial injection of Methohexital, end tidal level of Isofluorane, heart rate and body temperature* must be carefully monitored and tightly controlled to perform BOLD fMRI measurements under anaesthesia which are reasonably devoid of confound influences. The dose of the paralytic Mivacurium Chloride does not seem to influence the BOLD MRI signal critically, given that its paralytic effect is present at all. As in the GLM analysis we could not detect a *time independent* effect of inspiratory fraction of oxygen FiO_2. The implications of the latter result are broader, however, because ICA did not detect a time independent effect in *any* of the independent

component clusters, while in the GLM analysis we only investigated the stimulus driven BOLD fMRI responses (contained in cluster 12).

Summary

This thesis investigated the influence of the parameters of a common anaesthesia protocol based on the combination of Isofluorane and Fentanyl that is frequently used in a clinical setting and in animal research on BOLD fMRI responses. In addition we tried to investigate whether anaesthesia related parameters or physiological variables influenced other parts of the MRI signal, that were identified using Independent Component Analysis. All investigations were performed in macaque monkeys as their brains share important geometrical features with the human brain that are relevant for functional Magnetic Resonance Imaging studies (the macaque brain like the human brain is gyrencephalic while the rat brain for example is lissencephalic). In primates like the macaque there is also a better chance that important biochemical processes and agents that play a role under Anaesthesia and Hyperoxia are closer to their human counterpart than in an experimental preparation that uses rodents for example.

In the first part of this thesis we investigated the influence of anaesthesia related and physiological variables on BOLD fMRI responses using a *model driven analysis*. We tested for an influence of these independent variables on the BOLD fMRI response that was identified using a general linear model with predictors defined by the time course of a visual stimulus convolved with an *a priori* model of the hemodynamic impulse response. For the influence of some of these variables converging evidence was found in the literature. Existing results for the influence of elevated levels of the *inspired fraction of oxygen* FiO_2 and the ensuing arterial hyperoxia were contradictory, however. Hyperoxia is present in many anaesthesia protocols used in animal blood oxygen level dependent (BOLD) functional magnetic resonance imaging (fMRI) studies. Nevertheless, little data exist on the influence of hyperoxia on the magnitude of stimulus induced relative changes in BOLD fMRI signal (ΔBOLD%). No study to date investigated these effects in a time resolved manner, although cerebral vasoregulation offers sites for a time dependent interaction of hyperoxia and ΔBOLD%. Here

we investigated time dependent effects of an inspiratory oxygen fraction of 90%. We tightly clamped end tidal CO2 and body temperature and recorded physiological parameters relevant to the regional cerebral blood flow (rCBF) in macaque monkeys anaesthetised with Isofluorane and Fentanyl while using visual stimulation to elicit ΔBOLD%. To clarify whether changes in ΔBOLD% arose from changes in baseline blood oxygenation or rather altered neuronal or vascular reactivity, we directly measured changes in the regional cerebral blood volume (rCBV) using monocrystalline ion oxide nanoparticles (MION) as contrast agent. In visual cortex we found a biphasic modulation of stimulus induced ΔBOLD% under hyperoxia: We observed first a significant decrease in ΔBOLD% by 24% for data averaged over the time interval 0-180 minutes post onset of hyperoxia followed by a subsequent recovery to baseline. rCBV response amplitudes were decreased by 21% in the same time interval (0-180min). In the lateral geniculate nucleus (LGN), we neither found a significant modulation of ΔBOLD% nor of MION response amplitude. The cerebrovascular effects of hyperoxia may, therefore, be regionally specific. We formulated an extended version of the deoxyhemoglobin dilution model used to model the BOLD fMRI response that explicitly took into account the fact that under hyperoxia a part of the brain's oxygen consumption is supplied directly via the plasma. To our knowledge this fact has been completely ignored in the literature that investigated BOLD fMRI under hyperoxia. Predictions of this model do not, however, well describe our experimental findings, especially the time dependence and the regional specificity of the effects of hyperoxia. To reconcile the model with experimental findings we therefore had to assume altered neuronal activity or altered neurovascular coupling.

Of these two possibilities the assumption of altered neuronal activity under hyperoxia is more easily reconciled with the complete set of experimental findings presented here for three reasons. First, it is known that *hyperbaric* hyperoxia alters neuronal excitability ultimately leading to epileptic seizures. Here, we only applied hyperoxic ventilation at atmospheric pressure. However, it is hard to conceive how the action of hyperoxic ventilation on the brain should fundamentally change when higher absolute pressure is applied, as higher pressure alone does not have such an effect. We therefore can assume that the biochemical interactions that lead to the excitability changes in hyperbaric hyperoxia, especially the stimulation of neuronal Nitric Oxide Synthase, are also at work when ventilating with one atmosphere of oxygen. Second, the fundamental differences in the wiring of neuronal circuits in the cortex and the LGN yield a parsimonious explanation for the differential

effect in these two structures. Excitatory feedback loops in the visual cortex will enhance effects of excitability changes while the almost exclusively inhibitory feedback loops in the LGN will dampen any such change. Third, the ability of visual cortex to rapidly change synaptic weights could be the underlying mechanism of the temporal dependency of the observed effects.

We conclude that the use of hyperoxic ventilation in experiments that try to elucidate mechanisms of neurovascular coupling and of hemodynamic responses should be strictly avoided unless it is used as a controlled stimulus in its own right.

Moreover, we provide for the first time a detailed description of the influence of the barbiturate Methohexital on the amplitude of BOLD fMRI responses. We found that these influences could be detected for up to *5 hours* after the injection of this barbiturate, while its anaesthetic action at the doses used was in the range of a few tens of minutes at most. We also provide for the first time a precise estimate of the influence of body temperature on the amplitude of BOLD fMRI responses. The observed temperature dependency was higher than expected. We found that controlling the body temperature in a range of 0.5°C as it is frequently reported in the literature was insufficient for precise BOLD fMRI measurements.

In the second part BOLD fMRI data from two monkeys were reanalysed using spatial independent component analysis (ICA) - a multivariate, *model free* exploratory approach used here to describe the four dimensional fMRI datasets in the form of spatially independent maps and their associated time courses. This approach can reveal signal components that are *not related to any stimulus or other predefined event* and can have arbitrary time courses that differ over repetitions of the experiment.

Multivariate model free analysis techniques are especially suited when little is known about the signal at hand, as it is the case for BOLD fMRI data that were acquired *under anaesthesia*. Under anaesthesia a variety of physiological parameters that are tightly linked with each other in the normal awake state and influence the BOLD fMRI signal together become unlinked, increasing the complexity of the experimental design and the number of independent confounds. The independent levels of the different blood gases under mechanical ventilation are an example for this enhanced experimental complexity. Moreover the influence of anaesthetics and paralytics on the BOLD fMRI signal is poorly understood.

We used self organising group level ICA (sogICA) to cluster independent components that were repeatedly present in datasets from multiple runs, thus focusing on ICA findings that could be potentially generalised. To

help with the interpretation of these clusters of independent components we analysed whether the physiological and anaesthesia related covariates that we had recorded influenced these clusters significantly.

Several comparisons between the results of sogICA and our GLM results were possible that confirmed the validity of the sogICA approach:

We were able to replicate the location of significant BOLD fMRI responses found in the model driven GLM analysis. We were also able to confirm the sensitivity of these BOLD fMRI responses to the influence of body temperature. Body temperature had been revealed to be the physiological variable with the most significant influence on the BOLD fMRI response in our GLM analysis.

While these results confirmed the reliability of sogICA, results of this analysis were much richer, as we detected multiple signal components other than stimulus driven BOLD fMRI responses:

We detected a consistent signal contribution due to image motion that was likely based on a temperature drift of the hard shim of the MR scanner. This signal contribution was present despite k-space motion correction by the image reconstruction system of the scanner and subsequent sub millimetre motion correction of our analysis software.

We did not detect an influence of the dose of Mivacurium Chloride on any of the investigated independent signal components, possibly indicating that differing doses of this substance are not a major confound in BOLD fMRI experiments under anaesthesia, given the paralysis is maintained.

As in the GLM Analysis we did not detect a *time independent* influence of the inspiratory fraction of oxygen FiO_2 on the stimulus driven BOLD fMRI responses. This finding surprisingly held also for all of the other independent signal components investigated.

We also detected a strong ICA component in secondary somatosensory cortices that was repeatedly present over runs. Strength and repeatability of this component warrant future research, although its interpretation is unclear at present.

In this thesis results on the influence of hyperoxia on the BOLD fMRI response were presented. These effects were strongly time dependent and varied from brain region to brain region. Our findings for the first time provide a temporal profile of these effects. They resolve the issue of conflicting earlier reports on this topic.

Appendix A

Deoxyhemoglobin Dilution Model with Plasma Oxygen

We here derive the changes in the relative BOLD fMRI response amplitude that are expected under hyperoxia because of oxygen transport via the oxygen that is dissolved in the blood plasma. Our derivation closely follows the original derivation of the Deoxyhemoglobin Dilution Model developed by Hoge and colleagues [50] - up to the point where modifications have to be made to incorporate oxygen that is dissolved in the blood plasma. For readability we have replaced (as is often done) rCBF(V) with CBF(V). It should be clear from the context of evaluating BOLD fMRI responses in a relatively small voxel in this appendix that local, or regional, blood flow is meant.

In their derivation of the Deoxyhemoglobin Dilution Model (DDM) [50] Hoge and colleagues describe the additional transversal relaxation rate $R^*_{2|dHb}$ introduced by the presence of deoxyhemoglobin in an imaging voxel by:

$$R^*_{2|dHb} = A \cdot CBV \cdot [dHb]^{\beta}_{venous} \tag{A.1}$$

with A being a sample specific proportionality constant, $[dHb]_{venous}$ the concentration of deoxyhemoglobin in the venous compartment of the voxel and β a constant describing the MR physics of R^*_2 signal dephasing [10]. Differences in $[dHb]_{venous}$ between the resting state (rest) and the activated state (act) after stimulation lead to a difference in $[dHb]_{venous}$ as described by:

$$\Delta R^*_{2|dHb} = A \cdot (CBV_{act} \cdot [dHb]^{\beta}_{venous,act} - CBV_{rest} \cdot [dHb]^{\beta}_{venous,rest}) \tag{A.2}$$

The influence of this difference on the BOLD signal can be written as:

$$\frac{\Delta BOLD}{BOLD} = \exp(-TE \cdot \Delta R^*_{2|dHb}) - 1 \tag{A.3}$$

or else, in linear approximation, as:

$$\begin{aligned}\frac{\Delta BOLD}{BOLD} &\approx -TE \cdot \Delta R^*_{2|dHb} \\ &= TE \cdot A \cdot \quad \ldots \\ &\quad (CBV_{rest} \cdot [dHb]^{\beta}_{venous,rest} - CBV_{act} \cdot [dHb]^{\beta}_{venous,act})\end{aligned} \tag{A.4}$$

Hoge and colleagues in their derivation then use the strict proportionality of deoxyhemoglobin concentration to $CMRO_2$ derived by the conservation of mass principle under normal physiologic conditions:

$$[dHb]^{\beta}_{venous} = \frac{1}{4} \cdot \frac{CMRO_2}{CBF} \tag{A.5}$$

This equation, however, does not hold under hyperoxic conditions that create a non negligible concentration of physically dissolved oxygen in the plasma (further on abbreviated as PDO_2C; about 1.8 vol% at FiO_2 100%, thus providing about 20% of the tissue's oxygen consumption at rest). Due to the fact that physically dissolved oxygen is metabolized first, the above equation A.5 has to be rewritten (again using the conservation of mass principle) as:

$$\begin{aligned} CMRO_2 &= 4 \cdot [dHb]^{\beta}_{venous} \cdot CBF + PDO_2C \cdot CBF \\ &\Leftrightarrow \\ [dHb]^{\beta}_{venous} &= \frac{CMRO_2 - PDO_2C \cdot CBF}{4 \cdot CBF}\end{aligned} \tag{A.6}$$

Hence, the relationship between $[dHb]$ and $CMRO_2$ is changed from a strict proportionality to a linear one. Using equation A.6 and Grubbs law [43] for the passive relationship of CBV and CBF on the venous side:

$$\frac{CBV_{act}}{CBV_{rest}} = \left(\frac{CBF_{act}}{CBF_{rest}}\right)^{\alpha} \tag{A.7}$$

to replace the various $[dHb]$ and $[CBV]$ terms in A.4 yields:

$$\begin{aligned}\frac{\Delta BOLD}{BOLD} = TE \cdot A \cdot CBV_{rest} \cdot \quad &\ldots \\ \left(\frac{CMRO_{2rest} - PDO_2C \cdot CBF_{rest}}{4 \cdot CBF_{rest}}\right)^{\beta} \cdot \quad &\ldots \\ \left(1 - (\frac{CBF_{act}}{CBF_{rest}})^{\alpha} \left(\frac{\frac{CMRO_{2act} - PDO_2C \cdot CBF_{act}}{CBF_{act}}}{\frac{CMRO_{2rest} - PDO_2C \cdot CBF_{rest}}{CBF_{rest}}}\right)^{\beta}\right)\end{aligned} \tag{A.8}$$

If we now compare the fractional BOLD response amplitudes $\Delta BOLD\%$ in the normoxic *(n)* and hyperoxic *(h)* state we obtain:

$$\begin{aligned}\frac{\Delta BOLD\%_h}{\Delta BOLD\%_n} = \frac{\frac{\Delta BOLD_h}{BOLD_h}}{\frac{\Delta BOLD_n}{BOLD_n}} = \dots \\ \frac{CBV_{h,rest}}{CBV_{n,rest}} \cdot \quad \dots \\ \left(\frac{\frac{CMRO_{2h,rest} - PDO_2C \cdot CBF_{h,rest}}{4 \cdot CBF_{h,rest}}}{\frac{CMRO_{2n,rest}}{4 \cdot CBF_{n,rest}}} \right)^{\beta} \cdot \quad \dots \\ \left(\frac{\left(1 - (\frac{CBF_{h,act}}{CBF_{h,rest}})^{\alpha} \left(\frac{\frac{CMRO_{2h,act} - PDO_2C \cdot CBF_{h,act}}{CBF_{h,act}}}{\frac{CMRO_{2h,rest} - PDO_2C \cdot CBF_{h,rest}}{CBF_{h,rest}}} \right)^{\beta} \right)}{\left(1 - (\frac{CBF_{n,act}}{CBF_{n,rest}})^{\alpha} \left(\frac{\frac{CMRO_{2n,act}}{CBF_{n,act}}}{\frac{CMRO_{2n,rest}}{CBF_{n,rest}}} \right)^{\beta} \right)} \right)\end{aligned} \tag{A.9}$$

To simplify this equation we assume equal metabolic rates for the two resting states (hyperoxic *(h)* and normoxic *(n)*) and the two activated states (i.e. we assume unchanged neuronal activity under hyperoxia):

$$\begin{aligned} CMRO_{2h,act} = CMRO_{2n,act} \quad \wedge \quad CMRO_{2h,rest} = CMRO_{2n,rest} \\ \Rightarrow \\ \frac{CMRO_{2h,act}}{CMRO_{2h,rest}} = \frac{CMRO_{2n,act}}{CMRO_{2n,rest}} =: \epsilon \end{aligned} \tag{A.10}$$

with ϵ being defined as the relative increase in $CMRO_2$ upon stimulation. In addition, we use the proportional (multiplicative) model[1] which assumes that changes in blood flow in response to neuronal activation are proportional to the respective resting state CBF for equal changes ϵ in neuronal activation under conditions n and h:

$$\frac{CBF_{n,act}}{CBF_{n,rest}} = \frac{CBF_{h,act}}{CBF_{h,rest}} =: \delta_{CBF} \tag{A.11}$$

Here δ_{CBF} is defined as the factor of increase in CBF that is brought about by sensory stimulation. For the next simplification steps we use Grubbs law

[1] The alternative to the proportional model would be the *additive model* where equal *absolute* increases in neuronal metabolism would elicit equal *absolute* changes in CBF. As we try to estimate the minimally expected effects of hyperoxia we have to choose the more conservative model. It is indeed possible to calculate that the additive model will predict even larger modulations by hyperoxia than the multiplicative model.

(equation A.7) for the ratio of CBV to CBF to eliminate the remaining CBV terms. In addition we rewrite $CMRO_{2act}$ in terms of $CMRO_{2rest}$ by:

$$CMRO_{2act} = CMRO_{2rest} \cdot \epsilon \tag{A.12}$$

and then use the fact that this resting state $CMRO_2$ can be expressed in terms of the oxygen concentration κ (in units of vol% or, equivalently, $\mathrm{ml}(O_2)/dl(blood)$) that is extracted in the normoxic case at normal flow ($CBF_{n,rest}$) and resting conditions:

$$CMRO_{2act} = \kappa \cdot CBF_{n,rest} \tag{A.13}$$

We thus derive after some algebra[2]:

$$\begin{aligned}\frac{\Delta BOLD\%_h}{\Delta BOLD\%_n} = \quad & \cdots \\ & \left(\frac{CBF_{h,rest}}{CBF_{n,rest}}\right)^{\alpha-\beta} \cdot \quad \cdots \\ & \left(\frac{\kappa \cdot CBF_{n,rest} - PDO_2C \cdot CBF_{h,rest}}{\kappa \cdot CBF_{n,rest}}\right)^{\beta} \cdot \quad \cdots \\ & \frac{1 - \left(\frac{CBF_{h,act}}{CBF_{h,rest}}\right)^{\alpha} \cdot \left(\frac{\frac{\epsilon\cdot\kappa\cdot CBF_{n,rest} - PDO_2C\cdot CBF_{h,rest}\cdot\delta_{CBF}}{CBF_{h,rest}\cdot\delta_{CBF}}}{\frac{\kappa\cdot CBF_{n,rest} - PDO_2C\cdot CBF_{h,rest}}{CBF_{h,rest}}}\right)^{\beta}}{1 - \left(\frac{CBF_{n,act}}{CBF_{n,rest}}\right)^{\alpha} \cdot \left(\frac{\frac{\epsilon\cdot\kappa\cdot CBF_{n,rest}}{CBF_{n,rest}\cdot\delta_{CBF}}}{\frac{\kappa\cdot CBF_{n,rest}}{CBF_{n,rest}}}\right)^{\beta}}\end{aligned} \tag{A.14}$$

Last, we introduce the quotient of hyperoxic and normoxic resting state blood flow $QCBF$ defined by:

$$\begin{aligned} QCBF &:= \frac{CBF_{h,rest}}{CBF_{n,rest}} \\ &\Rightarrow \\ CBF_{h,rest} &= QCBF \cdot CBF_{n,rest} \end{aligned} \tag{A.15}$$

[2]Note that we did not make full use of simplifications to allow the reader to better follow the replacements of different terms

Using this definition, we obtain:

$$\begin{aligned}\frac{\Delta BOLD\%_h}{\Delta BOLD\%_n} = \quad & \dots \\ & (QCBF)^{\alpha-\beta} \cdot \quad \dots \\ & \left(\frac{\kappa - PDO_2C \cdot QCBF}{\kappa}\right)^{\beta} \cdot \quad \dots \\ & \frac{1 - \delta_{CBF}^{\alpha-\beta} \cdot \left(\frac{\epsilon\cdot\kappa - PDO_2C\cdot QCBF\cdot\delta_{CBF}}{\kappa - PDO_2C\cdot QCBF}\right)^{\beta}}{1 - \delta_{CBF}^{\alpha-\beta}\cdot\epsilon^{\beta}}\end{aligned} \tag{A.16}$$

Assuming a fixed coupling of flow to metabolism with gain n:

$$\delta_{CBF} - 1 = n \cdot (\epsilon - 1) \tag{A.17}$$

this can be rewritten as:

$$\begin{aligned}\frac{\Delta BOLD\%_h}{\Delta BOLD\%_n} = \quad & \dots \\ & (QCBF)^{\alpha-\beta} \cdot \quad \dots \\ & \left(\frac{\kappa - PDO_2C \cdot QCBF}{\kappa}\right)^{\beta} \cdot \quad \dots \\ & \frac{1 - (n\cdot\epsilon - n + 1)^{\alpha-\beta} \cdot \left(\frac{\epsilon\cdot\kappa - PDO_2C\cdot QCBF\cdot(n\cdot\epsilon - n + 1)}{8\ vol\% - PDO_2C\cdot QCBF}\right)^{\beta}}{1 - (n\cdot\epsilon - n + 1)^{\alpha-\beta}\cdot\epsilon^{\beta}}\end{aligned} \tag{A.18}$$

The first term in equation A.18 describes the increase of $\Delta BOLD\%$ by the reduction of baseline flow, the second term changes due to altered baseline deoxyhemoglobin production. The third term describes the effect that an increased flow in the activated state also results in an increased supply of plasma oxygen (per unit time), proportional to flow increase rather than to the increase in metabolism[3]. Numerator and denominator of the third term only differ in that ϵ^{β} is replaced by:

$$\left(\frac{\epsilon\cdot\kappa - PDO_2C\cdot QCBF\cdot(n\cdot\epsilon - n + 1)}{8\ vol\% - PDO_2C\cdot QCBF}\right)^{\beta} \tag{A.19}$$

Here corrections made via inclusion of PDO_2C in the denominator are outweighed by those in the numerator when n,ϵ > 1.

[3]This is due to the known mismatch between flow increase and metabolic increase, desctribed by the factor n throughout this derivation. Values of n in the literature range from 2 to 6.

Term 1 (>1) of equation A.18 is the only contribution found in the classical DDM (with $PDO_2C = 0$ terms 2 and 3 are equal to 1). The contribution of term 3 (>1, response increase) outweighs that of term 2 (<1, response decrease) such that the modified DDM always predicts a greater response amplitude increase under hyperoxia than the classical DDM. This may at first seem counterintuitive as inclusion of a nonzero PDO_2C leads to a decrease of resting state *dHb* production and, therefore, seemingly raises the baseline at the cost of relative BOLD signal increases. However, under activation conditions a nonzero PDO_2C has the effect of supplying additional oxygen via plasma due to the increased flow, that by a factor (n) of 2 to 5 outperforms increased metabolism. Reduction of $[dHb]$ under activation condition now results from 2 independent mechanisms: dilution by the increased flow and the use of plasma oxygen for a larger fraction of the tissue's increased energy demand. Because the relative increase in flow usually outperforms the increase in metabolism by a factor of 2 or more (for a review see: [109]) the fraction of plasma oxygen in total oxygen consumption is effectively increased in the activated state.

We can now derive numerical predictions using the values given in table A.1. Results of these calculations are found in table 1.6. For an exemplary

Parameter Values for Simulation		
Parameter	Value Range	References
κ	8 vol%	[98]
$QCBF$	0.67; 0.87	[38, 68]
ϵ	1.05...1.50	assumed values, comp. [110]
α	0.38	[43]
β	1.25	[10]
PDO_2C	1.5 vol%	[98]
n	2...6	[51, 40]

Table A.1: *Range of model values used for simulations and related references*

comparison of the classical and the modified DDM we choose $n = 2$ and $\epsilon = 1.2$ and obtain:

$$mDDM: \quad \frac{\Delta BOLD\%_h}{\Delta BOLD\%_n} = 1.45 \tag{A.20}$$

as compared to:

$$DDM: \quad \frac{\Delta BOLD\%_h}{\Delta BOLD\%_n} = 1.13 \tag{A.21}$$

Note, last, that the influence of the paramagnetism of O_2 dissolved in the plasma was omitted to keep our model simple. The magnetic susceptibility χ_{O_2} of pure O_2 at normal conditions (760 mmHg) is 1.4 ppm. Thus, we expect a contribution of roughly 0.8 ppm for the amounts of physically dissolved O_2 in our experiment at FiO_2 of 90%, if we estimate the O_2 concentration from the measured values presented in [98]. In principle signal changes by changed O_2 levels in blood plasma are therefore possible. We ignored this contribution to our model of relative functional signal changes for the following reason: PDO_2C will be very close to values observed at normoxia after a fraction of the capillary transit time. This is due to the fact that less than one third of $CMRO_2$ is supplied by this pathway at FiO_2 of 90% and oxygen from the plasma is metabolized first. Direct effects of χ_{O_2} would be, therefore, expected on the arterial side and would thus be volume rather than flow effects. Total blood volume changes scale with flow changes to a power of approximtaley 0.38 in the steady state [43]. Furthermore, there are only very few references describing functional arterial volume changes (e.g.: [74]) and in addition the arterial partition of blood volume in a grey matter voxel is around 0.25, thus further limiting a potential direct influence of χ_{O_2} driven volume effects. Most importantly though, such effects should also have shown up as an increase of MION fMRI responses.But in fact, we did observe a *decrease* of these responses.

List of Abbreviations and Symbols

α Grubb's exponent for the passive relationship between rCBF and rCBV.

β A constant describing the MR physics of R_2^* signal dephasing.

$\Delta BOLD\%$ Increase in the BOLD fMRI signal relative to the respective baseline.

δ_{CBF} A factor describing the relative increase of (r)CBF in response to visual stimulation.

ϵ A factor describing the relative increase of neuronal metabolism in response to visual stimulation.

κ The concentration of oxygen that - at normal blood flow - is extracted from oxyhemoglobin and converts it to deoxyhemoglobin. κ is specified in units of ml(O_2)/dl(blood).

$[dHb]$ Concentration of deoxygenated Hemoglobin in the blood.

$(r)CBF$ (regional) Cerebral Blood Flow.

$(r)CBF$ (regional) Cerebral Blood Volume.

BOLD Blood Oxygenation Level Dependent (functional magnetic resonance imaging signal). Sequences that are sensitive to T_2^* contrast have an image contrast that depends on the oxygen saturation of venous blood. This in turn is changed by the hemodynamic response to neuronal activation.

$CMRO_2$ Cerebral Metabolic Rate of Oxygen Consumption

dHb deoxygenated Hemoglobin.

fMRI functional Magnetic Resonance Imaging. Magnetic Resonance Imaging of the brain using sequences that are sensitive to physiological phenomena that are correlated to neuronal activity like blood oxygenation and regional cerebral blood flow.

GLM General Linear Model

LGN Lateral Geniculate Nucleus

PDO_2C Concentration of oxygen dissolved in the blood plasma.

*PGE*2 Prostaglandin E2

QCBF ratio of CBF under hyperoxic conditions to CBF at normoxic conditions

$SQTIME - O2 - 90$ The square of the time elapsed since switching to an inspiratory fraction of oxygen of 90%.

TE Echo time of an MRI sequence.

$TIME - O2 - 90$ Time elapsed since switching to an inspiratory fraction of oxygen of 90%.

TR Repetition time of an MRI sequence.

T_2^* Transversal relaxation time of the spin system due to spin–spin interaction and local susceptibilty effects. R_2^* is the inverse of T_2^*.

T_1 Longitudinal relaxation time of spin system.

n This factor describes the proportionality between normalised increases of CBF and $CMRO_2$

Bibliography

[1] Y. Adachi, K. Watanabe, H. Higuchi, T. Satoh, and E. Vizi. Oxygen inhalation enhances striatal dopamine metabolism and monoamineoxidase enzyme inhibition prevents it: a microdialysis study. *European Journal of Pharmacology*, 422(1-3):61–68, June 2001.

[2] Y. Aghakhani, E. Kobayashi, A. Bagshaw, C. Hawco, C. Benar, F. Dubeau, and J. Gotman. Cortical and thalamic fMRI responses in partial epilepsy with focal and bilateral synchronous spikes. *Clin Neurophysiol.*, 117(1):177–191, Jan. 2006.

[3] D. Atochin, I. Demchenko, J. Astern, A. Boso, C. Piantadosi, and P. Huang. Contributions of endothelial and neuronal nitric oxide synthases to cerebrovascular responses to hyperoxia. *J.Cereb.Blood Flow Metab*, 23(10):1219–1226, Oct. 2003.

[4] A. Bartels and S. Zeki. The chronoarchitecture of the cerebral cortex. *Philos Trans R Soc Lond B Biol Sci*, 360(1456):733–750, Apr 2005.

[5] A. J. Bell and T. J. Sejnowski. An information-maximization approach to blind separation and blind deconvolution. *Neural Comput*, 7(6):1129–1159, Nov 1995.

[6] P. Bickford, K. Chadman, B. Williams, B. Shukitt-Hale, D. Holmes, G. Taglialatela, and J. Joseph. Effect of normobaric hyperoxia on two indexes of synaptic function in Fisher 344 rats. *Free Radical Biology and Medicine*, 26(7-8):817–824, Apr. 1999.

[7] C. Bledowski, K. C. Kadosh, M. Wibral, B. Rahm, R. A. Bittner, K. Hoechstetter, M. Scherg, K. Maurer, R. Goebel, and D. E. J. Linden. Mental chronometry of working memory retrieval: a combined functional magnetic resonance imaging and event-related potentials approach. *J Neurosci*, 26(3):821–829, Jan 2006.

[8] C. Bledowski, D. Prvulovic, K. Hoechstetter, M. Scherg, M. Wibral, R. Goebel, and D. E. J. Linden. Localizing P300 generators in visual target and distractor processing: a combined event-related potential and functional magnetic resonance imaging study. *J Neurosci*, 24(42):9353–9360, Oct 2004.

[9] M. Boakye, B. Krauss, S. Huckins, L. Zhang, N. Szeverenyi, and J. Hodge, C.J. Effects of hyperoxia on human sensorimotor cortex activity produced by electrical stimulation of the median nerve: a functional magnetic resonance imaging study. *Neurosci.Lett.*, 321(1-2):5–8, Mar. 2002.

[10] J. Boxerman, L. Hamberg, B. Rosen, and R. Weisskoff. MR contrast due to intravascular magnetic susceptibility perturbations. *Magn Reson.Med.*, 34(4):555–566, Oct. 1995.

[11] G. Boynton, S. Engel, G. Glover, and D. Heeger. Linear systems analysis of functional magnetic resonance imaging in human V1. *J Neurosci.*, 16(13):4207–4221, July 1996.

[12] R. Buxton. Coupling between CBF and CMRO2 during neuronal activty. In M. Tomita, I. Kanno, and E. Hamel, editors, *Brain Activation and CBF Control*, pages 23–32. Elsevier Science: The Netherlands, Jan. 2002.

[13] V. D. Calhoun, T. Adali, V. B. McGinty, J. J. Pekar, T. D. Watson, and G. D. Pearlson. fMRI activation in a visual-perception task: network of areas detected using the general linear model and independent components analysis. *Neuroimage*, 14(5):1080–1088, Nov 2001.

[14] V. D. Calhoun, T. Adali, G. D. Pearlson, and J. J. Pekar. Spatial and temporal independent component analysis of functional mri data containing a pair of task-related waveforms. *Hum Brain Mapp*, 13(1):43–53, May 2001.

[15] V. D. Calhoun, T. Adali, M. C. Stevens, K. A. Kiehl, and J. J. Pekar. Semi-blind ICA of fMRI: A method for utilizing hypothesis-derived time courses in a spatial ICA analysis. *Neuroimage*, 25(2):527–538, Apr 2005.

[16] C. Carvalho, S. G. Paula Pinto, B. Maranhao, and E. Bethlem. Hyperoxia and lung disease. *Curr.Opin.Pulm.Med.*, 4(5):300–304, Sept. 1998.

[17] H. Chen and D. Yao. Discussion on the choice of separated components in fMRI data analysis by spatial independent component analysis. *Magn Reson Imaging*, 22(6):827–833, Jul 2004.

[18] H. Chen, D. Yao, Y. Zhuo, and L. Chen. Analysis of fMRI data by blind separation of data in a tiny spatial domain into independent temporal component. *Brain Topogr*, 15(4):223–232, 2003.

[19] Y. Chino, J. Kaas, I. Smith, E.L., A. Langston, and H. Cheng. Rapid reorganization of cortical maps in adult cats following restricted deafferentation in retina. *Vision Res.*, 32(5):789–796, May 1992.

[20] J. Christiansen, C. Douglas, and J. Haldane. The absorption and dissociation of carbon dioxide by human blood. *J Physiol*, 48:244–271, 1914.

[21] E. Cohen, K. Ugurbil, and S. Kim. Effect of basal conditions on the magnitude and dynamics of the blood oxygenation level-dependent fMRI response. *J.Cereb.Blood Flow Metab*, 22(9):1042–1053, Sept. 2002.

[22] T. Davis, K. Kwong, R. Weisskoff, and B. Rosen. Calibrated functional MRI: mapping the dynamics of oxidative metabolism. *Proc.Natl.Acad.Sci.U.S A*, 95(4):1834–1839, Feb. 1998.

[23] A. Delorme and S. Makeig. EEGLAB: an open source toolbox for analysis of single-trial EEG dynamics including independent component analysis. *J Neurosci Methods*, 134(1):9–21, Mar 2004.

[24] A. Delorme, H. Serby, and S. Makeig. EEGLAB Tutorial. `http://sccn.ucsd.edu/eeglab/maintut/ICAdecomposition.html`, 2007.

[25] I. Demchenko, Y. Luchakov, A. Moskvin, D. Gutsaeva, B. Allen, E. Thalmann, and C. Piantadosi. Cerebral blood flow and brain oxygenation in rats breathing oxygen under pressure. *J Cereb.Blood Flow Metab*, 25(10):1288–1300, Oct. 2005.

[26] I. Demchenko and C. Piantadosi. Nitric oxide amplifies the excitatory to inhibitory neurotransmitter imbalance accelerating oxygen seizures. *Undersea & Hyperbaric Medicine*, 33(3):169–174, May 2006.

[27] A. Devor, I. Ulbert, A. Dunn, S. Narayanan, S. Jones, M. Andermann, D. Boas, and A. Dale. Coupling of the cortical hemodynamic response

to cortical and thalamic neuronal activity. *Proc.Natl.Acad.Sci.U.S A*, 102(10):3822–3827, Mar. 2005.

[28] U. Dirnagl, U. Lindauer, and A. Villringer. Nitric oxide synthase blockade enhances vasomotion in the cerebral microcirculation of anesthetized rats. *Microvasc.Res.*, 45(3):318–323, May 1993.

[29] E. Disbrow, D. Slutsky, T. Roberts, and L. Krubitzer. Functional MRI at 1.5 Tesla: a comparison of the blood oxygenation level-dependent signal and electrophysiology. *Proc.Natl.Acad.Sci.U.S A*, 97(17):9718–9723, Aug. 2000.

[30] R. Douglas, C. Koch, M. Mahowald, K. Martin, and H. Suarez. Recurrent excitation in neocortical circuits. *Science*, 269(5226):981–985, Aug. 1995.

[31] T. Duong, C. Iadecola, and S. Kim. Effect of hyperoxia, hypercapnia, and hypoxia on cerebral interstitial oxygen tension and cerebral blood flow. *Magn Reson.Med.*, 45(1):61–70, Jan. 2001.

[32] T. Q. Duong, S.-C. Ngan, K. Ugurbil, and S.-G. Kim. Functional magnetic resonance imaging of the retina. *Invest Ophthalmol Vis Sci*, 43(4):1176–1181, Apr 2002.

[33] J. H. Duyn, C. T. Moonen, G. H. van Yperen, R. W. de Boer, and P. R. Luyten. Inflow versus deoxyhemoglobin effects in BOLD functional MRI using gradient echoes at 1.5 T. *NMR Biomed*, 7(1-2):83–88, Mar 1994.

[34] F. Esposito, E. Formisano, E. Seifritz, R. Goebel, R. Morrone, G. Tedeschi, and F. D. Salle. Spatial independent component analysis of functional MRI time-series: to what extent do results depend on the algorithm used? *Hum Brain Mapp*, 16(3):146–157, Jul 2002.

[35] F. Esposito, T. Scarabino, A. Hyvarinen, J. Himberg, E. Formisano, S. Comani, G. Tedeschi, R. Goebel, E. Seifritz, and F. D. Salle. Independent component analysis of fMRI group studies by self-organizing clustering. *Neuroimage*, 25(1):193–205, Mar 2005.

[36] F. Esposito, E. Seifritz, E. Formisano, R. Morrone, T. Scarabino, G. Tedeschi, S. Cirillo, R. Goebel, and F. D. Salle. Real-time independent component analysis of fMRI time-series. *Neuroimage*, 20(4):2209–2224, Dec 2003.

[37] U. Eysel, F. Gonzalez-Aguilar, and U. Mayer. Late spreading of excitation in the lateral geniculate nucleus following visual deafferentation is independent of the size of retinal lesions. *Brain Res.*, 204(1):189–193, Jan. 1981.

[38] T. Floyd, J. Clark, R. Gelfand, J. Detre, S. Ratcliffe, D. Guvakov, C. Lambertsen, and R. Eckenhoff. Independent cerebral vasoconstrictive effects of hyperoxia and accompanying arterial hypocapnia at 1 ATA. *J.Appl.Physiol*, 95(6):2453–2461, Dec. 2003.

[39] E. Formisano, F. Esposito, F. Di Salle, and R. Goebel. Cortex-based independent component analysis of fMRI time series. *Magn Reson.Imaging*, 22(10):1493–1504, Dec. 2004.

[40] P. Fox and M. Raichle. Focal physiological uncoupling of cerebral blood flow and oxidative metabolism during somatosensory stimulation in human subjects. *Proc.Natl.Acad.Sci.U.S A*, 83(4):1140–1144, Feb. 1986.

[41] C. R. Genovese, N. A. Lazar, and T. Nichols. Thresholding of statistical maps in functional neuroimaging using the false discovery rate. *Neuroimage*, 15(4):870–878, Apr 2002.

[42] G. Govindaiah and C. Cox. Depression of retinogeniculate synaptic transmission by presynaptic D-2-like dopamine receptors in rat lateral geniculate nucleus. *European Journal of Neuroscience*, 23(2):423–434, Jan. 2006.

[43] J. Grubb, R.L., M. Raichle, J. Eichling, and M. Ter Pogossian. The effects of changes in PaCO2 on cerebral blood volume, blood flow, and vascular mean transit time. *Stroke*, 5(5):630–639, Sept. 1974.

[44] B. Gutsche and C. Stephen. Responses of dogs to hyperoxic-, pentylenetetrazol-, and electroshock-induced convulsions. *J Appl.Physiol*, 22(2):321–326, Feb. 1967.

[45] N. Harrison and W. Sear. Intravenous Anaesthetics - Barbiturates, Etomidate, Propofol, Ketamine, and Steroids. In A. Evers and M. Maze, editors, *Anesthetic Pharmacology: Physiologic Principles and Clinical Practice*, number 24, pages 395–416. Churchill Livingston, Philadelphia, Pa., Dec. 2003.

[46] K. Hendrich, P. Kochanek, J. Melick, J. Schiding, K. Statler, D. Williams, D. Marion, and C. Ho. Cerebral perfusion during anesthesia with Fentanyl, Isoflurane, or Pentobarbital in normal rats studied by arterial spin-labeled MRI. *Magn Reson.Med.*, 46(1):202–206, July 2001.

[47] H. Hentschke, C. Schwarz, and B. Antkowiak. Neocortex is the major target of sedative concentrations of volatile anaesthetics: strong depression of firing rates and increase of GABA A receptor-mediated inhibition. *Eur.J Neurosci.*, 21(1):93–102, Jan. 2005.

[48] J. Hérault and B. Ans. [neuronal network with modifiable synapses: decoding of composite sensory messages under unsupervised and permanent learning]. *C R Acad Sci III*, 299(13):525–528, 1984.

[49] J. Himberg, A. Hyvrinen, and F. Esposito. Validating the independent components of neuroimaging time series via clustering and visualization. *Neuroimage*, 22(3):1214–1222, Jul 2004.

[50] R. Hoge, J. Atkinson, B. Gill, G. Crelier, S. Marrett, and G. Pike. Investigation of BOLD signal dependence on cerebral blood flow and oxygen consumption: the deoxyhemoglobin dilution model. *Magn Reson.Med.*, 42(5):849–863, Nov. 1999.

[51] R. Hoge, J. Atkinson, B. Gill, G. Crelier, S. Marrett, and G. Pike. Linear coupling between cerebral blood flow and oxygen consumption in activated human cortex. *Proc.Natl.Acad.Sci.U.S A*, 96(16):9403–9408, Aug. 1999.

[52] Y. Huang, S. Caminiti, T. Fawcett, R. Moon, P. Fracica, F. Miller, S. Young, and C. Piantadosi. Natural surfactant and hyperoxic lung injury in primates. I. Physiology and biochemistry. *J Appl.Physiol*, 76(3):991–1001, Mar. 1994.

[53] A. Hyvärinen. Fast ICA for noisy data using Gaussian moments. In *Circuits and Systems, 1999. ISCAS '99. Proceedings of the 1999 IEEE International Symposium on*, volume 5, pages 57–61vol.5, 30 May-2 June 1999.

[54] A. Hyvärinen, J. Karhunen, and E. Oja. *Independent Component Analysis*, chapter 8, pages 165–202. John Wiley & Sons, Inc., 2001.

[55] A. Hyvärinen, J. Karhunen, and E. Oja. *Independent Component Analysis*, chapter 10, pages 221–227. John Wiley & Sons, Inc., 2001.

[56] A. Hyvärinen, J. Karhunen, and E. Oja. *Independent Component Analysis*, chapter 9, pages 165–202. John Wiley & Sons, Inc., 2001.

[57] A. Hyvärinen, J. Karhunen, and E. Oja. *Independent Component Analysis*, chapter 7, pages 147–164. John Wiley & Sons, Inc., 2001.

[58] A. Hyvärinen, J. Karhunen, and E. Oja. *Independent Component Analysis*. John Wiley & Sons Inc., 2001.

[59] A. Hyvärinen and E. Oja. Independent component analysis: algorithms and applications. *Neural Netw*, 13(4-5):411–430, 2000.

[60] C. Iadecola. Neurovascular regulation in the normal brain and in Alzheimer's disease. *Nat.Rev.Neurosci.*, 5(5):347–360, May 2004.

[61] F. Jensen. Red blood cell pH, the Bohr effect, and other oxygenation-linked phenomena in blood O2 and CO2 transport. *Acta Physiol Scand.*, 182(3):215–227, Nov. 2004.

[62] P. Jezzard and A. W. Song. Technical foundations and pitfalls of clinical fMRI. *Neuroimage*, 4(3 Pt 3):S63–S75, Dec 1996.

[63] T. P. Jung, S. Makeig, M. Westerfield, J. Townsend, E. Courchesne, and T. J. Sejnowski. Analysis and visualization of single-trial event-related potentials. *Hum Brain Mapp*, 14(3):166–185, Nov 2001.

[64] C. Jutten and A. Taleb. Source separation: from dusk till dawn. In *Proc. 2nd Int. Workshop on Independent Component Analysis and Blind Source Separation ICA2000*.

[65] R. Kalisch, G. Elbel, C. Gossl, M. Czisch, and D. Auer. Blood pressure changes induced by arterial blood withdrawal influence BOLD signal in anesthesized rats at 7 Tesla: implications for pharmacologic MRI. *Neuroimage*, 14(4):891–898, Oct. 2001.

[66] K. Kashikura, J. Kershaw, A. Kashikura, T. Matsuura, and I. Kanno. Hyperoxia-enhanced activation-induced hemodynamic response in human VI: an fMRI study. *Neuroreport*, 11(5):903–906, Apr. 2000.

[67] K. Kashikura, J. Kershaw, A. Kashikura, X. Zhang, T. Matsuura, and I. Kanno. Hyperoxia modified activation-induced blood oxygenation level-dependent response of human visual cortex (V1): an event-related functional magnetic resonance imaging study. *Neuroscience Letters*, 299(1-2):53–56, Feb. 2001.

[68] S. Kety and C. Schmidt. The effects of altered arterial tensions of carbon dioxide and oxygen on cerebral blood flow and oxygen consumption of normal young men. *J Clin Invest.*, 27:487–492, 1948.

[69] D. Kim, T. Duong, and S. Kim. High-resolution mapping of iso-orientation columns by fMRI. *Nat.Neurosci.*, 3(2):164–169, Feb. 2000.

[70] V. Kiviniemi, J.-H. Kantola, J. Jauhiainen, and O. Tervonen. Comparison of methods for detecting nondeterministic BOLD fluctuation in fMRI. *Magn Reson Imaging*, 22(2):197–203, Feb 2004.

[71] C. Kolbitsch, I. Lorenz, C. Hormann, C. Kremser, M. Schocke, S. Felber, P. Moser, M. Hinteregger, K. Pfeiffer, and A. Benzer. Sevoflurane and nitrous oxide increase regional cerebral blood flow (rCBF) and regional cerebral blood volume (rCBV) in a drug-specific manner in human volunteers. *Magn Reson.Imaging*, 19(10):1253–1260, Dec. 2001.

[72] L. Krubitzer, J. Clarey, R. Tweedale, G. Elston, and M. Calford. A redefinition of somatosensory areas in the lateral sulcus of macaque monkeys. *J Neurosci*, 15(5 Pt 2):3821–3839, May 1995.

[73] N. Lange. Statistical procedures for functional MRI. In C. Moonen and P. Bandettini, editors, *Functional MRI*, Medical Radiology. Springer, 2000.

[74] S. Lee, T. Duong, G. Yang, C. Iadecola, and S. Kim. Relative changes of cerebral arterial and venous blood volumes during increased cerebral blood flow: Implications for BOLD fMRI. *Magnetic Resonance in Medicine*, 45(5):791–800, May 2001.

[75] F. Leite, D. Tsao, W. Vanduffel, D. Fize, Y. Sasaki, L. Wald, A. Dale, K. Kwong, G. Orban, B. Rosen, R. Tootell, and J. Mandeville. Repeated fMRI using iron oxide contrast agent in awake, behaving macaques at 3 Tesla. *Neuroimage.*, 16(2):283–294, June 2002.

[76] U. Lindauer, J. Gethmann, M. Kuhl, M. Kohl-Bareis, and U. Dirnagl. Neuronal activity-induced changes of local cerebral microvascular blood oxygenation in the rat: effect of systemic hyperoxia or hypoxia. *Brain Res.*, 975(1-2):135–140, June 2003.

[77] N. Logothetis, H. Guggenberger, S. Peled, and J. Pauls. Functional imaging of the monkey brain. *Nat.Neurosci.*, 2(6):555–562, June 1999.

[78] N. Logothetis, J. Pauls, M. Augath, T. Trinath, and A. Oeltermann. Neurophysiological investigation of the basis of the fMRI signal. *Nature*, 412(6843):150–157, July 2001.

[79] R. F. Martin and D. M. Bowden. A stereotaxic template atlas of the macaque brain for digital imaging and quantitative neuroanatomy. *Neuroimage*, 4(2):119–150, Oct 1996.

[80] T. Matsuura, K. Kashikura, and I. Kanno. Hemodynamics of local cerebral blood flow induced by somatosensory stimulation under normoxia and hyperoxia in rats. *Comp Biochem.Physiol A Mol.Integr.Physiol*, 129(2-3):363–372, June 2001.

[81] B. Matta, K. Heath, K. Tipping, and A. Summors. Direct cerebral vasodilatory effects of sevoflurane and isoflurane. *Anesthesiology*, 91(3):677–680, Sept. 1999.

[82] A. Mcewan, C. Smith, O. Dyar, D. Goodman, L. Smith, and P. Glass. Isoflurane minimum alveolar concentration reduction by fentanyl. *Anesthesiology*, 78(5):864–869, May 1993.

[83] M. McKeown, T. Jung, S. Makeig, G. Brown, S. Kindermann, T. Lee, and T. Sejnowski. Spatially independent activity patterns in functional MRI data during the stroop color-naming task. *Proc.Natl.Acad.Sci.U.S A*, 95(3):803–810, Feb. 1998.

[84] M. McKeown, S. Makeig, G. Brown, T. Jung, S. Kindermann, A. Bell, and T. Sejnowski. Analysis of fMRI data by blind separation into independent spatial components. *Hum.Brain Mapp.*, 6(3):160–188, 1998.

[85] M. J. McKeown, T. P. Jung, S. Makeig, G. Brown, S. S. Kindermann, T. W. Lee, and T. J. Sejnowski. Spatially independent activity patterns in functional MRI data during the stroop color-naming task. *Proc Natl Acad Sci U S A*, 95(3):803–810, Feb 1998.

[86] M. J. McKeown, S. Makeig, G. G. Brown, T. P. Jung, S. S. Kindermann, A. J. Bell, and T. J. Sejnowski. Analysis of fMRI data by blind separation into independent spatial components. *Hum Brain Mapp*, 6(3):160–188, 1998.

[87] M. J. McKeown, V. Varadarajan, S. Huettel, and G. McCarthy. Deterministic and stochastic features of fMRI data: implications for analy-

sis of event-related experiments. *J Neurosci Methods*, 118(2):103–113, Aug 2002.

[88] T. McMahon, R. Moon, B. Luschinger, M. Carraway, A. Stone, B. Stolp, A. Gow, J. Pawloski, P. Watke, D. Singel, C. Piantadosi, and J. Stamler. Nitric oxide in the human respiratory cycle. *Nat.Med.*, 8(7):711–717, July 2002.

[89] P. Mialon and L. Barthelemy. Effect of hyperbaric oxygen on prostaglandin and thromboxane synthesis in the cortex and the striatum of rat brain. *Mol.Chem.Neuropathol.*, 20(2):181–189, Oct. 1993.

[90] C. H. Moritz, J. D. Carew, A. B. McMillan, and M. E. Meyerand. Independent component analysis applied to self-paced functional MR imaging paradigms. *Neuroimage*, 25(1):181–192, Mar 2005.

[91] C. H. Moritz, V. M. Haughton, D. Cordes, M. Quigley, and M. E. Meyerand. Whole-brain functional MR imaging activation from a finger-tapping task examined with independent component analysis. *AJNR Am J Neuroradiol*, 21(9):1629–1635, Oct 2000.

[92] C. H. Moritz, B. P. Rogers, and M. E. Meyerand. Power spectrum ranked independent component analysis of a periodic fMRI complex motor paradigm. *Hum Brain Mapp*, 18(2):111–122, Feb 2003.

[93] L. Muckli, A. Kohler, M. Wibral, and W. Singer. Brain activity along the apparent motion path-recurrent feedback of area hMT/V5 to V1? *Perception*, 33:22–22, 2004.

[94] J. Niessing, B. Ebisch, K. Schmidt, M. Niessing, W. Singer, and R. Galuske. Hemodynamic signals correlate tightly with synchronized gamma oscillations. *Science*, 309(5736):948–951, Aug. 2005.

[95] S. Ogawa, T. Lee, A. Kay, and D. Tank. Brain magnetic resonance imaging with contrast dependent on blood oxygenation. *Proc.Natl.Acad.Sci.U.S A*, 87(24):9868–9872, Dec. 1990.

[96] T. Omae, S. Ibayashi, K. Kusuda, H. Nakamura, H. Yagi, and M. Fujishima. Effects of high atmospheric pressure and oxygen on middle cerebral blood flow velocity in humans measured by transcranial doppler. *Stroke*, 29(1):94–97, Jan. 1998.

[97] H. Pape and R. Mager. Nitric oxide controls oscillatory activity in thalamocortical neurons. *Neuron*, 9(3):441–448, Sept. 1992.

[98] C. Piantadosi. Physiology of hyperbaric hyperoxia. *Respir.Care Clin.N.Am.*, 5(1):7–19, Mar. 1999.

[99] T. Sato, Y. Takeda, S. Hagioka, S. Zhang, and M. Hirakawa. Changes in nitric oxide production and cerebral blood flow before development of hyperbaric oxygen-induced seizures in rats. *Brain Res.*, 918(1-2):131–140, Nov. 2001.

[100] T. Schicke, L. Muckli, A. L. Beer, M. Wibral, W. Singer, R. Goebel, F. Rsler, and B. Rder. Tight covariation of BOLD signal changes and slow ERPs in the parietal cortex in a parametric spatial imagery task with haptic acquisition. *Eur J Neurosci*, 23(7):1910–1918, Apr 2006.

[101] E. Schneider and K. Brune. Opioid activity and distribution of fentanyl metabolites. *Naunyn Schmiedebergs Arch Pharmacol*, 334(3):267–274, Nov 1986.

[102] K. Sicard and T. Duong. Effects of hypoxia, hyperoxia, and hypercapnia on baseline and stimulus-evoked BOLD, CBF, and CMRO2 in spontaneously breathing animals. *Neuroimage*, 25(3):850–858, Apr. 2005.

[103] W. Singer, F. Tretter, and M. Cynader. Organization of cat striate cortex: a correlation of receptive-field properties with afferent and efferent connections. *J Neurophysiol.*, 38(5):1080–1098, Sept. 1975.

[104] J. Stamler, L. Jia, J. Eu, T. McMahon, I. Demchenko, J. Bonaventura, K. Gernert, and C. Piantadosi. Blood flow regulation by S-nitrosohemoglobin in the physiological oxygen gradient. *Science*, 276(5321):2034–2037, June 1997.

[105] J. V. Stone, J. Porrill, N. R. Porter, and I. D. Wilkinson. Spatiotemporal independent component analysis of event-related fMRI data using skewed probability density functions. *Neuroimage*, 15(2):407–421, Feb 2002.

[106] C. G. Thomas, R. A. Harshman, and R. S. Menon. Noise reduction in BOLD-based fMRI using component analysis. *Neuroimage*, 17(3):1521–1537, Nov 2002.

[107] R. Tootell, D. Tsao, and W. Vanduffel. Neuroimaging weighs in: humans meet macaques in "primate" visual cortex. *J.Neurosci.*, 23(10):3981–3989, May 2003.

[108] R. B. Tootell, M. S. Silverman, E. Switkes, and R. L. D. Valois. Deoxyglucose analysis of retinotopic organization in primate striate cortex. *Science*, 218(4575):902–904, Nov 1982.

[109] K. Uludag. Basic Principles of Functional MRI. In R. Edelman, J. Hesselink, M. Zlatkin, and J. Crues, editors, *Clinical Magnetic Resonance Imaging*, volume 3rd, pages –. Saunders (W.B.) Co Ltd, Nov. 2005.

[110] K. Uludag, D. Dubowitz, E. Yoder, K. Restom, T. Liu, and R. Buxton. Coupling of cerebral blood flow and oxygen consumption during physiological activation and deactivation measured with fMRI. *Neuroimage*, 23(1):148–155, Sept. 2004.

[111] V. G. van de Ven, E. Formisano, C. H. Rder, D. Prvulovic, R. A. Bittner, M. G. Dietz, D. Hubl, T. Dierks, A. Federspiel, F. Esposito, F. D. Salle, B. Jansma, R. Goebel, and D. E. J. Linden. The spatiotemporal pattern of auditory cortical responses during verbal hallucinations. *Neuroimage*, 27(3):644–655, Sep 2005.

[112] L. Wang, P. Osborne, X. Yu, D. Shangguan, R. Zhao, H. Han, and G. Liu. Hyperoxia caused by microdialysis perfusion decreased striatal monoamines: involvement of oxidative stress. *Neurochemistry International*, 42(6):465–470, May 2003.

[113] W. Wang, X. Ho, Y. Yan, T. Yan, and C. Li. Intrasynaptosomal free calcium and nitric oxide metabolism in central nervous system oxygen toxicity. *Aviation Space and Environmental Medicine*, 69(6):551–555, June 1998.

[114] N. Watson, S. Beards, N. Altaf, A. Kassner, and A. Jackson. The effect of hyperoxia on cerebral blood flow: a study in healthy volunteers using magnetic resonance phase-contrast angiography. *European Journal of Anaesthesiology*, 17(3):152–159, Mar. 2000.

[115] N. Weiskopf, U. Klose, N. Birbaumer, and K. Mathiak. Single-shot compensation of image distortions and BOLD contrast optimization using multi-echo EPI for real-time fMRI. *Neuroimage*, 24(4):1068–1079, Feb. 2005.

[116] N. Weiskopf, K. Mathiak, S. Bock, F. Scharnowski, R. Veit, W. Grodd, R. Goebel, and N. Birbaumer. Principles of a brain-computer interface (BCI) based on real-time functional magnetic resonance imaging (fMRI). *IEEE Trans.Biomed.Eng*, 51(6):966–970, June 2004.

[117] R. Weissleder, P. Reimer, A. Lee, J. Wittenberg, and T. Brady. MR receptor imaging - ultrasmall iron-oxide particles targeted to asialoglycoprotein receptors. *American Journal of Roentgenology*, 155(6):1161–1167, Dec. 1990.

[118] M. Wibral, L. Muckli, K. Melnikovic, B. Scheller, A. Alink, W. Singer, and M. Munk. Time dependent effects of hyperoxia on the BOLD fMRI signal in primate visual cortex. *Neuroimage*, 2007. accepted for publication.

[119] T. Wolf, U. Lindauer, A. Villringer, and U. Dirnagl. Excessive oxygen or glucose supply does not alter the blood flow response to somatosensory stimulation or spreading depression in rats. *Brain Res.*, 761(2):290–299, July 1997.

[120] C. Zechner, G. Hahn, W. Jooss, M. Wibral, B. Bitnar, S. Keller, M. Spiegel, P. Fath, G. Willeke, and E. Bucher. Systematic study towards high efficiency multicrystalline silicon solar cells with mechanical surface texturization. In *Photovoltaic Specialists Conference, 1997., Conference Record of the Twenty-Sixth IEEE*, pages 243–246, 29 Sept.-3 Oct. 1997.

[121] X. Zhao, D. Glahn, L. H. Tan, N. Li, J. Xiong, and J.-H. Gao. Comparison of TCA and ICA techniques in fMRI data processing. *J Magn Reson Imaging*, 19(4):397–402, Apr 2004.

Curriculum Vitae

Michael Wibral

Personal Data

Date of Birth	April 30^{th} 1971
City of Birth	Essen, Germany

Education

2002-2007	PhD. Student, Department of Neurophysiology, Max Planck Instute for Brain Research, Frankfurt, Germany
2003	Certificate in Medical Physics, University of Kaiserslautern, Germany
1998	Diploma in Physics University of Konstanz, Germany
1991-1994	Studies in Physics, University of Cologne, Germany
1990	Abitur, Städtisches Gymnasium Olpe, Germany

Professional Experience

1998-2002	Semiconductor Process Engineer, *sunways* AG, Konstanz, Germany

Alternative National Service

1990-1991	Caritas Sozialstation, Olpe, Germany

Publications

Publications as a first author	[118]
Publications as a co-author	[7, 8, 93, 100, 120]

Teaching

September 2006	Lecture on 'Hyperoxia effects in BOLD fMRI', Laboratoire de neurobiologie et diversité cellulaire, ESPCI - CNRS, Paris, France
August 2006	Course on MEG/EEG Data Analysis at the Summer School on 'Theoretical Neuroscience and Complex Systems', Frankfurt Institute for Advanced Studies (FIAS), Frankfurt, Germany

Erklärung

Hiermit erkläre ich, Michael Wibral, geboren in Essen, die vorgelegte Arbeit zur Erlangung des akademischen Grades *Doctor rerum naturalium* mit dem Titel "The BOLD fMRI Signal under Anaesthesia and Hyperoxia" selbstständig und ausschließlich unter Verwendung der angegebenen Hilfsmittel erstellt zu haben. Ich habe bisher noch keinen Promotionsversuch unternommen.

Darmstadt, den 31. Januar 2007

Michael Wibral

Acknowledgements

I would like to thank Professor Wolf Singer. I hope I have learnt from him what it means to be a scientist. I have appreciated the freedom to follow down unexpected and interesting roads that opened up during my initial projects and finally led to this thesis. I also very much enjoyed the life in his department that always provided a place for philosophical discussions and the broader implications of neuroscience. I hope I have also earned something about writing a scientific publication that serves its purpose - to convey meaning to the reader.

I would like to thank my co-workers in this Project: Matthias Munk, Arjen Alink, Betram Scheller, Katharina Melnikovic and Alina Jurcoane. They have invested a lot of their days and nights in this project. I hope they will benefit from it as much as I did. Matthias, your fascination for neuroscience and your hands on support have kept this project going, this thesis would not be here without your help. Thank you very much as well for providing tasty things for the survival of your co-workers whenever necessary. Katharina has provided help crunching the data of this project with BrainVoyagerQX untiringly. With her questions about anaesthesia she has forced me to have a look behind the scenes more than once. I am also very grateful to her for *writing up all the answers* in her thesis. I hope to have learnt from Lars some smart heuristics that make things simple and that scientific strength is not numbers but original ideas. Arjen has never refused to quickly reprogram some stimulus when it was called for. I think he should be paid a second salary by the guys that made the presentation software. Bertram Scheller and Ulrich Kallenbach have given their vast knowledge on anaesthesia to this project. The idea to reformulate the Deoxyhemoglobin Dilution Model with plasma oxygen dates back to a discussion with Bertram. Alina has spent many hours at the scanner providing near real time data analysis.

Discussions on hemodynamic responses from the cellular level to the living brain with Ralf Galuske have been very instructive and an invaluable

source of inspiration for this thesis. I appreciate the prompt help I received from Boris Ebisch, Will Barnes and Evi Scheibinger whenever it was necessary.

Discussions with Jörg Geiger and Frank Tennigkeit from the Junior Research Group 'Cortical Function and dynamics' have helped me a lot in grasping the cellular action of hyperoxia. The very same is true for Prof. Jean Rossier from the *Laboratoire de neurobiologie et diversité cellulaire* at the ESPCI - CNRS in Paris. I really appreciated the opportunity to present my results to him and his group in Paris and I am grateful for their valuable input.

There is no thorough understanding of BOLD fMRI without discussing with Kâmil Uludağ from the Max Planck Institute for Biological Cybernetics in Tübingen - I am very glad to have had that opportunity.

Ralph Schönmeyer provided his excellent *bv-tools* software package that was invaluable in reconstructing the grey/white matter boundary of the monkey brain used for the 3-D surface reconstructions. He was there for a quick fix when needed and for quickly implementing a new feature when we called for it. Last but not least he provided cookies and tea as my friendly next door office neighbour in the Brain Imaging Center (BIC).

Nikolaus Weiskopf kindly provided the real time fMRI sequence to us. Without it we might have missed out on important effects of some anaesthesia variables.

The monkey fMRI team is indebted to the BIC Core Structure, especially Tim Wallenhorst for handling the numerous details necessary to keep the Brain Imaging Center in Frankfurt running and for his support with the measurements. Steffen Volz helped to implement PASL blood flow measurements in the monkey brain and recompiled to the real time fMRI sequences for us. He also translated my algorithm for spatial normalisation in the monkey into a handy BrainVoyagerQX plugin.

Fabrizio Esposito and Vincent van de Ven have provided support, both, in the form of MATLAB code as well as in explaing the intricacies of ICA in fMRI that made things *a lot* easier.

I always appreciated the lively and enlightening discussions with Georg Turi on Independent Component Analysis. It was a lot of fun working with him. I am also very grateful to him for proof-reading the mathematical parts of chapter 2.

The Functional Imaging Group at the Max Planck Institute for Brain Research has always been a great help in times that were difficult now and then. Without the humour of Marcus Naumer, the creativity of Sarah Weigelt,

Axel Kohler's tutorials in statistics, and Amanda Kaas' voice I do not think I would have made it. You wouldn't believe how important the discussion on 'off topics' from african restaurants to Zidane are to the well being of a scientist. Special Thanks go to Sarah Weigelt for being the manager and trainer of our little soccer team.

Steffi, the presence of your freckles has made my life worth living in the last three years. I am happy we could share books on hallucination and philosophy. Thank you.

I am glad I have the parents I have. Only with time I realised in what a marvellous family I grew up. I would especially like to thank my mother for teaching me how to learn things for myself. I still remember the introduction to qualia my father gave me when I was a little kid. It may have had a causal influence on my turning to neuroscience in the end. My Uncle Dieter Schafranek has shown me that science is fun in the first place.

I would like to thank Annette Wibral for donating her LaTeX book to this project. It has saved me from wasting countless hours. Her example of being persistent has kept me going when things got difficult.

I would like to thank my sister Ute Wibral for providing the elegant cover design to the thesis of her clumsy brother.

Matthias Wibral was so kind as to let his older brother win the race for the first PhD thesis - he even gave moral support.

The time spent with my friend Felix has always helped me to recover from working too much. Although our recreational periods sometimes proved to be a tough contrast to work.

My friend Andre Zimmermann has shown me how far you can get by simply not giving up on something.

I don't know how to thank Alice Fritz for all the little things she has done to keep my and other peoples' spirits up in the last 12 years.

David Linden has always entertained me well, both, as a flatmate and with his helpful instructions on how to catch my flight at Italian airports. He and Christoph Bledowski also deserve many thanks for putting me on the track to a *visible* scientific career. I hope we will keep on working together.

Thank you for the melodious synchrony, Amanda and Martha!

Support from the Bundesministerium für Bildung und Forschung (BMBF; Brain Imaging Center Franfkfurt, DLR 01GO0203), the Deutsche Forschungs-

gemeinschaft (DFG) and the Max Planck Society is gratefully acknowledged.